



UNIVERSITEIT VAN PRETORIA  
UNIVERSITY OF PRETORIA  
YUNIBESITHI YA PRETORIA

**Effect of composition and thermomechanical processing on the  
texture evolution, formability and ridging behavior of type AISI 441  
ferritic stainless steel**

**By**

**Mpho Given Maruma**

Supervised by

**Dr C.W Siyasiya**

**Prof. W.E Stumpf**

Submitted in partial fulfillment of the requirement for the degree

Master of Engineering (Metallurgy)

In the

Department of Materials Science and Metallurgical Engineering

Faculty of Engineering, Built Environment & Information Technology

University of Pretoria

South Africa

August 2013



UNIVERSITEIT VAN PRETORIA  
UNIVERSITY OF PRETORIA  
YUNIBESITHI YA PRETORIA

## Preface

This dissertation is submitted for the degree of Masters degree at the University of Pretoria. The research described herein was conducted under the supervision of Dr C.W Siyasiya and Prof W.E Stumpf in the department of Materials Science and Metallurgical Engineering, University of Pretoria

Except where acknowledgements and references are made to the previous work, this work is to the best of my knowledge original. This dissertation is the results of my own work except where specifically indicated in the text. Neither this nor any substantially similar dissertation has been or is being submitted elsewhere for any other degree, diploma or other qualification.

-----  
Maruma Mpho Given



## Acknowledgements

Firstly I would like to start by thanking the God of Mount Zion, Engenase, Edward and Barnabas Lekganyane for giving me strength, wisdom and spiritual support throughout my school and tertiary life. To you Mmina' Kgomo, Thank you so much, you are my rock, the pillar of my strength.

I would also like to express my sincere thanks to my supervisors, Dr C.W. Siyasiya and Prof W.E Stumpf for their invaluable support, guidance, encouragement and input in this research project. I have benefitted a lot from your experience and insight during this research project.

Special thanks must also go to Mrs Sarah Havenga, Mrs Louise Ackerman and Mrs Elsie Snyman-Ferreira for their help with the administrative work.

I would like to extend my gratitude to the Mrs W. Grote for texture measurement I would like to acknowledge the cooperation, sponsorship, provision of materials and relevant data from Columbus stainless steel and of course financial support from Mintek

My colleagues, Kofi A. Annan, Richard Nkhoma, Mpilo Thethwayo and Lindsay Leach, to these I say thanks for your friendship and words of encouragement.

To my parents, siblings and my fiancé thank you so much for your support

Finally I would like to thank the University of Pretoria, in particular the Materials science and Metallurgical Engineering Department for provision of facilities that made it possible to complete my studies successfully



# **EFFECT OF COMPOSITION AND THERMOMECHANICAL PROCESSING ON THE TEXTURE EVOLUTION, FORMABILITY AND RIDGING BEHAVIOUR OF TYPE AISI 441 FERRITIC STAINLESS STEEL**

**Author: Mpho. G. Maruma**

**Supervisors: Dr Charles W. Siyasiya**

**: Prof Waldo E. Stumpf**

**Department of Materials Science and Metallurgical Engineering**

**University of Pretoria**

**Masters of Engineering (Materials Science and Metallurgical Engineering)**

## **Synopsis**

Global warming and air pollution are the major problems facing the world today. Therefore strict environmental legislation on the emission of harmful gases from motor vehicles has forced the automobile industry to search for alternative materials or new materials for exhaust systems. In order to produce cleaner exhaust gases, the exhaust temperature needs to be increased to approximately 900°C. Therefore, exhaust manifolds are exposed repeatedly to hot gases as they are nearest to the engine requiring good oxidation resistance, thermal fatigue properties, cold workability and weldability. One such material to meet the above characteristics is AISI 441 ferritic stainless steel, a dual stabilised Ti and Nb ferritic stainless steel.

Ti and Nb are added to stainless steel to stabilise C and N due to their high tendency to form carbonitrides (Ti,Nb)(C,N) and laves phase (Fe<sub>2</sub>Nb) and Fe<sub>3</sub>Nb<sub>3</sub>C. With 18% Cr content, this steel has a good corrosion resistance at elevated temperatures. Included in many applications of this steel are those requiring deep drawing and related forming operations. However, the drawability and stretchability of ferritic stainless steels is inferior to that of the more expensive austenitic stainless steels. For instance, Columbus Stainless has experienced ridging/roping problems at times during the manufacturing process of type AISI 441 ferritic stainless steel. It is believed that this problem is related to crystallographic texture of materials which have effect on formability. The R-value in FSS can be improved through optimisation of chemical composition, which includes reducing the carbon content, and



processing conditions such as reducing the slab reheating temperature, increasing annealing temperature and refining the hot band grain size.

Therefore the aim of this research project was firstly to investigate effect of amount of cold reduction and annealing temperature on texture evolution and its influence on formability. The as received 4.5 mm hot band steel was cold rolled by 62, 78 and 82% reductions respectively followed by isothermal annealing of each at 900°C, 950°C and 1025°C for 3 minutes. Orientation distribution function (ODF) through X-ray diffractometer (XRD) measurement was used to characterise the crystallographic texture formed in the steel using PANanalytical X'Pert PRO diffractometer with X'celerator detector and variable divergence. Microstructures were characterised using optical microscopy and scanning electron microscope (SEM). The results show that steels that received 78% cold reduction and annealed at 1025°C recorded the highest  $R_m$ -value and lowest  $\Delta R$ -value which enhances its deep drawing capability. In addition, this steel showed the highest intensity of shifted  $\gamma$ -fibre, notably  $\{554\}\langle 225 \rangle$  and  $\{334\}\langle 483 \rangle$ . It can therefore be concluded that the  $\gamma$ -fibre which favours deep drawing, is optimal after 78% cold reduction and annealing at 1025°C.

The second objective was to investigate the effect of (Nb+Ti) content on the crystallographic texture and the subsequent formability and ridging severity. AISI 441 ferritic stainless steel with different amount of (Nb+Ti) content was used i.e. Steel A (0.26Nb+0.2Ti), Steel B (0.44Nb+0.15Ti) and steel C (0.7Nb+0.32Ti). After a strain of 10%, steels A exhibited the least resistance against surface ridging with average roughness  $R_a$  of 1.5  $\mu\text{m}$  followed by steels B with an average roughness  $R_a$  of 1.1 $\mu\text{m}$ . Steel C showed the highest resistance to ridging with an average roughness  $R_a$  of 0.64  $\mu\text{m}$ . This was attributed to the increase in carbonitrides (NbTi)(C,N) due to increased (Nb+Ti) content which acted as nucleation sites for  $\gamma$ -fibre.

Keywords: formability, XRD, (NbTi)(C,N), texture, cold rolling, annealing, ridging

## Publications and Conference Presentations

1. M.G. Maruma, C.W. Siyasiya, and W.E. Stumpf: Effect of cold reduction and annealing temperature on texture evolution of AISI 441 ferritic stainless – Presented at the Ferrous and Base Metals Development Network Conference, Magaliesburg, South Africa, 15-17 October 2012 – Published conference proceedings: Symposium series S73.
2. M.G. Maruma, C.W. Siyasiya, W.E. Stumpf: Effect of cold reduction and annealing temperature on texture evolution of AISI 441 ferritic stainless steel– Published in the Journal of the South African Institute of Mining and Metallurgy, 2013, Vol. 113, pp.115
3. M.G. Maruma, C.W. Siyasiya, W.E. Stumpf: Effect of titanium and niobium on texture evolution and ridging severity of AISI441 ferritic stainless steel – In preparation.



## TABLE OF CONTENTS

1. CHAPTER 1: INTRODUCTION .....	1
1.1. Problem Statement.....	5
1.2. Objectives .....	5
2. CHAPTER 2: BASIC STAINLESS STEEL METALLURGY .....	6
2.1. Classification of stainless steel.....	6
2.1.1. Austenitic Stainless Steel.....	7
2.1.2. Martensitic stainless steel.....	8
2.1.3. Ferritic stainless steels.....	8
2.2. Characteristics of ferritic stainless steel.....	10
2.2.1. General characteristics of type AISI 441 .....	10
2.3. Embrittlement phenomenon.....	11
2.3.1. The ductile to brittle transition (DBTT).....	11
2.3.2. Intermetallic precipitation .....	11
2.3.3. 475°C Embrittlement.....	12
2.3.4. Sensitisation.....	13
2.4. Ferritic stainless steel in automotive industry .....	13
2.5. Stabilisation .....	15
2.5.1. Stabilisation with only Ti.....	16
2.5.2. Ti and Nb dual stabilisation .....	17
3. CHAPTER 3: PRECIPITATION AND NUCLEATION THEORY .....	18
3.1. Homogeneous nucleation .....	18
3.2. Heterogeneous nucleation .....	19
4. CHAPTER 4: TEXTURE IN FERRITICSTAINLESS STEEL.....	22
4.1. Introduction.....	22
4.2. The nomenclature of rolling textures.....	23
4.3. Graphical representation of texture .....	24
4.3.1. Representation of texture by pole diagrams.....	24



4.3.2. Texture Representation by means of Orientation Distribution Function (ODF)	26
4.3.2.1. Euler angles	27
4.3.2.2. Euler space	29
4.3.2.3. Two dimensional representation of ODF	29
4.3.3. Texture measurement by probability-values (P-values)	30
4.5. Deformation and recrystallisation texture in ferritic steels	35
4.5.1. Deformation texture BCC steels	36
4.5.1.1. Typical deformation texture in ferritic stainless steel	37
4.5.2. Annealing texture	37
4.5.2.1. Interpretation of annealing texture	38
4.6. Effect of texture on roping or ridging in ferritic stainless steel	39
4.7. Effect of texture on drawability of ferritic stainless steel	44
4.7.1. Texture requirement for deep drawing	46
4.8. Effect of alloying elements on texture formation	49
5. CHAPTER 5: EXPERIMENTAL DETAILS	51
5.1. Description of the material	51
5.1.1. Chemical composition	51
5.2. Production of experimental alloys	52
5.3. Microstructural analysis	52
5.3.1. Optical microscopy and Scanning electron microscopy	52
5.3.2. Measurement of grain size	53
5.3.3. Scanning electron microscope	53
5.4. Effect of thermomechanical processing on texture	55
5.4.1. Isothermal annealing of specimens after cold rolling	55
5.5. Texture measurement	55
5.6. Mechanical testing	55
5.6.1. Tensile tests	55
5.6.2. Hardness measurement	58



6. CHAPTER 6: RESULTS .....	59
6.1. Introduction.....	59
6.2. Effect of cold reduction and annealing process on microstructural and texture evolution of AISI 441 steel.....	59
6.2.1. Microstructural analysis of as-received steels.....	59
6.2.2. Identification of carbides .....	70
6.2.3. Effect of thermomechanical processing on evolution of texture .....	74
6.2.3.1. Cold rolling texture.....	74
6.2.3.2. Annealing texture .....	75
6.2.4. Annealing parameter .....	79
6.3. Effect of thermomechanical processing on formability.....	80
6.3.1. Formability parameter.....	81
6.4. Effect of (Nb+Ti) content Ratio on microstructural evolution, mechanical properties and texture evolution in AISI 441 ferritic stainless steel .....	82
6.4.1. Effect of (Nb+Ti) content on microstructural evolution of the hot band ..	82
6.4.2. Effect of (Nb+Ti) content on microstructural evolution of the annealed hot band.....	83
6.4.3. Effect of (Nb+Ti) content on the microstructural evolution after 62% cold working	85
6.4.4. Effect of (Nb+Ti) content on the microstructural evolution after 62% cold working and annealing .....	86
6.4.5. Effect of (Nb+Ti) content on recrystallisation kinetics .....	88
6.4.6. Effect of (Nb+Ti) content on mechanical properties of ferritic stainless steel after annealing at 1025°C for 180 minutes.....	89
6.4.7. Effect of (Nb+Ti) content on texture evolution.....	90
6.4.7.1. Effect of (Nb+Ti) content on hot band texture .....	90
6.4.7.2. Effect of (Nb+Ti) content on annealed hot band texture.....	91
6.4.7.3. Effect of (Nb+Ti) content on cold worked steels .....	92
6.4.7.4. Effect of (Nb+Ti) content on cold worked and annealed steels.....	94



6.5. Effect of (Nb+Ti) content on ridging resistance .....	95
7. CHAPTER 7: DISCUSSION.....	98
7.1. Introduction.....	98
7.2. Effect of cold rolling and annealing process on microstructural and texture evolution in AISI 441 ferritic stainless steel.....	98
7.3. Effect of cold rolling and annealing process on formability of AISI 441 ferritic stainless steel .....	100
7.4. Effect of (Nb+Ti) content on microstructural and texture evolution of AISI 441 ferritic stainless steels .....	102
7.4.1. Effect of (Nb+Ti) content on the hot band and annealed hot band texture 102	
7.4.2. Effect of (Nb+Ti) content on the cold rolled texture.....	103
7.4.3. Effect of (Nb+Ti) content on the recrystallisation texture.....	104
7.5. Effect of (Nb+Ti) content on ridging resistance of AISI 441 ferritic stainless steels	105
8. CHAPTER 8: CONCLUSIONS.....	106
9. CHAPTER 9: RECOMMENDATION.....	107
10. REFERENCES .....	108



## LIST OF FIGURES

Figure 1-1: The chromium and nickel prices in latest years [1].	1
Figure 1-2: Effects of air- ratio on fuel economy, exhaust gas temperature and exhaust gas composition [6].	2
Figure 1-3: Components parts of automobile exhaust system [6].	3
Figure 1-4: Deep drawn cup of type AISI 430 stainless steel showing roping phenomenon [1].	4
Figure 2-1: Effect of alloying elements on the microstructure of stainless steels A) effect of nickel and chromium B) effect of carbon and chromium [21].	7
Figure 2-2: Fe-Cr Equilibrium Phase Diagram [23].	9
Figure 2-3: Shifting of the $(\gamma+\alpha)/\gamma$ boundary line through addition of carbon and nitrogen [19].	9
Figure 2-4: Effect of grain size on DBTT [26].	11
Figure 2-5: Heterogeneous precipitation of sigma phase on grain boundaries [29].	12
Figure 2-6: Effect of Nb and Ti addition to toughness of ferritic stainless steel [26].	16
Figure 3-1: Free energy of formation of a stable nucleus.	19
Figure 3-2: Heterogeneous nucleation of a precipitate on a grain boundary.	20
Figure 3-3: Relative activation energy for nucleation on grain boundaries, grain edges and grain corners to that for homogeneous nucleation as a function of a contact angle $\Theta$ .	21
Figure 4-1: Crystal arrangement. a) shows a randomly textured material and b) strongly textured material corresponding to (111) Pole Figure [40].	22
Figure 4-2: Definition of a (100)[100] texture with respect to the rolling direction.	23
Figure 4-3: Schematic representation of the construction of a pole figure [13].	25
Figure 4-4: Contouring of a 3-D pole density distribution to derive the standard 2-D pole figure presentation [47].	26

Figure 4-5: Pole Figures of  $\{111\}\langle 112 \rangle$  orientation from a cold rolled high strength steel corresponding to a series of Gaussian Distribution with scatter width of  $15^\circ$ , a)  $\{100\}$ , b)  $\{111\}$  Pole Figure [48].....26

Figure 4-6: Orientation of the crystal axis system and the sample axis system, s is the intersection of the planes (RD-TD) [50]. .....28

Figure 4-7: Diagram showing how through the Euler angles in the order 1, 2, 3 [47].28

Figure 4-8: Reduced Euler space with some important fibres and orientations [46]..29

Figure 4-9: Schematical representation of some orientations and texture fibres which are relevant for BCC materials at  $\phi_2 = 45$  [15].....30

Figure 4-10: Schematic of EBSD measurement setup [47] .....32

Figure 4-11: Diffraction in four circle texture goniometer with definition of the instrument angle. a) transmission geometry b) reflection geometry [47] .....34

Figure 4-12: Schematic of texture measurement in Schultz reflection geometry [42].35

Figure 4-13: Ridging under uniaxial tension in the RD at 25% elongation in 17% Cr ferritic stainless steel [64]. .....40

Figure 4-14: Roughness profiles of two differently processed materials to analyse ridging phenomenon. (a) One-step cold rolling (80%). (b) two-step cold rolling 60% then 50% [14].....41

Figure 4-15: Schematic drawing of Chao's model [65]. .....42

Figure 4-16 : Schematic drawing of Takechi et al's model [12].....43

Figure 4-17: Schematic representation of plastic buckling mechanism for roping [67]. (b) Before rolling direction elongation and (a) after rolling direction elongation.44

Figure 4-18: Principles involved in deep drawing of a blank sheet into a cup [55].....45

Figure 4-19: Effect of the amount of cold reduction on the  $R_m$ -value and  $\Delta R$  of 18%Cr-2%Mo ferritic stainless steel [17]. .....47

Figure 4-20: The  $\phi_2 = 45^\circ$  sections (Bunge notation) of the experimental ODFs of plain carbon steel, rolled at different finishing temperatures [43].....48



Figure 4-21: Relationship between the {111} intensity and the average strain ratio  $R_m$ -value [69].....49

Figure 4-22: Effect of Carbon [72] and Nitrogen [73] on the  $R_m$ -value on low carbon steel .....50

Figure 5-1: FEI NOVA NanoSEM 230 FEG used for analysis.....54

Figure 5-2: Instron tensile testing machine used to determine  $R_m$ -values and mechanical properties. ....56

Figure 5-3: Specimen dimension for plastic strain ratio determination. ....56

Figure 5-4: Specimen orientation for determining plastic anisotropy of metal [77]. ...57

Figure 5-5: Schematic diagram of tensile specimen showing how surface roughness was measured.....58

Figure 6-1: Effect of cold working on the microstructure of AISI 441 ferritic stainless steels. a) 62% cold worked b) 78% cold worked c) 82% cold worked ..... 60

Figure 6-2: Optical micrograph of the 78% cold rolled specimen after annealing for 300s at (a) 900°C, (b) 950°C and (c) 1025°C cold rolled steel by water quenching.....61

Figure 6-3: Image quality maps of the 78% cold rolled annealed for 300s at (a) 900°C, (b) 950°C and (c) 1025°C cold rolled steel (d) inverse pole figure ..... 62

Figure 6-4: Optical micrograph of the 82% cold rolled specimen after annealing for 300s at (a) 900°C, (b) 950°C and (c) 1025°C cold rolled steel by water quenching.....63

Figure 6-5: Image quality maps of the 82% cold rolled annealed for 300s at (a) 900°C, (b) 1025°C cold rolled steel and (c) inverse pole Figure .....64

Figure 6-6: Grain boundary character distribution plots of 78% cold rolled steel and annealed at (a) 900°C, (b) 950°C and (c) 1025°C cold rolled steel.....66

Figure 6-7: Grain boundary character distribution plots of 82% cold rolled steel and annealed at (a) 900°C, (b) 1025°C cold rolled steel.....67

Figure 6-8: SEM micrographs after 78% cold rolling and annealing at a) 900°C, b) 950°C and c) 1025°C for 300s .....	68
Figure 6-9: Micrographs for steels cold rolled and all annealed at 1025°C for 180s: (a) 62% industrially produced (b) 78% cold rolled in the lab and (c) 82% cold rolled in the lab .....	70
Figure 6-10: Optical micrograph of as-received hot band after etching with H <sub>2</sub> O, HCl and HNO <sub>3</sub> for 60 seconds.....	70
Figure 6-11: SEM-EDS spectra of the yellow particle observed in Figure 6-8.....	71
Figure 6-12: The isopleth diagram at 17.9%Cr showing the stable equilibrium phases in type 441 stainless steel with a constant amount of alloying elements and 0–0.5 wt.% of carbon [86]......	72
Figure 6-13: a) Scanning electron micrographs of the as-received cold rolled and annealed steel showing precipitation at grain boundaries and inside the matrix, b) and c) are the SEM-EDS spectra of the observed particles.....	73
Figure 6-14: XRD Bunge ODFs $\varphi_2 = 45$ section for steels cold rolled a) 62% as-received, b) and c) cold rolled in the lab for 78% and 82% respectively, and d) $\varphi_2 = 45^\circ$ section showing the position of the main orientations in BCC steels along the RD, ND and TD directions [78]......	74
Figure 6-15: Bunge ODF $\varphi_2 = 45$ section showing the presence of relatively strong $\gamma$ - and weak $\alpha$ -fibres of the as-received cold rolled and annealed steel B.....	76
Figure 6-16: Bunge ODF $\varphi_2 = 45$ section for steels cold rolled 78% and annealed at 900, 950 and 1025°C for 300s. ....	77
Figure 6-17: Bunge ODF $\varphi_2 = 45$ section for steels cold rolled 82% and annealed at 900, 950 and 1025°C for 300s .....	78
Figure 6-18: Effect of annealing temperature on the texture parameter of AISI 441 ferritic stainless steel after 78 and 82% cold reduction.....	79
Figure 6-19: Effect of percentage cold reduction on average strain ratio ( $R_m$ -value) for steels annealed at 1025°C for 300s. ....	81

Figure 6-20: Relationship between  $R_m$ -value and the texture parameter  $\log_{10} \left( \frac{I_{(111)}}{I_{(100)}} \right)$  of AISI 441 ferritic stainless steel after being annealed at 900, 950 and 1025°C for 300s .....82

Figure 6-21: Effect of (Nb+Ti) content on the hot band microstructure of AISI 441 ferritic stainless steels: (a) steel A with 0.26Nb+0.2%Ti (b) steel B with 0.44Nb and 0.15Ti (c) steel C with 0.7%Nb and 0.32% Ti .....83

Figure 6-22: Effect of (Nb+Ti) content on the hot band microstructure of AISI 441 ferritic stainless steels after annealing at 1025°C for 300s: (a) steel A with 0.26Nb+0.2%Ti (b) steel B with 0.44Nb and 0.15Ti (c) steel C with 0.7%Nb and 0.32% Ti .....85

Figure 6-23: Effect of (Nb+Ti) on the microstructure of 62% cold worked AISI 441 ferritic stainless steels. (a) Steel A with 0.26Nb+0.2%Ti (b) steel B with 0.44Nb and 0.15Ti (c) steel C with 0.7%Nb and 0.32% Ti .....86

Figure 6-24 : Effect of (Nb +Ti) content on the Microstructure of 62% cold worked and annealed at 1025°C for 300s. (a) Steel A with 0.26Nb+0.2%Ti (b) steel B with 0.44Nb and 0.15Ti (c) steel C with 0.7%Nb and 0.32%Ti .....87

Figure 6-25: Effect of (Nb+Ti) content on the recrystallisation kinetics of AISI 441 ferritic stainless steel after annealing at 1025°C for different times .....88

Figure 6-26: Effect of (Nb+Ti) on the Texture Evolution of Hot Band (a) steel A with 0.26Nb+0.2%Ti (b) steel B with 0.44Nb and 0.15Ti and (c) steel C with 0.7%Nb and 0.32% Ti .....91

Figure 6-27: Effect of (Nb+Ti) on the texture evolution of hot band after annealing at 1025°C for 300s. (a) 0.44Nb and 0.15Ti (b) 0.7%Nb and 0.32% Ti. ....92

Figure 6-28: the  $\varphi_2 = 45^\circ$  sections of the ODFs measured in the centre of the steel A with 0.26Nb+0.2Ti 62% cold worked sheets .....93

Figure 6-29: the  $\varphi_2 = 45^\circ$  sections of the ODFs measured in the centre of the 0.44Nb+0.15Ti 62% cold worked sheets .....93

Figure 6-30: the  $\varphi_2 = 45^\circ$  sections of the ODFs measured in the centre of the 0.7Nb+0.32Ti 62% cold worked sheets.....94

Figure 6-31: Effect of ( Nb +Ti) content on the cold worked after annealing at 1025 for 300s annealed of AISI 441 ferritic stainless steels. (a) Steel A with 0.26Nb+0.2%Ti (b) steel B with 0.44Nb and 0.15Ti (c) steel C with 0.7%Nb and 0.32% Ti.....95

Figure 6-32: Effect of (Nb+Ti) content on ridging resistance of AISI 441 ferritic stainless steel after annealing at 1025°C for 300s. ....96

Figure 6-33: Effect of (Nb+Ti) content on the ridging resistance of AISI 441 ferritic stainless steel. ....97

Figure 7-1: Effect of annealing time and temperature on texture variation of some important texture components in low carbon steel [107]. .... 100



## LIST OF TABLES

Table 1-1: Chemical composition in wt. % of type AISI 441 ferritic stainless steel .....	3
Table 2-1: Service temperature, steel grade and required properties for exhaust components [6, 31] .....	14
Table 4-1: Summary of important fibres and texture components in BCC steels [46]	24
Table 4-2: Major transformation texture components and their related orientations [68].....	48
Table 5-1: Chemical composition (wt. %) of the industrial steel designated B and experimental alloys A and C.....	51
Table 5-2: Dimensions for the tensile test specimen.....	57
Table 6-1: Effect of thermomechanical processing on formability as measured by the $R_m$ -value and $\Delta R$ .....	80
Table 6-2: Effect of (Nb+Ti) content on mechanical properties of ferritic stainless steel after annealing at 1025°C.....	89



## LIST OF ABBREVIATION

BCC	Body centred cubic
FCC	Face centred cubic
FSS	Ferritic stainless steel
DBTT	Ductile to brittle transition temperature
ODFs	Orientation distribution function
$R_m$ -value	Plastic strain ratio
$\Delta R$	Plastic anisotropy
$M_s$ -temperature	Martensite start temperature
$M_f$ -temperature	Martensite finishes temperature
RD	Rolling direction
TD	Transverse direction
ND	Normal direction
P-value	Probability value
XRD	X-ray diffraction
SEM	Scanning electron microscope
EBSD	Electron backscattered diffraction
SB	Shear band



## LIST OF SYMBOLS

$\theta$  = contact angle

$\gamma$  = austenite

$\alpha$  = ferrite

$\varphi_1, \Phi, \varphi_2$  = Euler angles (Bunge definition).

$\psi, \Theta, \text{ and } \Phi$  = Euler angles (Roe definition)

$\Delta G_E$  = strain energy

$\Delta G_V$  = Gibbs chemical free energy released per unit volume of new phase

$r^*$  = critical radius

$Q$  = activation energy for diffusion

$t$  = time

$r_0$  = initial average particle radius

$N$  = nucleation rate

$N_T$  = number of recrystallisation nuclei with texture

$N_R$  = number of recrystallisation nuclei without texture

$G_T$  = growth rate of nuclei with the texture

$G_R$  = growth rate of nuclei with random texture

$I_{(hkl)}$  = diffraction intensity from a particular family of (hkl) plane

$f(g)$  = orientation density function

$V$  = total volume of the sample

$G$  = interfacial surface energy per unit area associated with the interface of the two phases



UNIVERSITEIT VAN PRETORIA  
UNIVERSITY OF PRETORIA  
YUNIBESITHI YA PRETORIA

**This degree is dedicated**

**to**

**His Grace the Right Reverend Bishop Dr B.E Lekganyane,**  
*“Kgomo a mmaphaka a Bomonare”*

**for**

**His Guidance, Mercy and Everlasting Love**  
*(Psalm 23, 27, 136, 138, 139)*



## 1. CHAPTER 1: INTRODUCTION

Columbus Stainless is South Africa's primary and only producer of stainless steel flat products. An accelerated development of ferritic stainless steels to substitute the conventional austenitic stainless steels has been adopted by the company in the past few years. Examples include the replacement of AISI 304 austenitic stainless steel with AISI 441 ferritic stainless steel in some applications. Firstly, this is due to the volatility of the nickel price (see Figure 1-1) in recent years that resulted in many manufacturers opting to replace the Ni-containing austenitic stainless steels with ferritic steels that contain no nickel.

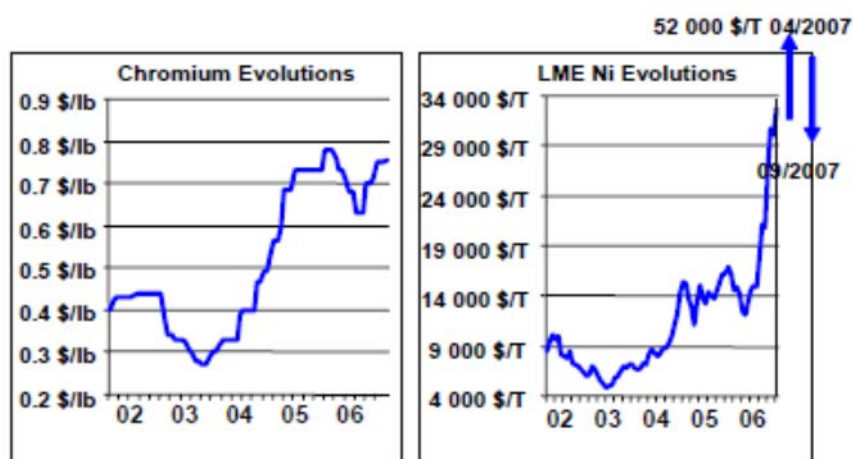


Figure 1-1: The chromium and nickel prices in latest years [1].

Charles et al [1] reported that ferritic stainless steel appears to be the most effective solution to the commercial effects of the high volatility of the nickel price. Their chromium content lies in the range between 17.5-19% that will be specific kind of ferritic stainless steel so be specific with no or little nickel. Therefore, their market share has grown considerably recently and these stainless steels already represent about 30% of the total stainless steel production.

Secondly, global warming and air pollution are amongst the major problems facing the world today. Strict environmental legislation on the emission of harmful gases from motor vehicles has, therefore, forced the automobile industry to search for alternative and cheaper materials for catalytic converters in the exhaust systems. A catalytic converter is an exhaust emission control device which controls toxic substances or chemicals in the exhaust by converting harmful gases into less toxic

substances. Examples include the conversion of carbon monoxide (CO), hydrocarbons ( $C_xH_y$ ) and oxides of nitrogen ( $NO_x$ ) to carbon dioxide ( $CO_2$ ), water ( $H_2O$ ) and nitrogen. Catalytic converters are currently South Africa's biggest automotive components export segment, with a share of 44% of all components exported in 2009 by value [2]. It has been reported by Southern Africa Stainless Steel Development Association (SASSDA) [3] that production of these exhaust components now exceeds 10 million units per year, which means that South Africa now produces about 10% of the world's catalytic converters, representing a R1 billion a year business export. It was further reported that this industry consumes 30% of primary materials supplied into the domestic market by Columbus Stainless. The major market for South African produced catalytic converters is Europe at more than 80% of export volumes [4].

In order to produce cleaner outlet gases, the exhaust temperature needs to be increased to approximately  $900^\circ C$  [5]. As the exhaust temperature is increased, there is an improvement in fuel consumption and a reduction in the emission of carbon monoxide gas as indicated in Figure 1-2. At lower temperatures than the above  $900^\circ C$ , the purification reactions of  $NO_x$ , HC and CO in the exhaust gas are difficult to achieve.

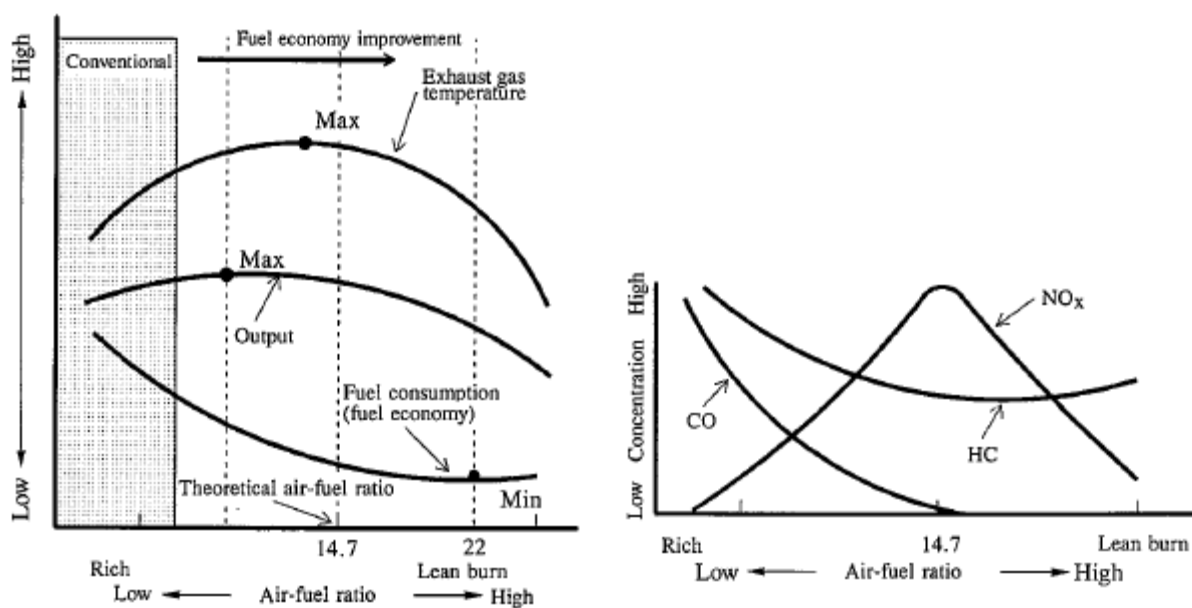


Figure 1-2: Effects of air- ratio on fuel economy, exhaust gas temperature and exhaust gas composition [6]

Exhaust manifolds are exposed repeatedly to hot gases as they are nearest to the engine as shown in Figure 1-3, with the catalytic converter relatively close by. Therefore excellent oxidation resistance, thermal fatigue properties, good workability and weldability and low thermal capacity to enhance the catalytic functions of the converter are necessary

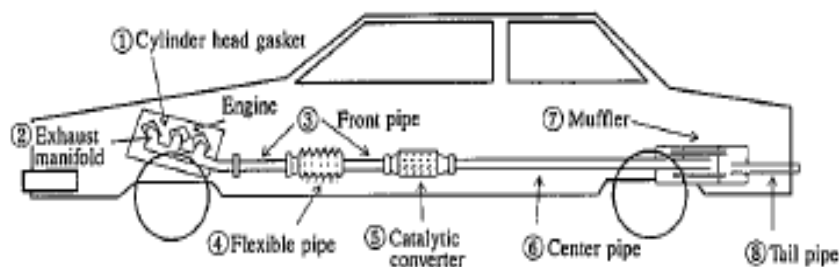


Figure 1-3: Components parts of automobile exhaust system [6]

High exhaust gas temperatures can be maintained by reducing the thickness of the exhaust manifold materials as this will decrease the thermal capacity [7]. This reduction in thickness will contribute significantly to the overall total weight reduction of the vehicles. It has been reported by Hiramatsu [8] that to reduce the weight of an exhaust manifold, heat resistant materials are required and application of the ferritic stainless steels as a substitution for cast iron is increasing.

One such material to meet the above characteristics is AISI 441 ferritic stainless steel with a chemical composition as shown in Table 1-1. AISI 441 is a Nb-Ti dual stabilised ferritic stainless steel which presents good oxidation and oxidation resistance at high temperature and has a low thermal expansion coefficient.

Table 1-1: Chemical composition in wt. % of type AISI 441 ferritic stainless steel

	%C	%Mn	%Si	%Cr	%N	Ni	%S	%P	%Nb	%Ti	Remarks
Min				17.5					0.39	0.1	Nb $\geq$ 0.3+(3×C)
Max	0.03	1.00	1.00	18.5	0.045	0.5	0.015	0.04	1.00	0.6	

This steel, with approximately 18 wt.% Cr, has a good corrosion resistance at elevated temperatures. Ti and Nb are added to this stainless steel to stabilise C and N due to their high tendency to form carbonitrides such as Ti(C,N) and, Nb(C,N). It has been reported by Fujuta et al [5, 9] that fine precipitates formed during deformation also improves their high temperature strength. These precipitates lower the interstitial carbon and nitrogen content in the matrix and as a result this leads to fully ferritic microstructures at all temperature ranges. Furthermore, it is important to note that Ti and Nb carbides and nitrides are more stable than chromium carbides and therefore their formation inhibits the formation of chromium carbides at grain boundaries, hence this prevents sensitization by preventing the intergranular corrosion along such boundaries. Included in their many applications are those requiring deep drawing and related forming operations. Other applications where AISI 441 ferritic stainless steel can be used include heat exchanger tubes, sinks and welded parts of washing machines [1].

However, the formability of ferritic stainless steels is inferior to that of austenitic stainless steels as the former suffers from undesirable surface defects known as ridging or roping as depicted in Figure 1-4.

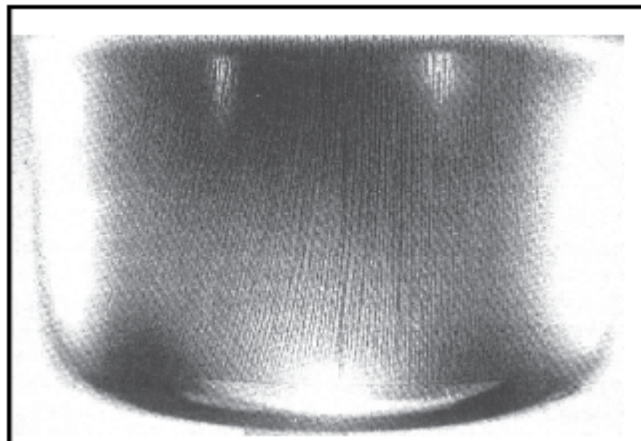


Figure 1-4: Deep drawn cup of type AISI 430 stainless steel showing roping phenomenon [1]

Therefore, considerable research has been carried out to understand the causes of ridging and improving the drawability of ferritic stainless steel [10-12]. It has been shown that the formability of ferritic stainless steel can be improved by increasing the plastic strain ratio (R-value) which is related to the {111} recrystallisation texture [13-16]. The R-value in ferritic stainless steel can be improved through optimisation of

the chemical composition and the processing conditions such as decreasing the carbon content, reducing the slab reheating temperature, increasing annealing temperature or refining the hot band grain size.

Nb and Ti additions to ferritic stainless steel promote the development of a {111} type texture through stabilisation of C and N in solid solution and thus they increase the R-value. Ti stabilised 18% Cr – 2%Mo ferritic stainless steel shows excellent formability because of a high capacity for deep drawing as measured by its plastic strain ratio and a low planar anisotropy [17].

### **1.1. Problem Statement**

The ferritic steel type AISI 441 is a fairly new developed product and it is increasingly being used to replace some of the austenitic stainless steel types. Included in their many applications are those requiring deep drawing and related forming operations. Ridging/roping problems are experienced at times by most manufacturers of this steel and it is believed that this problem is related to the crystallographic texture which can be optimised by optimising the steel's composition and its thermomechanical production process. Research has, for instance, shown that the desired crystallographic texture can be enhanced by the addition of Ti and Nb to this steel [18].

### **1.2. Objectives**

The aim of this study was to investigate the effect of the (Ti+Nb) content, the annealing temperature and cold reduction on the crystallographic texture of the AISI 441 stainless steel and its influence on the formability and ridging of this steel.

The expected outcomes of this research project were as follows:

- I. Establish the effects of cold rolling and annealing practices in order to optimise the annealing texture.
- II. Optimisation of the (Ti+Nb) content for maximum drawability and minimum ridging;

## 2. CHAPTER 2: BASIC STAINLESS STEEL METALLURGY

### 2.1. Classification of stainless steel

Stainless steels are iron based alloys containing appreciable amounts of chromium. These alloys are mainly used as engineering materials for their excellent corrosion resistance in many environments. Stainless steels contain at least 10.5% chromium and preferably more than 13% of Cr to be stainless and have adequate atmospheric corrosion resistance [19]. Chromium is noted for the formation of a very stable, thin, hydrated surface oxide film (essentially  $\text{Cr}_2\text{O}_3$ ) in oxidising environments when alloyed with chromium. This oxide film protects the underlying iron-chromium alloy from corrosion by forming a diffusion barrier between the corrosive environments and underlying metal.

In addition to chromium, stainless steel may also have a number of alloying elements such as molybdenum, aluminium, Ti and Nb. These are ferrite formers and they increase the extent of the ferrite phase field in stainless steels. Molybdenum also has a beneficial effect on the corrosion resistance of stainless steel alloys as it improves pitting and crevice corrosion attack. Aluminium improves high temperature oxidation and carburisation resistance. Ti and Nb forms stable carbides to resist sensitization and improve high temperature properties [9]. Other elements such as a nickel, nitrogen and carbon stabilise the austenite at the expense of ferrite and martensite i.e. they suppress the  $M_s$ -temperature as shown in Figure 2-1

Carbon and nitrogen also increase the strength of stainless steels with carbon primarily at elevated temperature and nitrogen at cryogenic temperature. At the same time carbon also decreases the corrosion resistance of stainless steel and, therefore, there must be a balance between the two. Nitrogen provides attractive properties such as good fracture strength and also improves the corrosion resistance particularly the resistance to pitting corrosion [20].



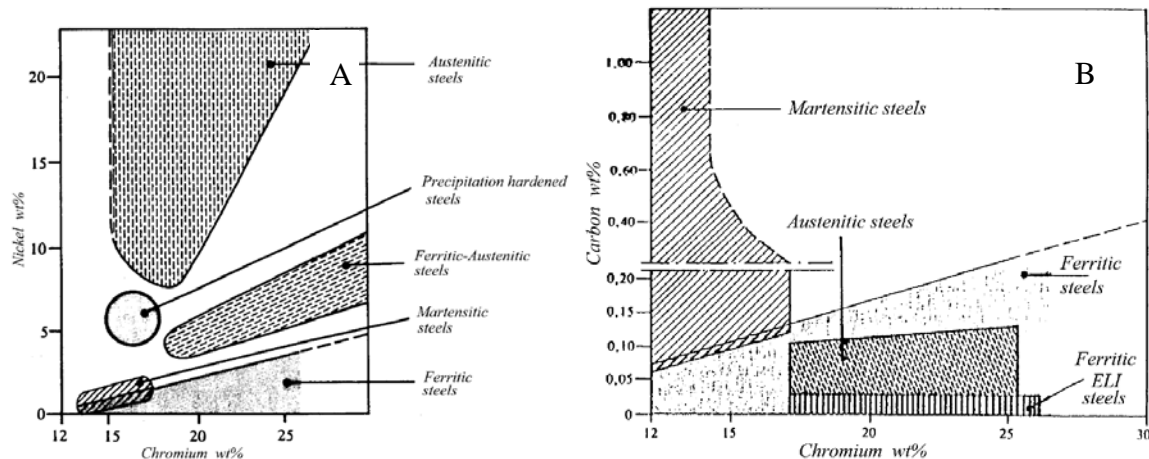


Figure 2-1: Effect of alloying elements on the microstructure of stainless steels A) effect of nickel and chromium B) effect of carbon and chromium [21]

It should be noted from Figure 2-1 that carbon is a very strong austenite former and Cr is a strong ferrite former. If the carbon content of a stainless steel is very low, slightly more Ni may have to be added to compensate for the loss of the austenite forming properties of the carbon.

Stainless steel can be classified into three classes according to chemical compositions and structure; austenitic stainless steel (face centered cubic, FCC), ferritic stainless steel (body centered cubic, BCC) and martensitic stainless steel (body centered tetragonal, BCT). Stainless steels containing both austenite and ferrite usually in equal amounts are known as duplex stainless steel.

### 2.1.1. Austenitic Stainless Steel

Austenitic stainless steels are generally defined as the iron based alloys with at least 10.5 to 12% chromium and carbon content normally below about 0.15%. With increasing demand on corrosion resistance, the chromium content must be increased to levels above 16%. Like Ferritic stainless steels, they are classified as austenitic due to their room temperature microstructure remaining mostly austenitic. In stainless steels containing more than 16% Cr, an austenitic microstructure can be obtained by alloying with minimum of 6% nickel [22]. Nickel is a strong austenite former and it extends the austenite phase field. As a result, austenite remains stable at higher chromium levels and down to room temperature.

These alloys are non-magnetic in the annealed conditions and do not harden during heat treatment. Austenitic stainless steels can be hot worked easily and cold worked if proper allowance is made for their high rate of work hardening. Another interesting property is their best high temperature strength and resistance to scaling compared to martensitic and ferritic stainless steels. However, due to high nickel prices, they are being replaced by low cost ferritic stainless steels.

### **2.1.2. Martensitic stainless steel**

Martensitic stainless steels by definition lie within the chromium range of 11.5 to 18%Cr, with the lower limit being governed by corrosion resistance and upper limit by the requirement to convert fully to austenite on heating. A fully martensitic structure can be achieved in a stainless steel provided that:

- i. There is a balance of alloying elements to produce a fully austenitic structure at the solution treatment temperature,
- ii. The  $M_s$ - $M_f$  temperatures are above room temperature [23].

Martensitic stainless steels are air-hardening, magnetic, can be cold-worked and hot worked without difficulty. Martensitic stainless steel with low carbon content can be machined satisfactorily, have good toughness and show good corrosion resistance to weather and some chemicals. They attain their best corrosion resistance in hardened conditions but are not as corrosion resistant as the austenitic or ferritic stainless steels.

### **2.1.3. Ferritic stainless steels**

Ferritic stainless steels are essentially iron-chromium binary alloys containing about 12 to 30 wt.% chromium as the major alloying element and the maximum content of carbon is 0.25 wt.%. They are called ferritic stainless steels because their structure remains mostly ferrite at room temperature. Chromium is a powerful ferrite former as it extends the  $\alpha$ -ferrite phase field and suppresses the region where austenite is stable. Ferritic stainless steels contain more than 12 wt.% Cr containing no interstitial element do not undergo the  $\gamma \rightarrow \alpha$  phase transformation but cool from solidification temperatures as solid solutions of Cr in ferrite, see Figure 2-2 below.



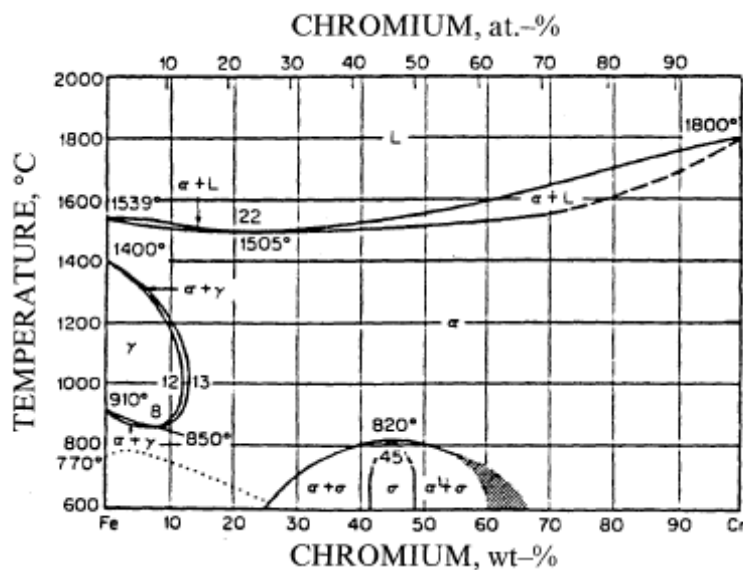


Figure 2-2: Fe-Cr Equilibrium Phase Diagram [23].

It is not only the Cr content that matter in order to obtain fully ferritic microstructure at room temperature; the interstitial elements C and N must be kept at minimum. These interstitials elements enlarge the  $(\gamma + \alpha)$  phase field shifting it to higher chromium levels as depicted in Figure 2-3 below.

These steels are relatively low in cost because they do not contain substantial amounts of nickel and they are resistant to chloride stress corrosion cracking [5]. Therefore, they are preferred to austenitic stainless steel in certain applications. They are magnetic and are typically employed where corrosion resistance is needed and where strength requirements are relatively moderate

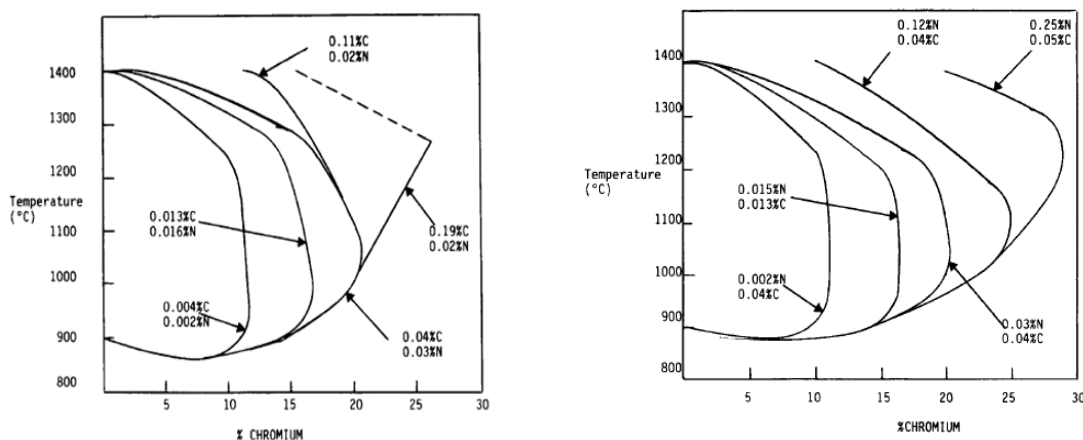


Figure 2-3: Shifting of the  $(\gamma+\alpha)/\gamma$  boundary line through addition of carbon and nitrogen [19].

Ferritic stainless steel cannot be hardened by heat treatment and are only moderately hardenable by cold working. The ferritic structure in these steels introduces a number of metallurgical problems that influence their mechanical properties. Among the metallurgical problems encountered in ferritic stainless steel are poor ductile to brittle transition temperatures, precipitation of intermetallic phases, 475°C embrittlement, low ductility of the welded conditions, sensitization and high temperature embrittlement [24].

## **2.2. Characteristics of ferritic stainless steel**

### **2.2.1. General characteristics of type AISI 441**

AISI 441 alloy is a low carbon and nitrogen ferritic stainless steel containing between 17-18 wt.% Cr. This alloy is dual stabilised with Nb and Ti to enhance its high temperature corrosion and oxidation resistance. AISI 441 remains a single ferritic phase at all temperatures up to its melting point and, therefore, cannot be hardened by heat treatment. In the annealed state, AISI 441 is ductile and can be formed into various shapes. However this steel has limited weldability and should not be used in the as-welded condition for impact loaded structure as this steel undergoes severe grain growth in the heat affected zones (HAZs) during welding [25]. This alloy's enhanced stress corrosion resistance, high temperature oxidation resistance, creep resistance, high thermal conductivity and lower coefficient of thermal expansion makes it suitable for application in the automobile industry, hot water tanks and heat exchangers. However, type AISI 441 stainless steel has some disadvantages compared to austenitic stainless steels of which some are: ridging and roping after drawing, poor toughness in impact loading, an inherent brittleness and poor DBTT, sensitisation and excessive grain growth at elevated temperatures.

## 2.3. Embrittlement phenomenon

### 2.3.1. The ductile to brittle transition (DBTT)

The DBTT of ferritic stainless steels increases with increasing chromium content and grain size, see Figure 2-4. Assuming no grain growth after the recrystallization process, the thinner gauge materials which receive more cold reduction during forming process will have smaller grain sizes and hence the lower DBTT.

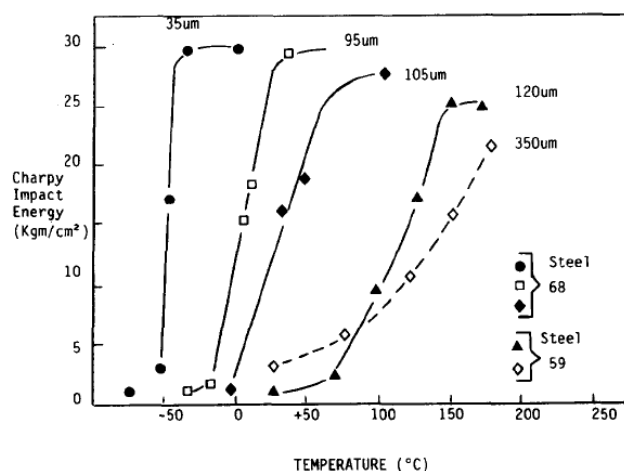


Figure 2-4: Effect of grain size on DBTT [26].

### 2.3.2. Intermetallic precipitation

Precipitation of intermetallic phases is undesirable as they have negative influence on the mechanical properties and corrosion resistance of the alloy. Sigma phase ( $\sigma$ ) is one of the most common intermetallic phases which form in the Fe-Cr systems. It is a hard, brittle, incoherent intermetallic compound of iron and chromium (FeCr) consisting of approximately 45% Cr and 55% Fe. Ferritic stainless steels are susceptible to the formation of sigma phase when they are exposed to temperature range of 700 to 800°C [27]. During tempering/annealing, the sigma phase heterogeneously precipitates first on grain boundary triples points and after site saturation, on grain boundaries as shown in Figure 2-5 below. Its precipitation is accompanied by chromium, nickel and silicon depletion of the matrix adjacent to the sigma grain boundaries. This renders adjacent matrix prone to intergranular corrosion leading to premature failures.

Sigma phase formation is generally slow. On one hand, its precipitation is accelerated significantly by addition of ferrite stabilizing elements such as chromium, molybdenum, silicon, Ti, vanadium and tantalum and on the other hand it is retarded by the addition of nickel, cobalt, aluminium, carbon and nitrogen [28]. Other intermetallic phases which form in stainless steels include Laves ( $\eta$ ) and Chi ( $\chi$ ) phases [22].

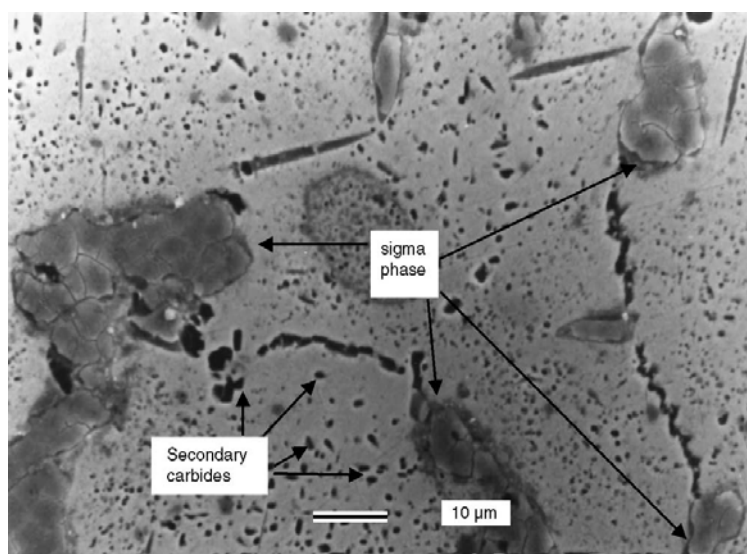


Figure 2-5: Heterogeneous precipitation of sigma phase on grain boundaries [29]

### 2.3.3. 475°C Embrittlement

The 475°C embrittlement occurs in ferritic stainless steels at temperatures between 400 and 550°C for prolonged exposure time. It is caused by segregation of Cr in ferrite. At these temperatures, ferrite separates into an iron rich magnetic component and a chromium rich non-magnetic component [30]. The damage is accelerated at a temperature of about 475°C and hence 475°C embrittlement. The 475°C embrittlement is accelerated by increasing chromium content and is accompanied by increase in hardness, tensile strength and yield strength with a corresponding decrease in ductility and toughness. This embrittlement can be removed by heating the steel to a temperature above 600°C and cooling rapidly to room temperature [23].



#### 2.3.4. Sensitisation

Ferritic stainless steels are susceptible to intergranular corrosion (also known as sensitization) after heat treatment or welding. In these type of steels, sensitization is induced by slow cooling through temperature range of 500-850°C and relieved by low temperature annealing treatments i.e. temperature below 500°C. The temperature range in which sensitization takes place is the range in which there is low solubility of carbon and nitrogen in ferrite. Due to fast diffusion rates of chromium and carbon in ferrite, the sensitisation kinetics of ferritic stainless steels is so rapid that material will only have chromium depleted grain boundaries when quenched from approximately 750°C or higher. If the samples are cooled slowly, it will become sensitized, but chromium will rapidly diffuse back during cooling to desensitize the grain boundary. Holding sensitised ferritic stainless steel at approximately 800°C will cause chromium to diffuse back to the depleted regions. Sensitisation can be overcome by one of the several methods all of which increases production cost:

- Reheating the alloys to temperature between 950 and 1100°C to dissolve chromium carbides and allowing Cr to diffuse back to Cr depleted zone
- Reduce interstitial levels by better control during steel making.
- Addition of strong carbide and nitride former such as Ti, Nb and zirconium tie up carbon and nitrogen. This will prevent the precipitation of Cr carbides. This addition of Ti, Nb and Zr is called stabilisation and will be dealt with in the next subsection.

#### 2.4. Ferritic stainless steel in automotive industry

Secondly, global warming and air pollution are amongst the major problems facing the world today. Strict environmental legislation on the emission of harmful gases from motor vehicles has, therefore, forced the automobile industry to search for alternative and cheaper materials for exhaust systems. In order to produce cleaner outlet gases, the exhaust temperature needs to be increased to approximately 900°C [5]. Purification reactions can be accelerated by introducing the exhaust gas reaction into the catalytic converter and high temperature can be maintained by reducing the

thickness of the exhaust manifold materials. This reduction on the exhaust manifold materials thickness contributes to overall weight reduction and as results traditional cast iron components are now being replaced by ferritic stainless steels [7].

The exhaust system is divided into hot and cold end. The hot end consists of exhaust manifold, front pipe, flexible pipe, catalytic converter and cold end consists of muffler and tail end pipe as shown in Figure 1-3 in chapter 1. Typical operating temperatures and materials currently used for exhaust system components are shown in Table 2-1 below. It can be seen form Table 2-1 that most parts are made of ferritic stainless steels grade containing 11% Cr except for those parts in more demanding heat and corrosion areas.

Table 2-1: Service temperature, steel grade and required properties for exhaust components [6, 31]

No.	Part	Service temperature (°C)	Steel grades	Required properties
1	Cylinder head gasket	100	301	High strength, superior bead formability
2	Exhaust Manifold	800-950	409, 441,309,321, 304	High temperature strength, oxidation resistance, thermal fatigue life and workability
3	Front pipe	600-900	409,436,304,321	
4	Flexible pipe		304, 321,316Ti,309	
5	Catalytic converter		441,409,321,309	High temperature strength, oxidation resistance, thermal shock resistance and workability, high temperature salt damage resistance
6	Centre pipe	300-600	409,304,441	Salt damage resistance

Ferritic stainless steels are mainly used in the automotive exhaust systems as a compromise between low carbon steels and higher cost, higher alloyed ferritic or austenitic stainless steels. The ferritic stainless steels offer better corrosion resistance and longer service life than low carbon steels. They are also relatively cheaper than the more highly alloyed stainless steels.

## 2.5. Stabilisation

To solve the problem of sensitisation, the carbon in ferritic stainless steels can be reduced through a combination of steel making practices and the addition of elements with strong affinity for carbon and nitrogen. These steels are processed firstly in an argon oxygen decarburisation (AOD) or vacuum oxygen decarburisation (VOD) to reduce the carbon content to very low level of less than 0.02%. Secondly, carbon can further be reduced through addition of Ti, vanadium, zirconium, tantalum and Nb. These stabilising elements form carbonitrides which precipitate at higher temperatures and shorter times than chromium carbides thus removing all of the carbon from solution before the chromium carbides can form and precipitate. These carbonitrides are found to be less harmful to the toughness of the ferritic stainless steels compared to chromium carbonitrides. Difficulty of getting tantalum and its cost makes it impossible to find any application in any cost effective structural components [32]. It was further stated that since vanadium does not play a role in significantly reducing the sensitisation, it is not commercially used as a stabilising element. This leaves us with Ti, Nb and Zirconium being used as stabilising element and this will be dealt with in the next subsection

It has been reported by Grubb [33] that toughness of ferritic stainless steels can be improved by addition of Nb up to full stabilisation and thereafter begins to decline. These excess stabilising alloying elements induce solid solution hardening and this reduces the toughness. It was further reported that this effect is more pronounced with Ti addition because it is a stronger solid solution hardener than Nb. It is evident from Figure 2-6 below that Ti has more pronounced effect in reducing DBTT than Nb. Zero Ti shows higher DBTT because no carbon and nitrogen was tied up and, therefore, more carbon was in solid solution which has negative effect on DBTT. The European Standard EN 10088-2:2005 [34] specifies that the minimum and maximum Nb and Ti required to stabilised ferritic steel grades should be as follows:

$$\text{EN 1.4512 (AISI 409):} \quad \text{Ti}_{\min} = 6 \times (\text{C} + \text{N}) \dots\dots\dots (2.1)$$

$$\text{EN 1.4512 (AISI 409):} \quad \text{Ti}_{\min} = 0.15 + 4 \times (\text{C} + \text{N}) \dots\dots\dots (2.2)$$

$$\text{EN 1.4509 (AISI 441):} \quad \text{Nb}_{\min} = 0.30 + (3 \times \text{C}) \dots\dots\dots (2.3)$$



The  $Ti_{free}$  and  $Nb_{free}$  i.e. the Ti and Nb in solution are given by the following expressions:

$$Ti_{free} = Ti - Ti_{min} \dots \dots \dots (2.4)$$

$$Nb_{free} = Nb - Nb_{min} \dots \dots \dots (2.5)$$

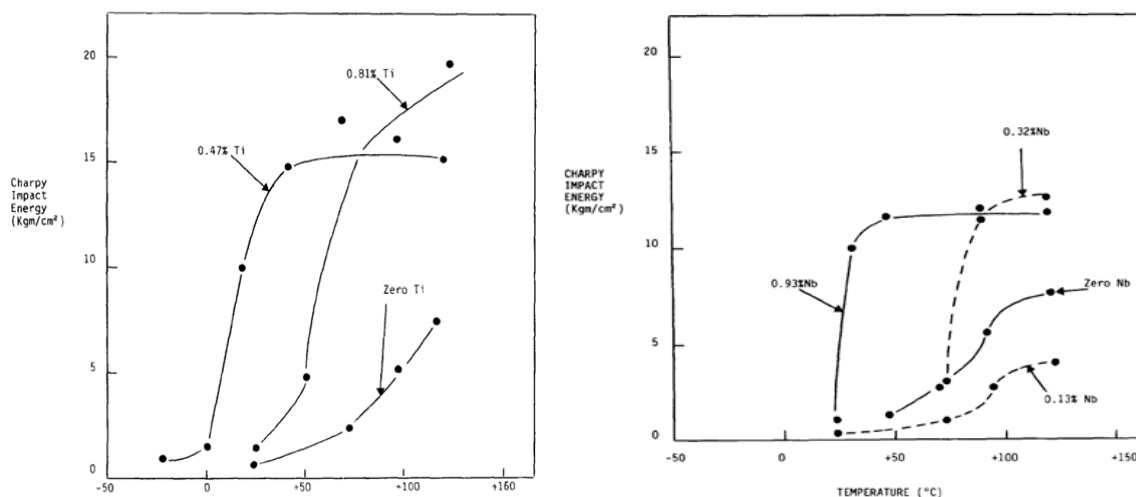


Figure 2-6: Effect of Nb and Ti addition to toughness of ferritic stainless steel [26].

The carbonitrides of Nb and Ti are beneficial in enhancing {111} texture through particle stimulation nucleation (PSN). Pickering and Lewis [35] showed the formation of {111} texture parallel to the rolling plane at the matrix/Nb(C,N) interface. This phenomenon was found in all steels containing undissolved particles of (Nb(C,N), Ti(C,N)). It was also observed that areas adjacent to the large and undeformed particles had high stored energy and, therefore, the effect was similar to that of higher levels of cold reduction.

### 2.5.1. Stabilisation with only Ti

Ti is the most commonly used stabilising element in stainless steels. This is highly reactive elements that forms TiN in the present of N and TiC in the presence of carbon. Ti forms titanium carbonitrides (Ti(C,N)) in the presence of carbon and nitrogen due to their mutual solubility of TiC and TiN. N/C ratio determines the TiN/TiC ratio in the Ti(C,N) [36]. The most recent stabilisation requirement for single stabilised steel is given by Equation 2.1 and 2.2 above. However the disadvantage of single Ti stabilised is that Ti stabilised stainless steels suffers from poor surface finish and causes large cubic Ti(C,N) to precipitate and reduced impact toughness



[32]. This negative effect of Ti can be minimised or reduced by the addition of Nb as discussed in the next section.

### **2.5.2. Ti and Nb dual stabilisation**

Gordon and Bennekom [36] reported that dual stabilisation of Ti and Nb results in superior mechanical properties of the weldment since the interstitial C and N are tied up. It was further reported that deleterious effect of each element is not fully realised since each is present in smaller quantities. Nb is relatively more expensive than Ti but this compensated by reduced production costs because of lowered or no surface grinding of defects. It has also been found that addition of Ti and Nb increases the corrosion resistance [5, 9] and increases formability [37, 38].

### 3. CHAPTER 3: PRECIPITATION AND NUCLEATION THEORY

In general, the solidification of a metal or alloys can be divided into the following steps:

- i) The formation of stable solid nuclei in the melt (nucleation) and
- ii) The growth of these nuclei into crystals (grains) and the formation of a grain structure.

Basically there are two main mechanism by which nucleation of solid particles in liquid metals occurs and they are homogeneous and heterogeneous nucleation. The choice between homogeneous and heterogeneous nucleation of a second phase is determined by the balance between chemical and other driving force which are negative and various retarding forces which are positive.

#### 3.1. Homogeneous nucleation

In homogeneous nucleation, the nuclei form at random in the matrix. It is generally accepted that homogeneous nucleation occurs very seldom and that practically heterogeneous nucleation occurs in most cases. The energy balance for precipitation and nucleation of second phase can be modeled mathematically by Equation 3-1:

$$\Delta G = \left(\frac{4}{3}\right) (\pi r^3 \Delta G_v) + \frac{4}{3} \pi r^3 \Delta G_\epsilon + 4\pi r^2 \gamma \dots\dots\dots 3-1$$

Where  $\Delta G_\epsilon$  is a strain energy (a retarding force) that arises out of the difference in volume or densities between the precipitates and solid solution in which it nucleates,  $\Delta G_v$  is the free energy released per unit volume of a new phase and  $\gamma$  is the surface energy of the new phase that has formed.

By taking the first derivative of Equation 6 with respect of  $r \left(\frac{d\Delta G}{dr}\right)$  at  $r = r^*$  and equate it to zero, the critical radius of the embryo that can become a nucleus and the activation energy required for that to form can be represented by Equation 3-2 and 3-3.

$$r^* = - \left(\frac{2\gamma}{\Delta G_v + \Delta G_\epsilon}\right) \dots\dots\dots 3-1$$

$$\Delta G^* = \left( \frac{16\pi\gamma^3}{(\Delta G_v + \Delta G_\epsilon)^2} \right) \dots \dots \dots 3-2$$

It is important to note the strong influence of the surface energy  $\gamma$  on the activation energy  $\Delta G^*$ . Therefore a conclusion can be made that nucleation is very sensitive to the value of the surface energy between the precipitation and the matrix and nucleation will take place easier in case of low surface energy between the precipitation and matrix.

Plotting Equation 6 shows the effect of nucleus size on the stability of the new nucleus as shown in Figure 3-1.

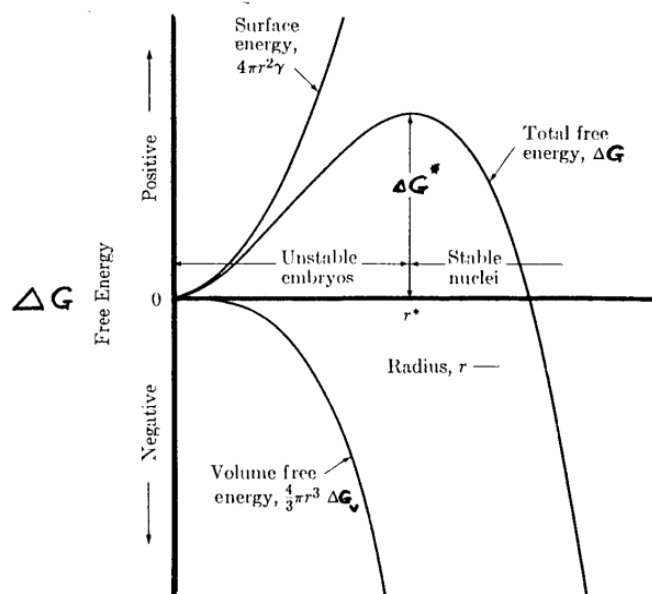


Figure 3-1: Free energy of formation of a stable nucleus.

At  $r = r^*$ , spontaneous growth of the nucleus will take place as  $r$  can now increase with a reduction in  $\Delta G$  taking place at the same time. The free energy released  $\Delta G_v$  can be increased by increasing undercooling, thus decreasing the critical nucleus size. In most cases it is difficult to obtain large undercooling for homogenous nucleation to take place hence heterogeneous nucleation is encountered very often.

### 3.2. Heterogeneous nucleation

Heterogeneous nucleation in the solid solution can take place on various defects or microstructural characterisation and these sites may include grain boundaries,

vacancies, dislocation and stacking faults. Only nucleation on grain boundaries will be discussed in this project.

When a nucleation takes place on a grain boundary as shown in Figure 3-2, a certain surface area of the grain boundary is removed from the system.

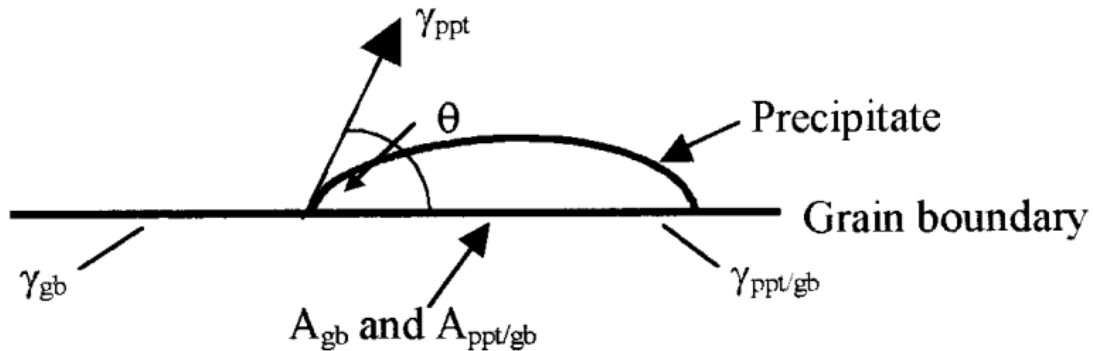


Figure 3-2: Heterogeneous nucleation of a precipitate on a grain boundary

This forms additional driving force for nucleation and must therefore have a negative sign in the basic free energy equation for nucleation as indicated in Equation 3-4

$$G = K_1(\Delta G_v + \Delta G_\epsilon) + K_2\gamma_{ppt}A_{ppt} + K_3\gamma_{ppt/gb}A_{ppt/gb} - \gamma_{gb}A_{gb} \dots 3-4$$

From Equation 3-4 it is clear that the system will preferentially select those higher energy grain boundaries where it will gain the most energy as an additional driving force. Figure 3-3 shows the relationship between the activation energy for grain boundary nucleation for the various possible grain boundary sites and the contact angle  $\theta$ .

It may be seen from Figure 3-3 that at a given contact angle  $\theta$ , nucleation on grain corners requires the lowest activation energy, then grain edges and lastly grain boundaries. The nucleation rates  $\dot{N}$  should therefore be ranked as follows:

$$\dot{N}(\text{grain corners}) > \dot{N}(\text{grain edges}) > \dot{N}(\text{grain surfaces})$$

Grain boundaries can also lower the retarding forces arising from the strain energy  $\Delta G_\epsilon$  and thereby create a new driving force. In case where the surface energy and the strain energy are lowered enough through nucleation on grain boundary, the

grain boundaries may become the preferred sites fully and no nucleation within the grains will occur.

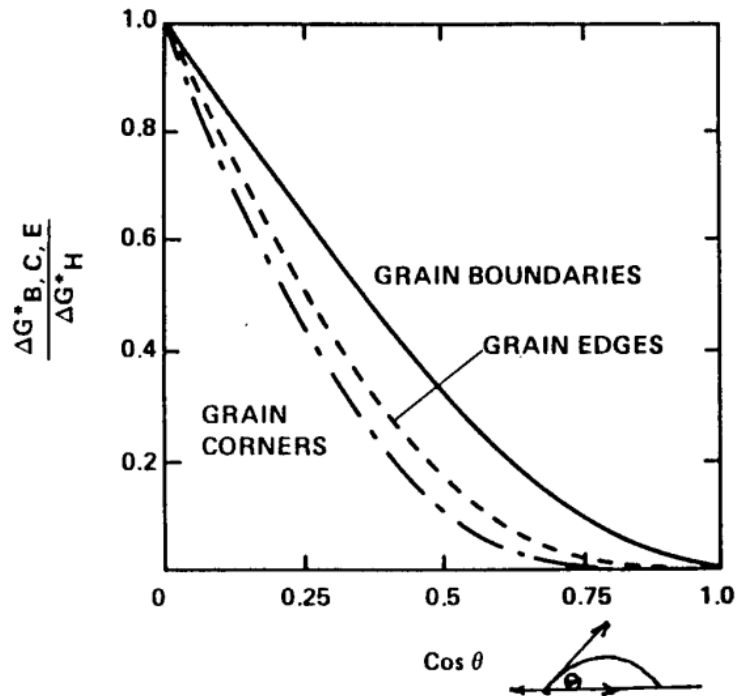


Figure 3-3: Relative activation energy for nucleation on grain boundaries, grain edges and grain corners to that for homogeneous nucleation as a function of a contact angle  $\Theta$ .

## 4. CHAPTER 4: TEXTURE IN FERRITICSTAINLESS STEEL

### 4.1. Introduction

Plastic flow causes the re-orientation of the lattice of individual grains of a polycrystalline material and tends to develop a preferred orientation of the lattice of the grains as well as a preferred change of shape of the grains with respect to the rolling direction [39]. Texture or preferred orientation is said to be present when materials consist of assembly of individual grains of which a significant proportion of that orientation cluster at a certain degree about some particular orientation [13]. Figure 4-1 shows a crystal arrangement of randomly textured materials and strongly cube textured materials in (111) pole figure. It is important to note from Figure 4-1 that iso-density contour lines cluster around the preferred pole orientations and this indicate that not all grains have exactly the same preferred orientation but a statistical spread around these orientations exists.

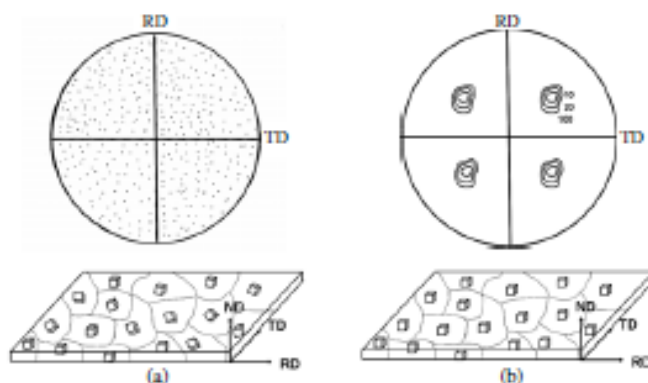


Figure 4-1: Crystal arrangement. a) shows a randomly textured material and b) strongly textured material corresponding to (111) Pole Figure [40].

Texture is solely a crystallographic condition and does not necessarily have any relationship with the grain shape, grain size and distribution [41]. Unique texture may arise during various metallurgical processing steps such as during solidification, deformation processes (such as deep drawing, cold or hot working, etc.), and recrystallisation after cold work [42, 43]. Texture determines the plastic anisotropy of the metals which is significant in applications such as deep drawing.

The following general statement are important regarding texture formation [39]:

- i. Texture is influenced by the hot working conditions particularly when dynamic recrystallisation occurs.
- ii. It is possible, in certain cases to minimize texture formation or develop a desired texture by controlling the cold or hot working and annealing schedule but it is difficult to produce free randomness
- iii. The plastic strains near the surface of the specimen may differ from those in the interior especially in rolling and wire drawing. These may produce textures that vary with depth below the surface also known as texture gradient.
- iv. Anisotropy of mechanical properties in some specimen maybe influenced by elongated or flattened inclusions, voids, fissures, grain boundaries and by texture of the grains.

Ray and Jonas [43] indicated that there are three principal processes that give rise to texture and its changes evolution and these are namely the deformation, recrystallisation and transformation texture. These will be discussed separately in the next subsection.

#### 4.2. The nomenclature of rolling textures

Texture maybe defined according to the orientation of grains with respect to the rolling direction by using the appropriate Miller indices as shown in Figure 4-2. Texture in rolled sheet metals is usually represented as  $\{hkl\}\langle uvw \rangle$ , where  $\{hkl\}$  is the plane parallel to the rolling plane and  $\langle uvw \rangle$  is the direction parallel to the rolling direction [44]. Rolling direction (RD), transverse direction (TD) and normal direction (ND) need to be used as the reference frame to the actual specimen for rolled sheet materials.

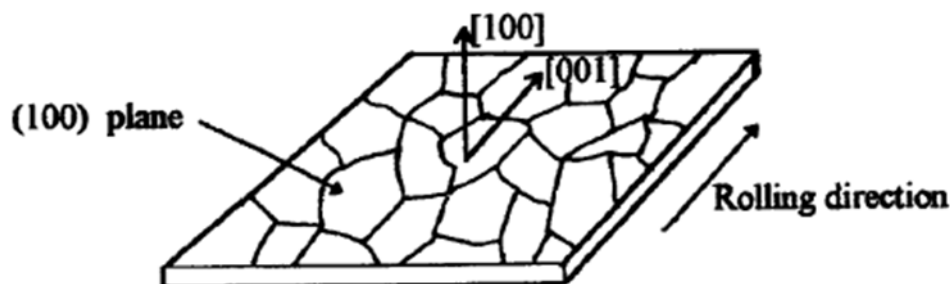


Figure 4-2: Definition of a  $(100)[100]$  texture with respect to the rolling direction.

The most important texture components for bcc steels are summarised in Table 4-1 below. It has been reported in literature that the most important rolling and recrystallisation texture components are represented in  $\phi_2 = 45$  section with boundaries  $0-90^\circ$  for  $\phi_1$  and  $\phi$  [15, 45].

Table 4-1: Summary of important fibres and texture components in BCC steels [46]

Fibre name	Fiber axis	Important components
$\gamma$ - fibre	$\langle 111 \rangle // ND$	$\{111\}\langle 100 \rangle, \{111\}\langle 112 \rangle$
$\alpha$ - fibre	$\langle 110 \rangle // RD$	$\{001\}\langle 110 \rangle, \{112\}\langle 110 \rangle, \{111\}\langle 110 \rangle$
$\eta$ - fibre	$\langle 001 \rangle // RD$	$\{001\}\langle 100 \rangle, \{001\}\langle 100 \rangle$
$\epsilon$ - fibre	$\langle 110 \rangle // TD$	$\{001\}\langle 110 \rangle, \{112\}\langle 111 \rangle, \{111\}\langle 112 \rangle, \{011\}\langle 100 \rangle$
$\zeta$ - fibre	$\langle 110 \rangle // ND$	$\{110\}\langle 112 \rangle, \{110\}\langle 110 \rangle$
$\beta$ -fibre	$\langle 110 \rangle // TD$	$\{111\}\langle 110 \rangle, \{111\}\langle 112 \rangle, \{557\}\langle 583 \rangle$

### 4.3. Graphical representation of texture

It should be stated beforehand that it is not easy to measure the texture in a polycrystalline as one increasingly deals with statistical parameters [41]. Firstly, not all the grains that are considered align themselves with a particular orientation lying exactly on that orientation and a statistical spread around the preferred orientation is to be expected. Secondly, measurement must be undertaken over a large number of grains and contour lines are usually plotted with a certain intensity of orientation. There are various methods of representing texture and the methods include using probabilities (p-values), pole diagram, orientation distribution functions (ODFs).

#### 4.3.1. Representation of texture by pole diagrams

Pole diagrams are essentially maps that indicate the number of planes from a particular family of planes that lie at a particular angle to some reference direction. Rolling direction (RD), transverse direction (TD) and normal direction (ND) need to be used as a reference frame to the actual specimen for rolled sheet materials. Typical texture representation by pole figures is shown in Figure 4-3, which was determined by X-ray goniometer and is represented as a stereographic projection showing the variation in the pole density for a selected set of crystal planes.



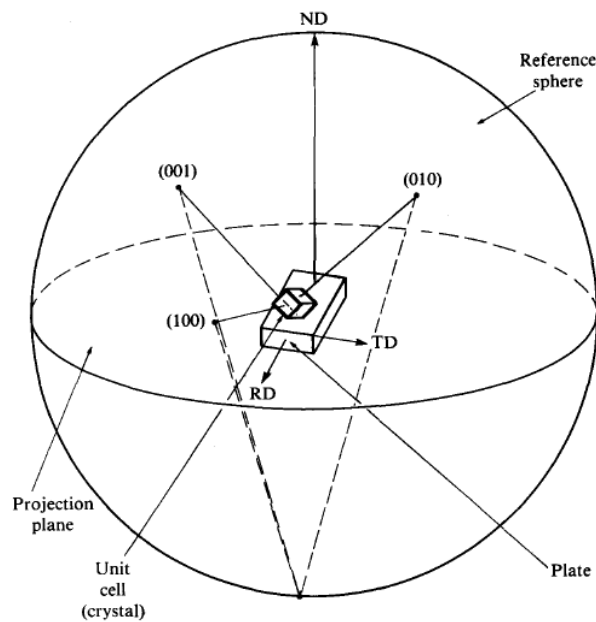


Figure 4-3: Schematic representation of the construction of a pole figure [13].

For a rolled sheet, the rolling plane normal (ND) is pointed towards the north pole of the sphere as shown in Figure 4-3. For each grain in the sample, a set of crystallographic equivalent direction is chosen and projected on the equatorial plane as shown in Figure 4-3. The intersection of all points of the  $\langle 100 \rangle$  direction on the equatorial plane is called (100) pole figure. It has been reported in literature that even though a pole figure of a polycrystalline material contains information regarding the crystallographic orientation of all grains, it is not simple to extract information from an experimentally determined pole figure. For a large number of grains in a polycrystalline material, poles may overlap on the pole figure, so that the true orientation density is not clearly represented. In that case, contours tend to be used instead [47]. The most common way is to draw contour lines of equal orientation density in the pole figure as shown in Figure 4-4 below. Regions of high pole density have a high number of contours, while regions with low pole density have sparsely spaced contours. Some researchers prefer to plot the density spots than contouring as shown in Figure 4-5.

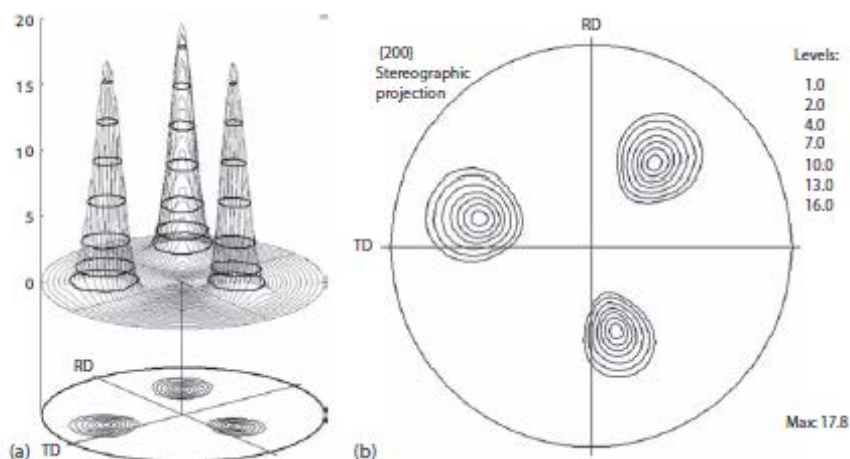


Figure 4-4: Contouring of a 3-D pole density distribution to derive the standard 2-D pole figure presentation [47].

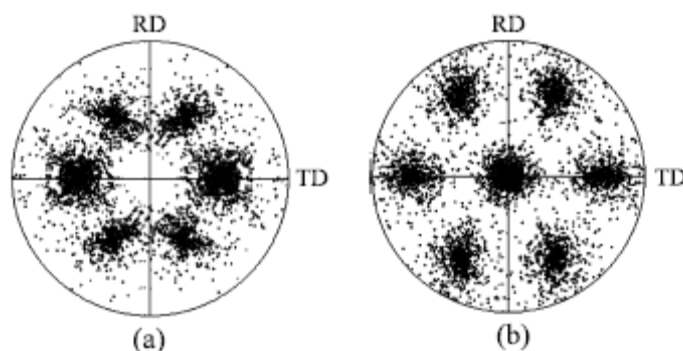


Figure 4-5: Pole Figures of  $\{111\}\langle 112 \rangle$  orientation from a cold rolled high strength steel corresponding to a series of Gaussian Distribution with scatter width of  $15^\circ$ , a)  $\{100\}$ , b)  $\{111\}$  Pole Figure [48].

4.3.2. Texture Representation by means of Orientation Distribution Function (ODF)  
Pole diagrams described above generally provide only texture information in a qualitative sense and at best semi-quantitative [43, 47] as it does not give information about orientation relationship of a particular crystal relative to the rest of them. Therefore one way of removing this difficulty is to use the crystallite orientation distribution function (CODF or ODF), which essentially describe the frequency of occurrence of a particular orientation in a three dimensional (Euler) orientation space [43]. To obtain ODF, at least three pole figures are required.  $\{100\}$ ,  $\{211\}$  and  $\{222\}$  are typical pole figures required to obtain ODF in BCC materials.

In an ODF, each orientation point on a pole figure is replaced by a Gauss-type series expansion method at defined widths and ODF's for angles  $\varphi_1$  ( $0^\circ$  to  $90^\circ$ ) and  $\Theta$  ( $0^\circ$  to  $90^\circ$ ) are plotted in Euler space as discussed in the next sub-section. They provide information concerning the quantity of materials or volume fraction associated with each orientation and thus permits conclusion to be drawn about mechanism of recrystallisation.

If one denotes by  $dV$  the total volume of all elements of the sample which possess the orientation  $g$  within the elements of orientation  $dg$  and by  $V$ , the total sample volume, then orientation distribution function  $f(g)$  is defined by equation 4-1[44].

$$\frac{dV}{V} = f(g) dg \dots \dots \dots 4-1$$

$$\text{where } dg = \frac{1}{8} \pi^2 \sin\phi d\phi d\varphi_1 d\varphi_2$$

The integral of the ODF over all possible orientation should be equal to 4-1.

#### 4.3.2.1. Euler angles

Mathematical methods have been developed to allow an ODF to be calculated from the numerical data obtained from several pole figures. The most widely used notations employed for the description of ODFs are those proposed independently by Bunge [44] and Roe [49]. They use generalized spherical harmonic functions to represent crystallite distributions. Bunge use Euler angles ( $\varphi_1, \Phi, \varphi_2$ ) to describe the crystals rotations, the set of angles employed by Roe are referred to as  $\psi, \Theta$ , and  $\Phi$ . These two sets of angles are related to each other as follows:

$$\varphi_1 = \frac{\pi}{2} - \psi, \quad \Phi = \Theta, \quad \varphi_2 = \frac{\pi}{2} - \Phi$$

Euler angle defines the difference between orientation between the crystal axes and the deformation axes (i.e. RD, ND and TD) as depicted in Figure 4-6 and when performed in the correct sequence as shown by arrows in Figure 4-7, transforms the specimen coordinate system onto the crystal coordinate system. Two different coordinate systems are defined with the first one connected to the sample axis  $X_i$  and the second to the crystal or the grain  $X_i^c$ .

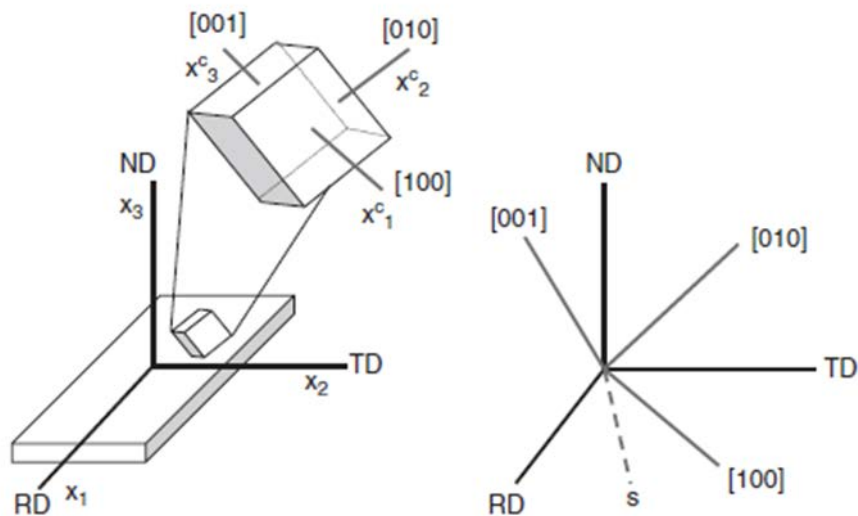


Figure 4-6: Orientation of the crystal axis system and the sample axis system, s is the intersection of the planes (RD-TD) [50].

From the definition of Euler angles it follows that they are periodic with period  $2\pi$  and thus holds:

$$g\{\varphi_1 + 2\pi, \phi + 2\pi, \varphi_2 + 2\pi\} = g\{\varphi_1, \phi, \varphi_2\} \dots \dots \dots 4-2$$

In more general case, the Euler angles are defined in the range  $0^\circ \leq \varphi_1, \varphi_2 < 360^\circ$  and  $0^\circ \leq \phi \leq 180^\circ$ .

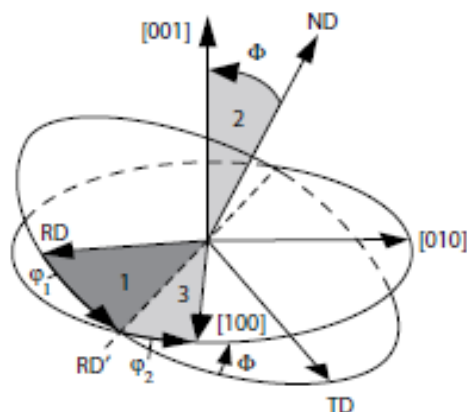


Figure 4-7: Diagram showing how through the Euler angles in the order 1, 2, 3 [47].

#### 4.3.2.2. Euler space

A three dimensional view of the Euler space in the Bunge notation is presented in Figure 4-8. Euler space is defined by Euler angles  $(\varphi_1, \phi, \varphi_2)$ , which constitute a set of three consecutive rotations that bring the crystallographic  $\langle 100 \rangle$  axes to each crystalline into coincidence with a specimen axes as shown in Figure 4-6.

Each point on the Euler space correspond to a particular rotations and conversely each rotation of crystal orientation leads to a point in the three dimensional space. Through appropriate software, the actual three dimensional orientation distribution functions at any preset density level in a cube may also be plotted as shown in Figure 4-8.

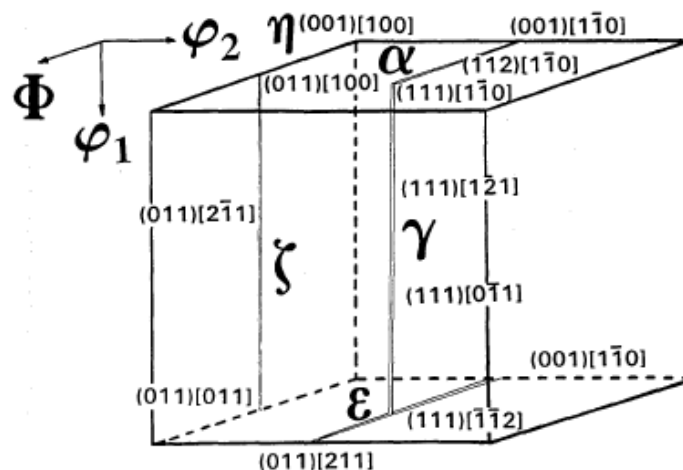


Figure 4-8: Reduced Euler space with some important fibres and orientations [46].

#### 4.3.2.3. Two dimensional representation of ODF

For practical reasons, ODF are not represented in the 3 dimension (3D) Euler space but 2 dimension sections of the Euler space. The example of ODF in 2D is shown in Figure 4-9.

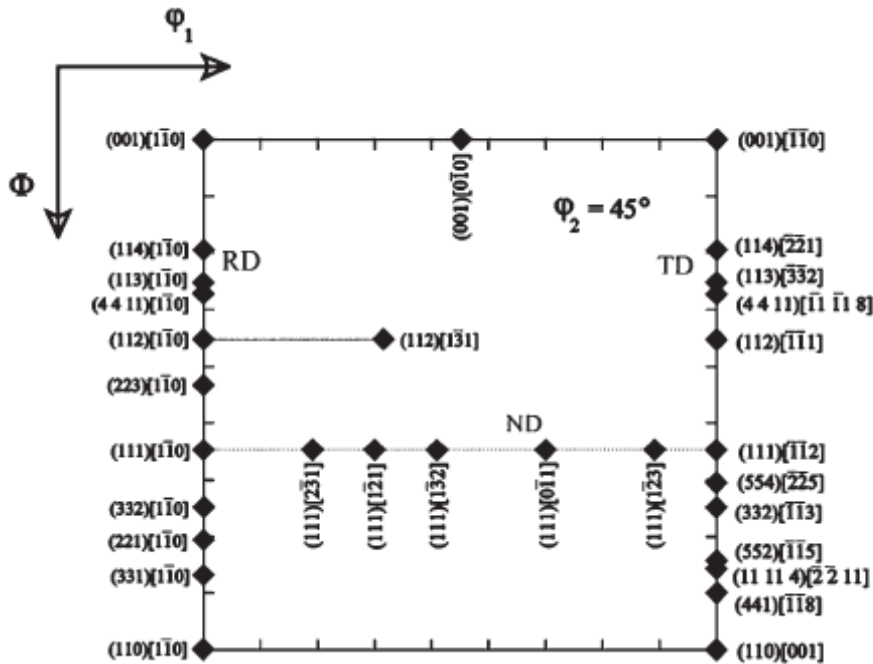


Figure 4-9: Schematical representation of some orientations and texture fibres which are relevant for BCC materials at  $\phi_2 = 45^\circ$  [15].

The representation described above is known as the Bunge notation [44]. The orientations lying along the RD fiber are related by rotations around the RD //  $\langle 110 \rangle$  axis and the fibers lies along  $\phi_2 = 45^\circ$  in the  $\phi_1 = 0^\circ$  section. The TD fibers contains orientation that have a common  $\langle 110 \rangle$  // TD and this fibers lies along  $\phi_2 = 45^\circ$  in the  $\phi_1 = 90^\circ$  section. Orientations on the ND fiber have a common  $\langle 110 \rangle$  // ND and this fiber extends parallel to the  $\phi_1$  axis at  $\phi_1 = 55^\circ$  and  $\phi_2 = 45^\circ$  [43].

#### 4.3.3. Texture measurement by probability-values (P-values)

P values represent the probabilities of a particular diffracting plane lying in or nearly parallel to the plane of the sheet and it is expressed as shown in Equation 4-3 [16]:

$$P_{hkl} = \frac{\frac{I_{(hkl)}}{R_{(hkl)}}}{\frac{1}{n} \left( \sum_{hkl}^n \frac{I_{hkl}}{R_{hkl}} \right)} \dots\dots\dots 4-3$$

where  $I_{hkl}$  is the diffraction intensity from a particular family of (hkl) planes and  $R_{hkl}$  is the corresponding intensity for a specimen with random distribution. P value is used

as a rapid indication of texture changes as well as an assessment of the influence of texture on deep drawability. Higher values  $P_{111} : P_{100}$  ratio are associated with higher  $r$ -values which leads to better drawability.

#### 4.4. Texture measurement

##### 4.4.1. Texture measurement by SEM-EBSD

This technique is the most popular technique used to measure texture due to the ease of availability and operation of SEM and it does not require much background in texture theory from the user. In order to produce EBSD pattern using SEM, the following steps need to be followed:

- i) Tilt the specimen so that its surface makes an angle of  $70^\circ$  with the horizontal in order to have more electrons diffracted
- ii) Turn off the scan coil to obtain a stationary electron beam,
- iii) Place the recording medium in front of the tilted specimen to capture the diffraction pattern.

Randle and Engler (2010) reported that the main effect of tilting the specimen is to reduce the path length of electron that have been backscattered by lattice planes as they enter the specimen, thus allowing a far greater proportion of these electron to undergo diffraction and escape from the specimen (having lost virtually more of their energy) before being absorbed. When the specimen is flat, as in the case of a conventional SEM, the path length and hence absorption of the backscattered electrons is too good to produce detectable diffraction.

The principles of texture measurement using SEM-EBSD method are as follows [40, 51]: In the SEM-EBSD, the intensity of the electron beam with the uppermost surface layer of the sample produces electron back scatter diffraction pattern (EBSD) that is analogous to Kikuchi pattern in the transmission electron microscope (TEM). EBSD are captured on a phosphor screen and recorded with a low intensity video camera or a CCD device. The beam is made to scan the area of interest and in case of large scans, the sample is translated using a high precision mechanical stage in



increments as small as  $0.1\mu\text{m}$ . At each position an EBSD is recorded. With a phosphor screen, back scattered electron are converted to light and this signal is transferred into camera. The digital signal is then entered into a computer and indexed. Specimen coordinate, crystal orientation, parameters describing the pattern quality and a parameter evaluating the pattern match are recorded. The sample is then translated to the next position and the procedure is repeated. The schematic set up of EBSD measurement is shown in Figure 4-10.

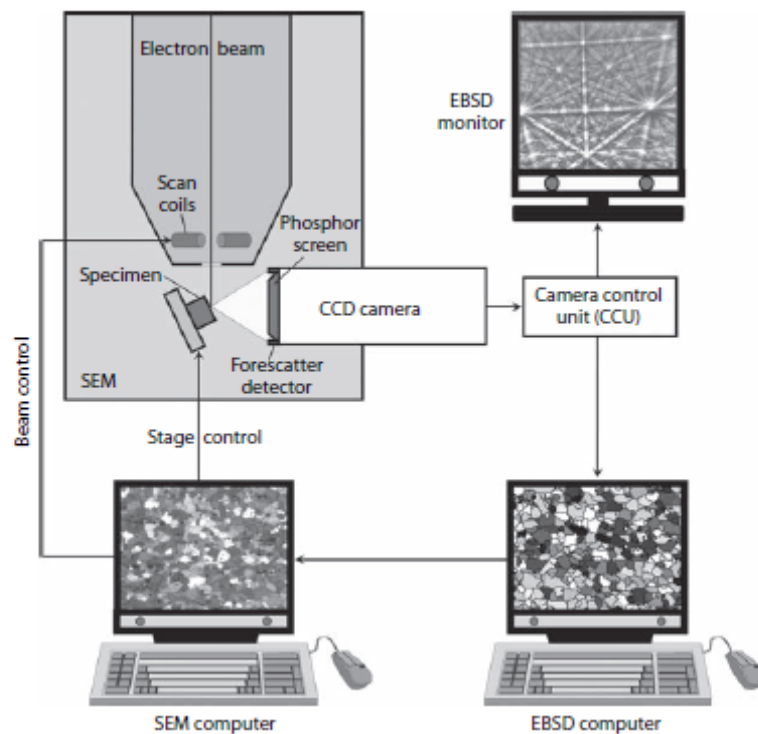


Figure 4-10: Schematic of EBSD measurement setup [47]

A spatial resolution of less than  $0.1\mu\text{m}$  can be reached on SEM equipped with a field emission gun. The biggest advantage of EBSD is the fact that it is the only technique that provides localised texture information in a quantitative manner. Therefore it helps bridge the gap between bulk texture measurements technique like X-rays and localised TEM techniques. EBSD is only applicable to crystals with fairly dislocation densities, surface preparation is critical and the automatic indexing procedure is not always reliable. Failure to index and mis-indexing of pattern, both of which are



orientation dependent, can produce texture artefacts. There are also statistical limitations when using EBSD technique.

It is important to note that EBSD measures the local texture of the materials which allows identifying nucleation and growth mechanism responsible for development of texture [18]. Furthermore, the basic fundamental mechanisms responsible for recrystallisation texture are not identified by XRD.

#### **4.4.2. Texture measurement by X-Ray diffraction**

The intensities of the various texture components of pole figures can be measured with an X-ray Diffractometer. X-ray diffraction is the oldest and still commonly used method for texture measurement. It was first employed by Wever in 1924 to investigate texture in metals and with the introduction of goniometer; pole figures can be directly recorded. Schultz in 1949 initiated modern quantitative X-ray for texture analysis and the principles of texture measurement using Schultz method are as follows [40, 42, 47, 51]:

A reflection specimen is mounted on the goniometer as shown in Figure 4-11 and the specimen is subjected to the three types of movement. The movements are:

- i) Simple translation to and fro which improves the statistical averaging of the texture measurement by increasing the number of grains that are measured,
- ii) Rotation about an axis perpendicular to the sheet surface (angle  $\varphi$ ) and
- iii) Rotation about the orthogonal areas through an angle  $\Theta$

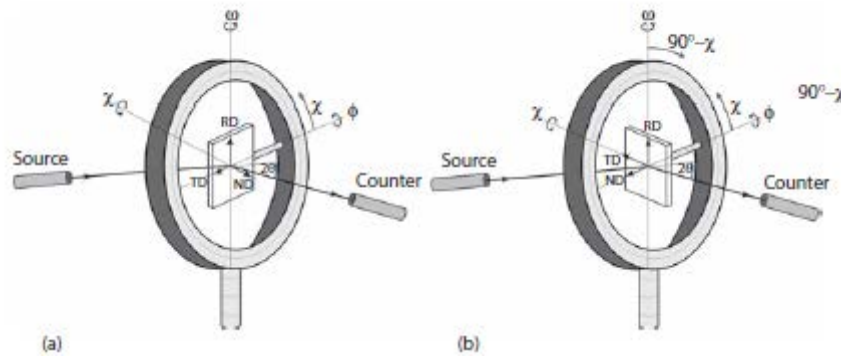


Figure 4-11: Diffraction in four circle texture goniometer with definition of the instrument angle. a) transmission geometry b) reflection geometry [47]

In order to determine the orientation of a given lattice plane ( $hkl$ ), the Diffractometer is first set to the adequate Bragg angle ( $\Theta_B$ ) of the diffraction peak of interest. The sample is rotated in a goniometer until the lattice plane is brought in reflection conditions (i.e. normal to lattice plane or diffraction vector which is the bisectrix between incident and diffraction beam) see Figure 4-11a. The reference point of the rotation is the rolling direction.

Determination of texture can be done on a sample of large thickness or a plane surface on which x-rays are reflected on a thin sheet which is penetrated by X-rays. Because of the defocusing effects as the flat sample is inclined against the beam, variation in the irradiated volume and absorption intensity corrections are necessary particularly in reflection geometry. The following number of adjustment can be made to minimise the defocusing errors:

- i) A narrow divergence slit is desirable, but this also jeopardise the total count rate and statistical significance of the measurement,
- ii) A wide receiving slit offsets the defocusing effect to some extent but also reduce the peak to background ratio,
- iii) Defocusing effects and other geometrical imperfection are most severe when the Bragg angle is small (less that about  $15^\circ$ ). A larger Bragg angle maybe selected by changing to a longer wavelength radiation or even by

using a high order reflection although this usually results in a severe reduction in count rate.

In reflection geometry, only incomplete pole figures can be measured usually to a pole distance of  $80^\circ$  from the sample surface normal. The schematics of texture measurement in Schulz geometry are shown in Figure 4-12.

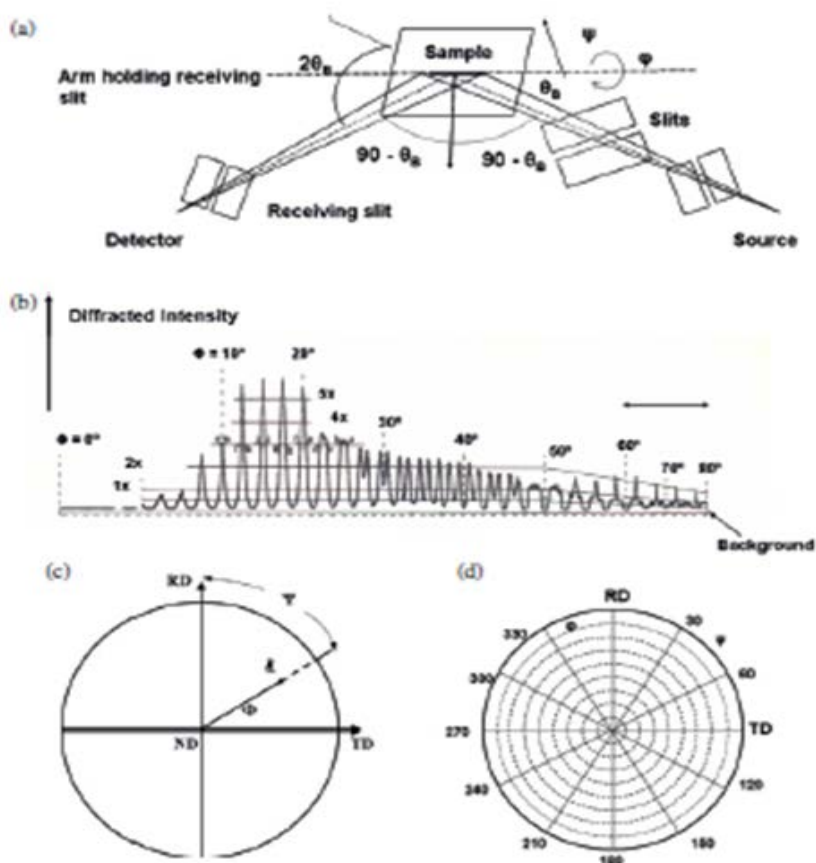


Figure 4-12: Schematic of texture measurement in Schultz reflection geometry [42].

Figure 4-12(a) above shows the diffraction geometry for a given sample orientation, Figure 4-12(b) shows the intensity variation of a given peak (hkl) as a function of different inclination and rotation, Figure 4-12(c) the position of a pole at an inclination  $\phi$  and Figure 4-12(d) shows the trace of a pole on a concentric chart.

#### 4.5. Deformation and recrystallisation texture in ferritic steels

The Study of deformation and recrystallisation texture in ferritic stainless steel and low alloy steels is made somewhat more difficult due to two factors [52]:

- i. The BCC lattice structure of  $\alpha$ -Fe or Fe-C steels does not have a uniquely defined slip system as is the case with FCC. This is due to lack of closed packed planes in the BCC structure. Occurrence of cross slip is therefore common in the Fe-C during cold working deformation and produces so called wavy slip lines.
- ii. During hot working or solution treatment, these steels are frequently taken into the austenite temperature range and upon cooling, they experience phase transformation to ferrite and this will further affect the grain orientation with respect to former austenite grain orientation.

#### 4.5.1. Deformation texture BCC steels

When the metal is deformed, its grains are re-oriented with a certain orientation being preferred orientation over others [30]. It was also observed that the preferred orientation or texture is influenced by at least four factors and these are: the type of deformation, amount of deformation, temperature of deformation and the mechanism of slip in the metal [30].

Leslie [53] and Hosford [54] have shown that unique deformation textures generally appear after rather heavy cold work reductions of more than 50% and these appear to have principally  $\alpha$ -fibre-like texture of  $\{001\}\langle 110 \rangle$ , although other texture components are usually also present.

As the amount of deformation or cold reduction increases, crystals rotations occur in polycrystalline along the following paths:

- I.  $\{100\}\langle 100 \rangle \rightarrow \{001\}\langle 110 \rangle \rightarrow \{112\}\langle 110 \rangle \rightarrow \{223\}\langle 110 \rangle$
- II.  $\{110\}\langle 001 \rangle \rightarrow \{554\}\langle 225 \rangle \rightarrow \{111\}\langle 112 \rangle \rightarrow \{223\}\langle 110 \rangle$

The preferred orientation resulting from deformation is strongly dependent on the slip and twinning systems available for deformation but is not generally affected by processing variables such as die angle, roll diameter, roll speed and reduction per pass [55]. The formation of strong preferred orientation will results in anisotropy in mechanical properties.

#### 4.5.1.1. Typical deformation texture in ferritic stainless steel

Typical cold rolling texture in bcc materials consists of two fibers through Euler angles. The two fibers are  $\alpha$ -fiber which consists of grains with a  $\langle 110 \rangle$  axis parallel to the RD and  $\gamma$ -fiber which consists of grains with a  $\langle 111 \rangle$  direction parallel to the normal direction. During cold rolling, the intensities along the  $\alpha$ - fiber will emerge the highest but in general  $\alpha$  and  $\gamma$ -fiber are clearly present in most cold rolling texture of steels.

#### 4.5.2. Annealing texture

In general annealing consists of heating materials to a specified temperature for a predetermined length of time. The purpose of annealing is to relieve residual stresses induced by prior processing and soften the steel for improved machinability or formability. Microstructure undergoes a sequence of change during annealing and they are recovery, recrystallisation and grain growth. Hu [56] reported that during recovery, there is no change in texture. Recrystallisation of deformed materials occurs by nucleation of new undeformed grains and their subsequent growth into the deformed matrix. New orientations due to twinning also occur during recrystallisation in materials with low stacking fault energy and on the contrary, in high stacking faults materials, twinning is not common during recrystallisation. Therefore recrystallisation generally causes a change in the distribution of the crystallographic orientation of the grains and consequently in the crystallographic texture of materials.

Annealing of cold worked metals produces a preferred orientation called annealing or recrystallisation texture which can either be stronger than or different from the deformation texture. Many industrial materials receive their final forming operation in annealed conditions, and, therefore the understanding of recrystallisation texture is very important. Annealing texture arises from dislocation rearrangements in the deformed grains, recrystallisation of the deformed grains (primary recrystallisation) and subsequent grain growth (secondary recrystallisation) [39, 57].

Annealing texture formation depends on a number of processing variables, the amount and type of deformation preceding annealing, the composition of the alloy, grain size, annealing temperature and time, and the texture produced by deformation

[55]. A good way of maximising a recrystallisation texture in ferritic stainless steel is first to produce a strong preferred orientation by a heavy reduction and then use high annealing temperatures [15].

#### 4.5.2.1. Interpretation of annealing texture

There are two theories used to interpret the formation of annealing texture [18, 58]:

- i. Orientation growth theory of recrystallisation proposes that nuclei with many orientation forms but due to the fact that the grain growth rate of any given nucleus depends on the orientation difference between the deformed matrix and growing crystal. Therefore the recrystallisation texture will arise from those nuclei that have fastest growth rate in the cold worked materials.

Mathematically, this may be expressed as follows:

$$\frac{G_T}{G_R} = \beta = \frac{d^3_T}{d^3_R} \quad \dots\dots\dots 4-4$$

where  $G_T$  is the growth rate of those nuclei with the texture orientations and  $G_R$  is the growth rate of those nuclei with random orientation. When  $\beta < 1$ , no preferred orientation will be observed and when  $\beta \gg 1$ , a preferred orientation will develop out of a large number of nuclei with a particular texture orientation.

- ii. Orientation nucleation theory of recrystallisation texture assumes that grain boundaries or special grains acts as preferred sites for nucleation. Mathematically, this maybe expressed as follows

$$\frac{N_T}{N_R} = \alpha \quad \dots\dots\dots 4-4$$

Where  $N_T$  is the number of recrystallisation nuclei with preferred orientation and  $N_R$  is the number of nuclei with random nuclei. When  $\alpha < 1$ , no preferred texture will be observed and when  $\alpha \gg 1$ , a preferred texture will develop out of the larger number of nuclei with a particular texture orientation.

In ferritic steels, the recrystallisation texture of the elongated fibrous grains appears to be of overriding importance in obtaining good drawability properties [48]. It appears in particular that a  $\gamma$ -fibre texture of  $\langle 111 \rangle // ND$  imparts good drawability to

low carbon steels although  $\alpha$ -fibre texture of  $\langle 110 \rangle // RD$  is usually also present in significant quantities.

In a study by Hölscher et al [59] on texture of AISI 430 ferritic stainless steel, it was similarly found that the so-called  $\alpha$ -fibre  $\langle 110 \rangle // RD$  increases during cold rolling with the  $\gamma$ -fibre  $\langle 111 \rangle // ND$  appearing after heavy cold work. During recrystallisation annealing, however the volume fraction of the  $\alpha$ -fibre decreased and that of the  $\gamma$ -fibre increased.

#### **4.6. Effect of texture on roping or ridging in ferritic stainless steel**

Ferritic stainless steel sheets containing 11-17% Cr tend to form undesirable surface corrugations or small ridges/ropelike marks called ridging when the sheets are pulled or deep drawn [60]. These undesirable surface conditions occur or form parallel to the rolling direction [12] and extend over the whole sheet with their width reaching 1 to 2 mm in the transverse direction [61]. Shin et al [60] observed that these ridges have a depth in the range of 20-25 $\mu$ m and can be distinguished from stretcher strains. Stretcher strains occur at an elongation of about 5% while ridging becomes noticeable at a stage of more 5% elongation as shown in Figure 4-13 below and the amplitude increases with the increase in strain until the specimen breaks.

This phenomenon has negative effect on the appearance of decorative items and expensive, time consuming grinding and polishing operation must be employed to remove it [11]. Considerable research has been conducted over the past four decades to understand the causes of ridging. Research has shown that ridging is known to have the following characteristics [62, 63].

- i. Appearance of ridging is related to the development of the columnar structure during solidification of the ingot and distribution of banded martensite or ferrite structure in the hot rolled sheet.
- ii. Combination of high r-valued  $\{111\}$  and low r-valued  $\{100\}$  orientation in the recrystallisation texture of final products may lead to ridging.
- iii. Addition of Ti or Nb to tie the carbon in the form of carbides promotes extensive nucleation of recrystallised grains which reduces ridging.



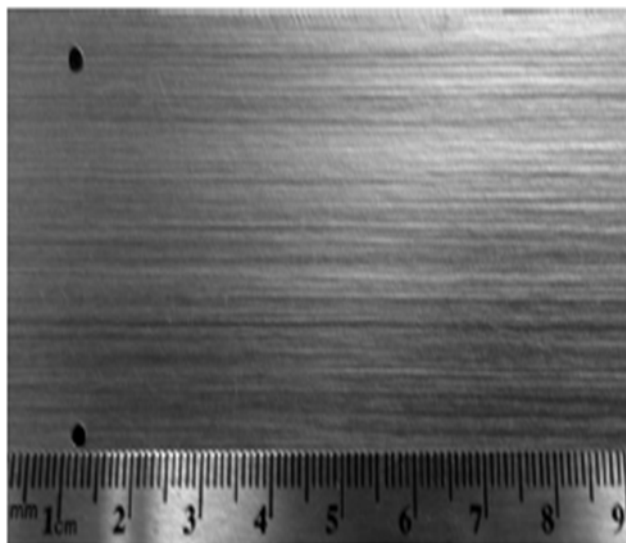


Figure 4-13: Ridging under uniaxial tension in the RD at 25% elongation in 17% Cr ferritic stainless steel [64].

In the study by H. J Shin et al [60] on the effect of texture on ridging of ferritic stainless steel, it was found that the lower plastic strain ratio of the  $\{001\}\langle 110\rangle$  colonies and difference in shear deformation between the  $\{111\}\langle 110\rangle$  and  $\{112\}\langle 110\rangle$  colonies results in ridging. Therefore, it was concluded that it is beneficial to eliminate the colonies for the good surface quality of ferritic stainless steels. They also studied the effect of microstructure and chemical composition on ridging in AISI 430 and 409L stainless steel. In this study it was found that for the same composition, initially columnar structured specimen showed more severe ridging than equiaxed specimen and 409L steel showed more severe ridging than 430 ferritic stainless steel. Therefore, for minimum ridging, the microstructure of the steel should essentially consist of equiaxed structure. It was further reported that long grain colonies with similar orientation develop from the columnar grains during cold rolling and survive even after annealing because they are not recrystallised. These colonies exhibit different plastic anisotropy from the matrix and this result in ridging. Wei et al [63] found that ridging is mainly due to the inhomogeneous distribution of the shear strain and this inhomogeneity may be due to the banded distribution of texture components along the rolling direction.



de Abreu et al [15] studied the effect of high temperature annealing on texture and microstructure of an AISI 444 ferritic stainless steel and it was observed that samples cold rolled at 30% and 60% and subsequently annealed at 1010°C presented microstructure, texture and  $R_m$  values suitable for deep drawing. The main texture component was found to be  $\{111\}\langle 112 \rangle$  and contain no component in the (100) plane. It was also found that the increase of the annealing temperature from 955 to 1010°C did not influence grain size. Huh and Engler [14] studied the effect of intermediate annealing during cold working on texture, formability and ridging of 17%Cr ferritic stainless steel sheet. It was found that intermediate annealing at 700°C for 1hour during cold working led to a weak rolling texture. After recrystallisation, this gave rise to a strong  $\{111\}$ //ND ( $\gamma$ -fibre) texture. This was proven by an increase in the  $R_m$ -value and the improvement in formability of the sheets. It was further concluded that materials rolled with intermediate annealing showed much less severe ridging than the ordinary rolled sheet as shown in Figure 4-14 below.

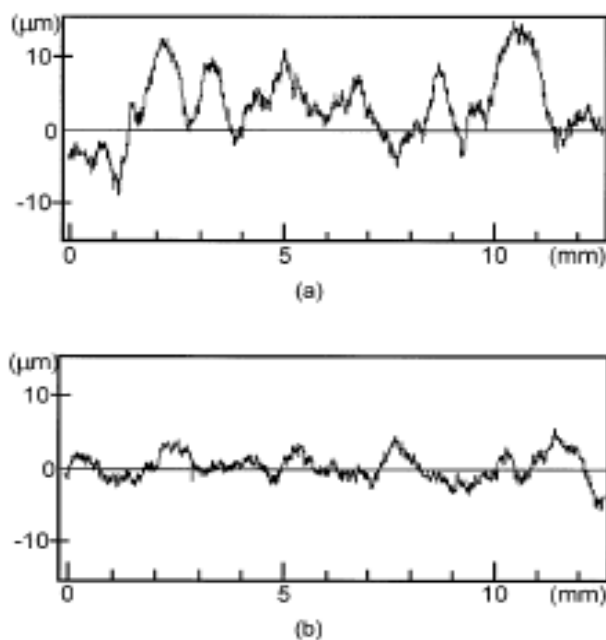


Figure 4-14: Roughness profiles of two differently processed materials to analyse ridging phenomenon. (a) One-step cold rolling (80%). (b) two-step cold rolling 60% then 50% [14].

Sheppard et al [10] studied the roping phenomena in ferritic stainless steels and it was found that roping can be reduced by introducing recrystallisation annealing, thus

fracturing bands of similar sized colonies of grains and producing a more homogeneous grain distribution. It was concluded that the main cause of roping is the inhomogeneity of the developed substructure and because of this, a number of related factors affect roping phenomenon. The hot rolling temperature must be controlled because high temperatures cause grain growth before rolling which promotes banding during deformation. Excessive Grain growth must be avoided during hot rolling as this causes banding during deformation and orange peel which mask the roping phenomenon.

#### 4.6.1. Chao's Model

In Chao's model [65], ridging was attributed to plastic strain ratio differences between the ND//<100> and ND//<111> components when extended in the rolling direction. Chao has shown through crystal plasticity theory that {100}<100> contracts in the directions perpendicular to the sheets plane upon extension in the rolling direction while {111}<110> cube on corner texture shows much less or no contraction in this direction along with substantial compressive strains across the width of the steels as indicated in the Figure 4-15 below. However it was found by Wright [67] that the most drawback about Chao's model is that the deformed outline of the surface is far from that of real materials which shows undulations.

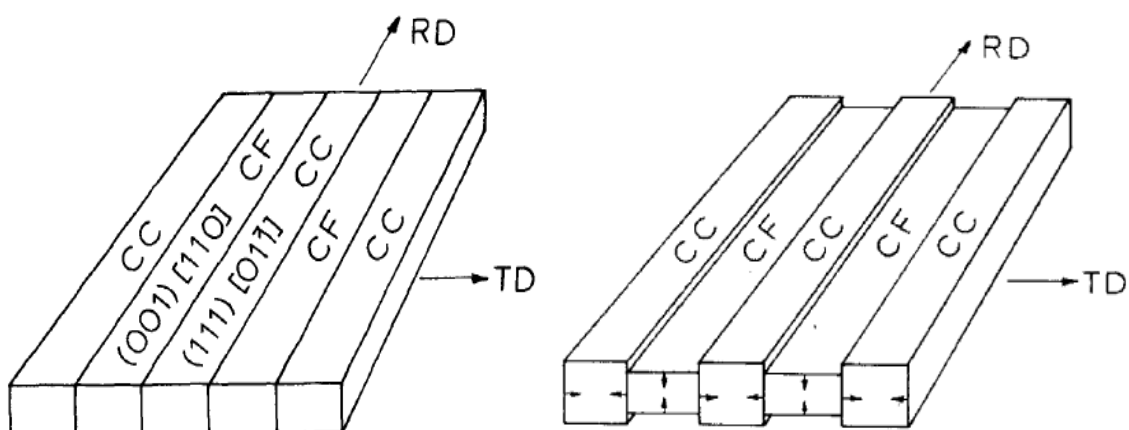


Figure 4-15: Schematic drawing of Chao's model [65].

#### 4.6.2. Takechi's model

Takechi's model focused on different shear strains between RD//<110> [66]. In this model, the ridging phenomenon was found to be caused by the shear strain of crystals having RD//<011> orientation. Takechi and co-worker through crystal plasticity calculation argue that a certain rolling texture of {hkl}<011> as shown in Figure 4-16a will deform to a final shape shown by Figure 4-16b when subjected to uniaxial tensile elongation in the rolling direction.

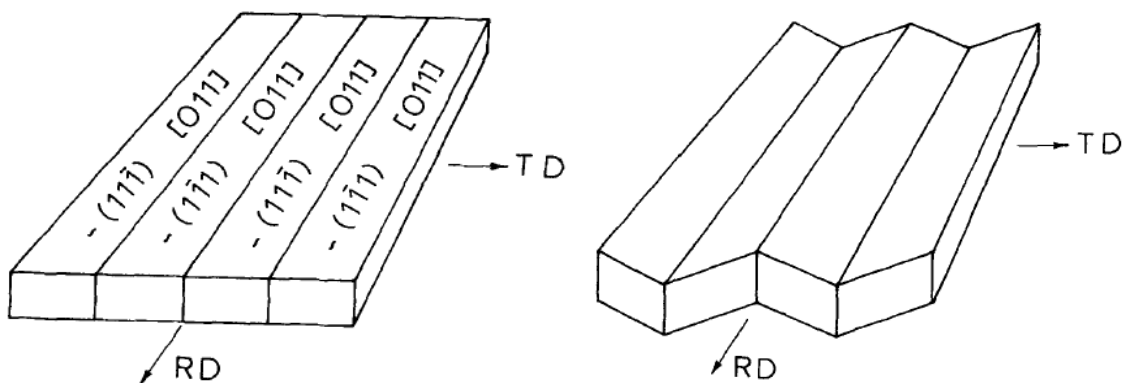


Figure 4-16 : Schematic drawing of Takechi et al's model [12]

This explanation was further supported by showing etch pits that are groups of grains in the centre of a cold rolled sheets of 17% Cr and several ridges in the cold rolled sheets correspond with changes in the direction of the etch pits consisted with the mechanism. This model requires strong texture components of either {111}<110> or {211}<110>. Wright [67] doubt the generality of the ridging model of Takechi *et al* [12] because roping is commonly observed in annealed cold rolled sheets and there is absence of dominant texture components of the {111}<110> or {211}<011>.

#### 4.6.3. Wright's model

According to Wright model, there is a compatibility problem occurring during the deformation due to different plastic strain ratio between the {111}<112> and {011}<110> bands [67]. The {111}<112> gives rise to higher  $R_m$ -values compared to {100}<100>. It was furthermore found that this compatibility problems can be satisfied provided that {001}<110> band buckled along normal direction as shown in the Figure 4-17 below.

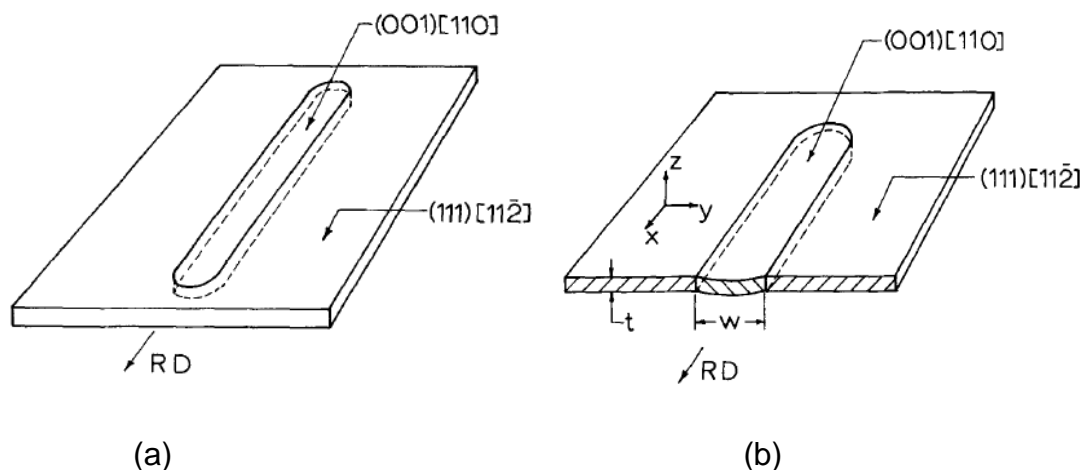


Figure 4-17: Schematic representation of plastic buckling mechanism for roping [67]. (b) Before rolling direction elongation and (a) after rolling direction elongation.

It was further found in this model that  $\{001\}\langle 110\rangle$  and  $\{110\}\langle 112\rangle$  bands contracts mainly in the short transverse direction upon tensile loading in the rolling direction. These banded texture are commonly surrounded by textured materials such as the common annealing cube on corner texture such as  $\{111\}\langle 110\rangle$ ,  $\{111\}\langle 112\rangle$  which shows much less or no contraction in the transverse direction when subjected to tensile elongation in the rolling direction

#### 4.7. Effect of texture on drawability of ferritic stainless steel

Deep drawing is the metal working process used for shaping flat sheets into a cup shaped articles [55]. This is done by placing a blank of appropriate size over a shaped die and pressing the metal into die with a punch as shown in Figure 4-18. For deep drawing, where the blank's hold down force is just high enough to allow smooth radial flow into the die cavity without wrinkling, the major requirements are [22]:

- I. An easy flow in the plane of the sheet under shear conditions, i.e. the materials shall have a low flow stress in both directions in the plane of the sheets;
- II. The side walls of the drawn component shall resist thinning in the thickness direction and this requires a high flow stress in the thickness direction.

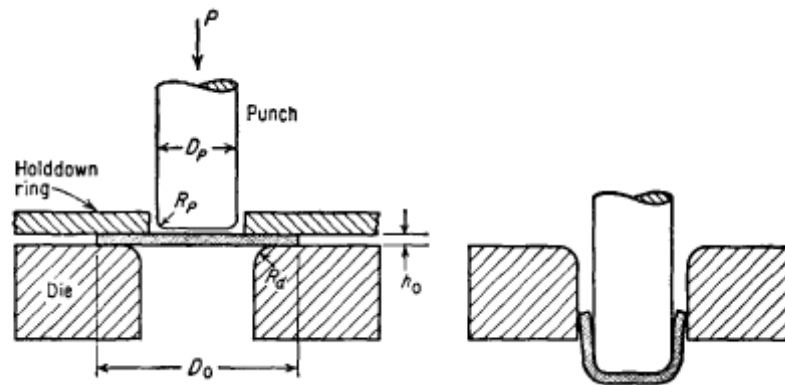


Figure 4-18: Principles involved in deep drawing of a blank sheet into a cup [55].

Generally, the onset of plastic instability during the deep drawing process leads to metals failure. One factor that controls the beginning of the necking is the plastic strain ratio, R-value. R-value is the ratio of the true strain in the width direction to the true strain in the thickness direction during tensile test as shown by Equation 4-5 [23].

$$R = \frac{\varepsilon_w}{\varepsilon_t} \dots\dots 4-5$$

Where  $\varepsilon_w$  and  $\varepsilon_t$  are the true strains in the width and thickness directions of the conventional tensile test of the material respectively. It is difficult to measure the change in thickness of a thin sheet and this can be simplified by using the constance of volume principle. Therefore expression shown by Equation 4-6 can be rewritten as:

$$R = \frac{\ln \frac{w_0}{w}}{\ln \frac{w_0 L_0}{w L}} \dots\dots 4-6$$

The above equation allows the measurement of the changes in width ( $\Delta w$ ) and length ( $\Delta L$ ) during normal uniaxial tensile test of the sheet metal instead of more difficult measurement of the change in thickness,  $\Delta t$ , required for the determination of  $\varepsilon_t$ . The R-value is related to crystallographic texture of sheet steel and varies with the direction of the test relative to the sheet rolling direction in anisotropic materials

[23]. During cold and hot rolling processes, thin sheet materials will possess a certain degree of texture and its stress strain behavior will also be direction dependent. Therefore R-values are measured in three directions of the rolling direction ( $0^\circ$ ), across the rolling direction ( $90^\circ$ ) and at  $45^\circ$  to the rolling direction to take into the effect of direction. The mean value for  $\bar{R}$  (also designated as  $R_m$ ) is given by equation 4-6 and this value represents the average plastic anisotropy of the material.

$$R_m = \frac{r_0 + 2r_{45} + r_{90}}{4} \dots\dots 4-6$$

The variation of R-value in the rolling plane is measured by the change in R-value ( $\Delta R$ ) as given by Equation 4-7.

$$\Delta R = \frac{r_0 + r_{90} - 2r_{45}}{2} \dots\dots 4-7$$

The  $\Delta R$  value represents the planar anisotropy of the materials and is the indication of the amount of necking or earing that will occur on the edges of the deep drawn cups. When  $\Delta R$  is positive, ears tend to form in the rolling direction and at  $90^\circ$  from the rolling direction and when it is negative, the ears form at  $45^\circ$  from the rolling direction.

#### 4.7.1. Texture requirement for deep drawing

Hatherley et al [42] reported that texture in the metal sheet can have two types of influence on deep drawability. It was observed that if the plastic flow properties vary with the angle around the sheet, the flow of metal will be uneven and this will give rise to peaks and troughs (earing) around the periphery of the deep drawn cup. This phenomenon is often referred to as planar anisotropy and it is undesirable as further trimming operations have to be carried out to remove the ears. To obtain extensive deformation in a drawing operation, it is necessary that the flow of the metals in the flange region occur easily without the buildup of high stresses which lead to fracture in the vicinity of the punch. Therefore, suitable texture can introduce a differential

strengthening between in-plane and the through thickness mode of plastic deformation.

Deep drawability of the steel is associated with the high values of  $R_m$  and with  $\Delta R$  close to zero. High  $R_m$ -values are obtained after annealing after relatively high cold reductions of between 60 to 75% as shown in the Figure 4-19. The high  $R_m$ -values are associated with the  $\{111\} \langle 110 \rangle$  fibre in the annealed sheet and if the cold work reduction exceed 75%, the  $\{111\} \langle 112 \rangle$  component emerges [17].

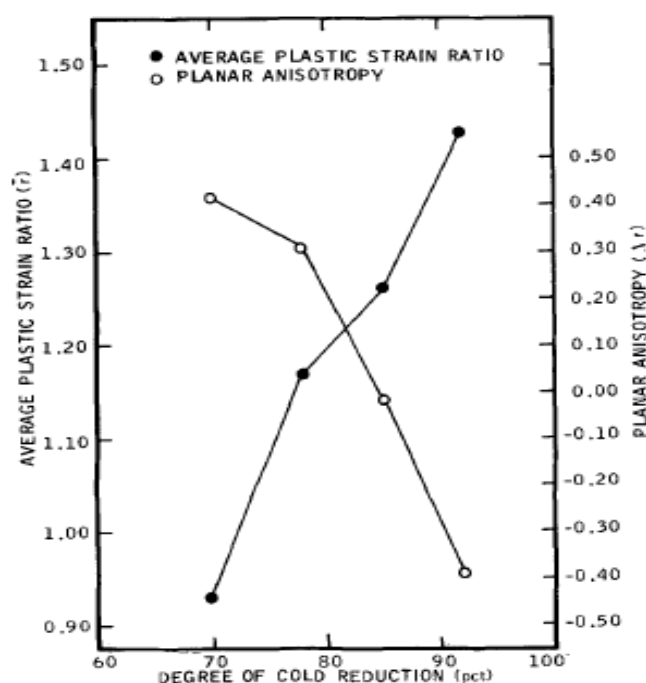


Figure 4-19: Effect of the amount of cold reduction on the  $R_m$ -value and  $\Delta R$  of 18%Cr-2%Mo ferritic stainless steel [17].

It is evident from Table 4-2 that formation of  $\{100\} \langle 011 \rangle$  must be avoided due to its negative effect on the deep drawability, earing and lead to delamination behavior of steels [43]. This can be minimised by avoiding  $\gamma$ -recrystallisation because during recrystallisation  $\{100\} \langle 001 \rangle$  forms which eventually transform into the  $\{100\} \langle 011 \rangle$ .

Table 4-2: Major transformation texture components and their related orientations [68].

Texture components	Source	$\Delta r$	$R_m$
{100}<011>	T	-0.8	0.4
{113}<110>	T	-1.7	1.0
{332}<113>	T	1.9	2.7
{112}<110> (Copper)	R	-2.7	2.1
{223}<113>	R	-2.0	2.5
{554}<225>	R,A	1.1	2.6
{111}<112>	R,A	0.0	2.6
{111}<123>	R,A	0.1	2.4
{111}<110>	R,A	0.0	2.6

Good drawability and minimum earing can be attained by maximizing {554}<225>, {111}<112>, {111}<123> and {110}<110> texture components. It was reported that the sharpness of {111}<112> can be increased by alloying the steel with Nb, Ti and V, decrease the finishing temperature and increase rolling reductions [51]. Effect of finishing temperature on desirable texture is shown in Figure 4-20. From Figure 4-20, it can be seen that finishing rolling at lower temperature enhanced the formation of {111}<110> and {111}<112> textures.

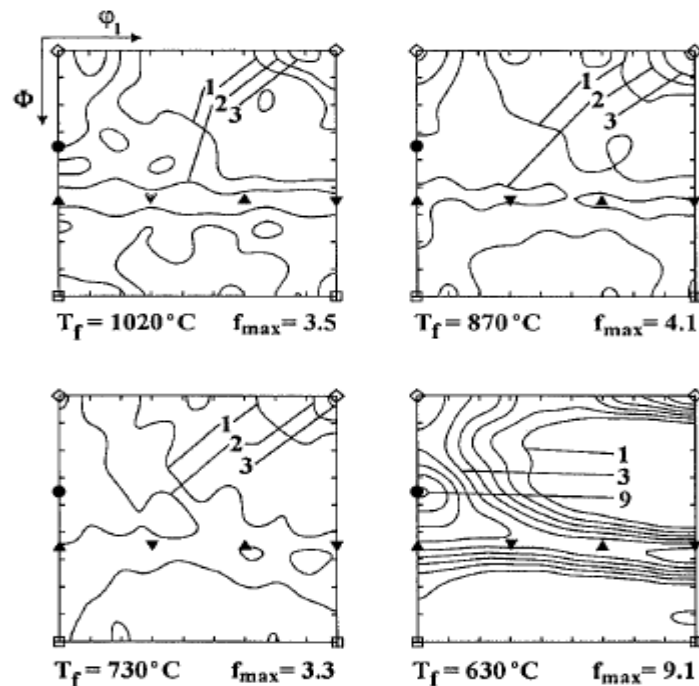


Figure 4-20: The  $\phi_2 = 45^\circ$  sections (Bunge notation) of the experimental ODFs of plain carbon steel, rolled at different finishing temperatures [43]



Lewis and Pickering [16] studied the development of recrystallisation texture in ferritic stainless steel and their relationship to formability and it was also found that there is a relationship between limiting drawing ratio (LDR), the R-value and texture parameter involving the ratio of  $\{111\}:\{100\}$  component in the texture. Both the R-value and the LDR increases as the intensity of  $\{111\}$  structural component parallel to the rolling plane increases, indicating the beneficial effect of a strong  $\{111\}$  component in deep drawing. Therefore, it is desirable to minimise the  $\{110\}$  texture and maximise  $\{111\}$  texture to obtain high  $R_m$ -values as depicted in Figure 4-21.

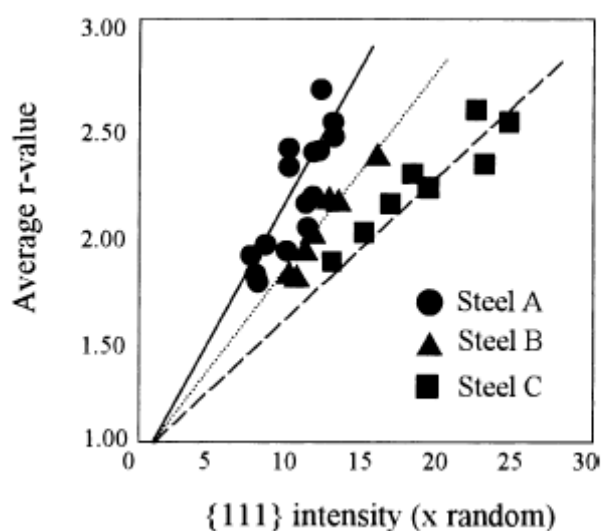


Figure 4-21: Relationship between the  $\{111\}$  intensity and the average strain ratio  $R_m$ -value [69].

#### 4.8. Effect of alloying elements on texture formation

It has been shown by Hu and Goodman [70] that manganese is detrimental to  $R_m$ -value in cold rolled and annealed sheets of low carbon steel.  $R_m$ -value was found to be approximately 1 when more than 0.4%Mn is present but increases sharply at low manganese content reaching  $R_m$ -value of 2.5 at 0.02%Mn. This is due to the  $\{111\}$  texture component that is developed strongly during recrystallisation and grain growth when manganese level is relatively low. When Manganese content increases, the recovery and recrystallisation kinetics are lowered and this reduces the  $\{111\}$  texture.

As may be seen from Figure 4-22, high levels of carbon and nitrogen are also undesirable to deep drawability of steels. It is reported that if the amount of interstitial

carbon and nitrogen are low, there is a quick restoration in the deformed grains and different nucleation sites are activated and lead to a {111} grain structure. Interstitial carbon and nitrogen in solid solution favours the formation of grain with lower strain energy at the expense of highly deformed grains and carbon also slows down the restoration process because of the C-Mn dipoles immobilising dislocations [71]. Therefore, additions of Ti and Nb to ferritic stainless have beneficial effect on the drawability as they bind the interstitials and promote the formation of a strong {111} texture. This leads to an increase  $R_m$ -value as shown in Figure 4-22(b).

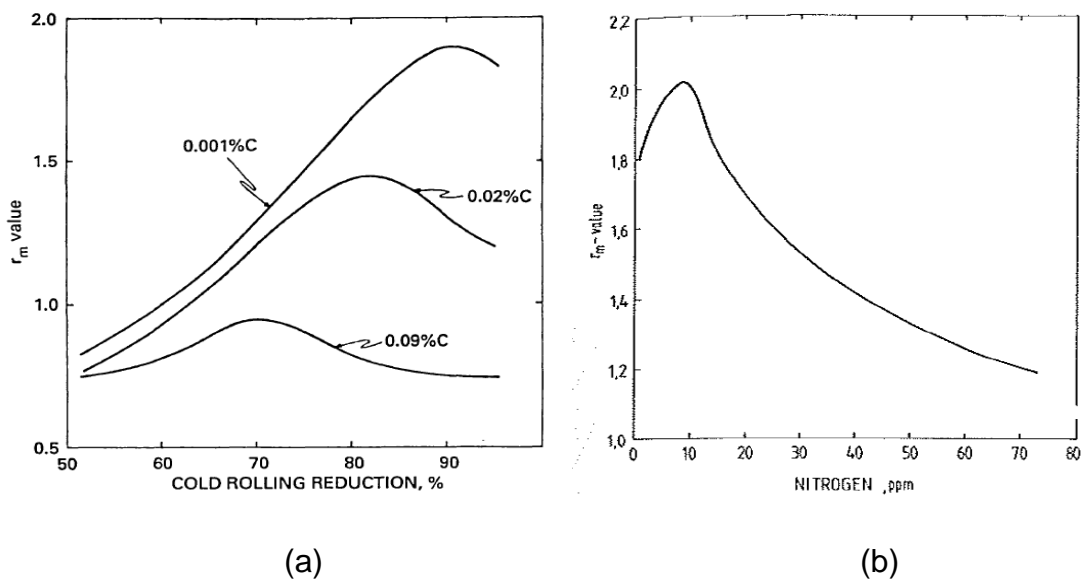


Figure 4-22: Effect of Carbon [72] and Nitrogen [73] on the  $R_m$ -value on low carbon steel

## 5. CHAPTER 5: EXPERIMENTAL DETAILS

### 5.1. Description of the material

#### 5.1.1. Chemical composition

The main emphasis in the study of this steel was to understand the effect of (Nb+Ti) content on the formability and ridging of this steel and also to study the effect of the percentage cold reduction and annealing temperature on texture development in type AISI 441 ferritic stainless steel. Hot band, annealed hot band, cold rolled and annealed cold rolled specimens designated type B were received from Columbus Stainless. The effect of the alloys chemical composition (Nb+Ti) content was investigated through two experimental alloys whose chemical compositions were within the Type AISI 441 ferritic stainless steel specification. Alloy A had lower Nb content and slightly higher Ti content than alloy B whereas alloy C contained both more Nb and Ti than Alloy B.

The following criteria were used in designing of the experimental alloys:

- I. Lower the Nb content and increase the Ti content
- II. Increase both the Nb and Ti content

The summary of the chemical compositions for all the three steels are given in Table 5-1 below.

Table 5-1: Chemical composition (wt. %) of the industrial steel designated B and experimental alloys A and C.

	%C	%Mn	%Si	%Cr	%N	Ni	%S	%P	%Nb	%Ti	Remarks
A	0.015	0.4	0.35	16.8	0.04	0.1	0.002	0.04	0.26	0.2	Nb $\geq$ 0.3+(3×C)
B	0.012	0.4	0.51	17.68	0.04	0.12	0.0005	0.02	0.444	0.151	
C	0.015	0.42	0.41	17.28	0.01	0.12	0.001	0.02	0.7	0.3	

The lower limit of the Ti content is based on the minimum amount needed to fully stabilise the steel. The upper limit of the Ti content was based on the fact that

excessive addition above the required requirement for full stabilisation would cause an increase in DBTT and a decrease in ductility [36]. It has been reported in literature that excess Ti content in steel can have negative effect on the surface finish of the steel sheet [74] and can also lead to excessive inclusions. The Nb content in the steel must be kept as low as possible due to its cost.

## **5.2. Production of experimental alloys**

Steel B was industrially produced and supplied by Columbus as a 1.5 mm cold rolled and annealed strip. The experimental alloys A and C were prepared in the lab by Specialised Alloys and Metallurgical Services (SAMS) in a 50kg vacuum induction melting furnace (VIM) using transfers bars from steel A as a base metal.

### **5.2.1. Hot rolling, annealing and cold rolling of the experimental alloys**

The as cast alloys were homogenised in an argon atmosphere at 1200°C and then hot forged into square bars of 25-30mm thick. These ingots were thereafter reheated to 1200°C and hot rolled in several passes into a final thickness gauge of 4.5mm and quenched into water. The last pass finishing temperature before water quenching was found to be 920°C. After hot rolling, the samples were annealed for 300s at 1025°C and followed by water quenching. The annealed 4.5 mm strips were further cold rolled 62% into sheets of thickness of 1.5mm. These cold rolled samples were finally annealed at 1025°C for 300s.

### **5.2.2. Cold rolling of as-received hot band**

The thickness of the as-received hot band materials was 4.5mm. Therefore, to study the effect of amount of cold reduction on texture evolution, the 4.5mm hot band was cold rolled down to 1.5mm, 1mm and 0.8mm. These reductions corresponded to 62%, 78% and 82% cold reduction with the 62% simulating industrial cold reduction.

## **5.3. Microstructural analysis**

### **5.3.1. Optical microscopy and Scanning electron microscopy**

The metallographic specimens were prepared by following the standard metallographic techniques. The specimens were then polished down to a 1µm finish and then etched in 100ml H<sub>2</sub>O, 100ml HCl and 100ml HNO<sub>3</sub>. The microstructural analysis was carried out using Olympus PGM optical microscope equipped with

Image Analysis software. Microstructural analysis was carried out by both optical and scanning electron microscopy (SEM-EDS) on longitudinal sections perpendicular to rolled surface, i.e. RD-ND plane. The scanning electron microscope investigations were carried out on a high resolution scanning electron microscope equipped with EDX (HRSEM-EDX) model using EDAX Genesis detector.

Microstructural analysis was conducted to evaluate and assess the influence of cold reduction, annealing temperature, composition on the evolution of microstructure.

### **5.3.2. Measurement of grain size**

The grain size was determined by using the linear intercept method according to the ASTM E112-96<sup>1</sup> standard. The average five grain size measurements were conducted.

### **5.3.3. Scanning electron microscope**

The scanning electron microscope investigations were carried out on a high resolution scanning electron microscope equipped with EDX (HRSEM-EDX) model Joel JSM-6000F SEM as indicated in Figure 5-1. EBSD analysis investigation was carried out using Jeol JSM -6300 SEM equipped with EBSD. The accelerating voltage was set at 15KV and the probe current was set at  $7 \times 10^{-9}$  A. The sample was tilted at an angle of  $70^\circ$  to allow more electron diffraction to the detector [47]. The EBSD scans were performed in a FEI NOVA NanoSEM 230 FEG equipped with EDAX Digiview EBSD Camera operated at 20kV. Grain boundary analyses of the annealed samples were carried out using EBSD at mid thickness of the specimens in RD-TD plane and were evaluated using the EDAX-TSL software package. During data collection, a minimum number of seven Kikuchi bands were allowed to index a pattern, thus ensuring reliable information [47].

---

<sup>1</sup> ASTM E112-96: Standard Test Method for Determining Average Grain Size



Figure 5-1: FEI NOVA NanoSEM 230 FEG used for analysis

Field [75] reported that EBSD patterns having confidence index above 0.1 can correctly index an orientation 95% of the time. Average confidence index of the patterns was above 0.45 in this work and this led to more than 96% of the patterns being indexed correctly in every case. The minimum angular resolution of the EBSD from alpha iron using W filament has been found to be  $1^\circ$  as reported by Humphrey [76]. In order to make accurate measurements, misorientations less than  $1.5^\circ$  were excluded from the data [47]. The step size of 10% of the grain size was used to ensure that at least 1000 grains or more were scanned to give good statistical representation of texture or orientation of the grains as reported by Engler [47]. EBSD data was calculated using the series expansion method with  $I_{\max} = 22$ . Orthotropic sample symmetry was applied and the orientations were expressed in Euler angles such that  $0^\circ \leq (\varphi_1, \theta, \varphi_2) \leq 90^\circ$  with  $10^\circ$  Gaussian spread around the ideal orientations.

The specimens for EBSD were mounted, grinded and then polished down to  $1\mu\text{m}$ . The specimens were further electropolished in an alcohol solution of 5% perchloric acid using an applied voltage of 35V dc for a period of 30 sec. This was done to ensure that good surface finish is obtained for suitable diffraction.

## 5.4. Effect of thermomechanical processing on texture

### 5.4.1. Isothermal annealing of specimens after cold rolling

After cold working, samples were annealed at 900, 950 and 1050°C for 180s. The choice of annealing temperature was based on three factors namely: the need to obtain sufficient recrystallisation, avoiding precipitation of laves phase and grain growth. The insufficient recrystallisation allows the banded structure to remain in the steel thus lowering  $R_m$  value and results in significant ridging.

## 5.5. Texture measurement

Pole figures were measured by PANanalytical X'Pert PRO diffractometer with X'celerator detector and variable divergence using Cu-K $\alpha$  radiation on the central of the sheets with 5° steps. Specimens obtained from the center of the samples were sequentially prepared by combination of careful grinding, polishing and chemically etched with dilute hydrochloric acid to remove surface deformation caused by the grinding and the mechanical polishing. The Three dimensional crystallographic orientation distribution functions (ODFs) was obtained from the three incomplete pole figures ( $\{110\}$ ,  $\{200\}$  and  $\{211\}$ ) measured in back reflection with a maximum tilt of 75°. The rolling direction was used as a reference direction for texture measurement.

The ODFs,  $f(g)$ , were calculated by the series expansion method according to Bunge ( $l_{\max} = 22$ ). Three Euler angles ( $\varphi_1$ ,  $\Phi$ ,  $\varphi_2$ ) were used to express orientation  $g$  and orthotropic sample symmetry was applied.

## 5.6. Mechanical testing

### 5.6.1. Tensile tests

Formability of the material can be estimated by the Lankford parameter (R-value) which is defined as the ratio of the true stain in the width direction to the true strain in the thickness direction. Tensile tests were employed to determine  $R_m$ -values and  $\Delta R$  values of the sheets and to determine mechanical properties. These values were used to evaluate effect of annealing temperature and Nb/Ti ratio on formability and mechanical properties of the alloys. Two samples were used per condition to determine the mechanical properties and  $R_m$ -values.



Tensile tests were carried out at a cross head speed of 5mm/min at room temperature using Instron tensile tester Model no 1175 as shown in Figure 5-2 below. Sub-sized tensile specimens were produced according to the ASTM E-517<sup>2</sup>. The schematic drawing of the tensile specimen and dimensions are shown in Figure 5-3 and Table 5-2 respectively.  $R_m$  and  $\Delta R$  values were measured after 10% tensile strain along the longitudinal, transverse and diagonal directions as indicated in Figure 5-4.



Figure 5-2: Instron tensile testing machine used to determine  $R_m$ -values and mechanical properties.

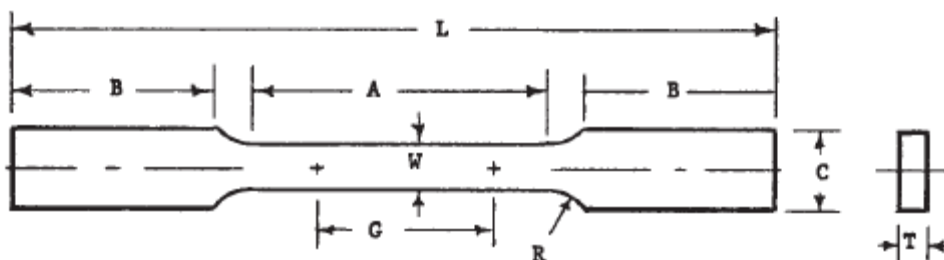


Figure 5-3: Specimen dimension for plastic strain ratio determination.

<sup>2</sup> ASTM E 517: Standard Test Method for Plastic Strain Ration (R) for Sheet Metal.



Table 5-2: Dimensions for the tensile test specimen

	Parameters	Dimensions
<b>G</b>	Gauge Length	50mm
<b>W</b>	Width	12.5mm
<b>T</b>	Thickness	Thickness of material
<b>R</b>	Radius of fillet	13mm
<b>L</b>	Overall Length	300mm
<b>A</b>	Length of a Reduced Section	60mm
<b>B</b>	Length of a Grip Section	50mm
<b>C</b>	Width of Grip Section	30mm

It is important that the sheet thickness is constants because the results of the formability test depend on the thickness of the test sheet [16]. Due to sample limitations, the reported  $R_m$ -values are average of two measurements.

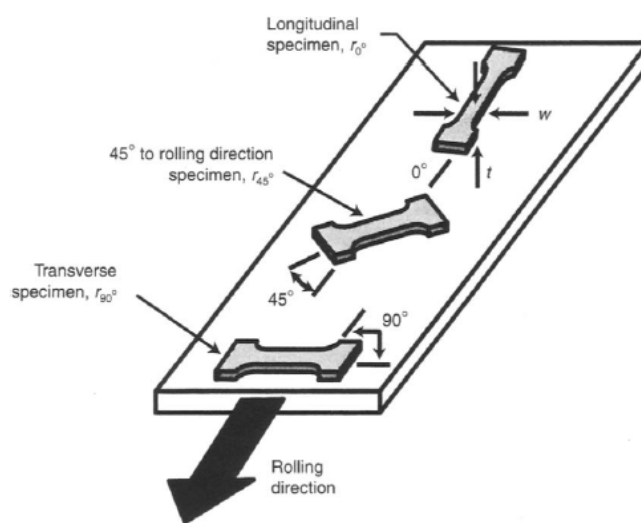


Figure 5-4: Specimen orientation for determining plastic anisotropy of metal [77].

Surface ridging characteristics behaviour was investigated for samples in the cold rolled and annealed condition. The ridging profile was determined after 10% tensile elongation on a tensile specimen. Specimens were grinded and polished before tensile straining and the surface topography was mapped after tensile deformation using stylus profilometer. Figure 5-5 below shows where the surface roughnesses were taken.

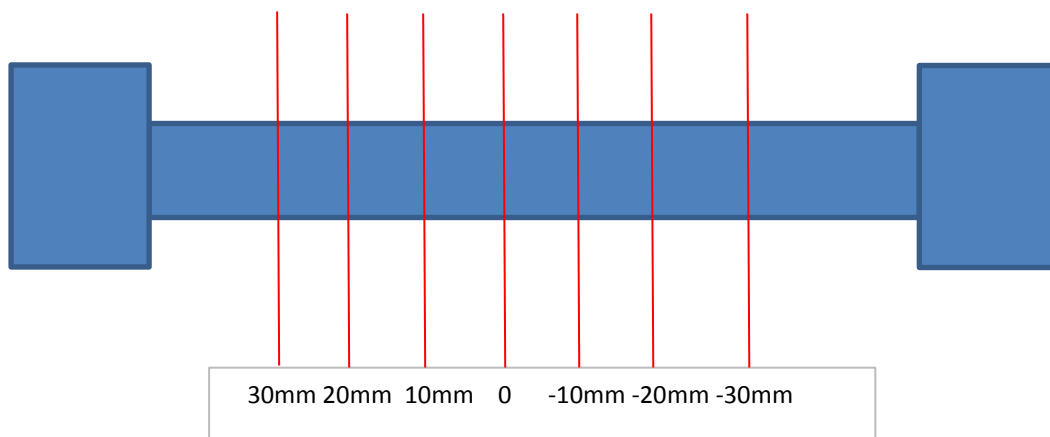


Figure 5-5: Schematic diagram of tensile specimen showing how surface roughness was measured

### 5.6.2. Hardness measurement

Vickers hardness measurements were made using a load of 20kgf to give large indentation for accurate measurement. Two samples were used per condition to determine the hardness values. Averages of at least ten readings were taken for each result. The specimen were ground and polished before hardness measurement could be measured. This was done to ensure that flat and smooth surface is obtained for accurate measurement.



## 6. CHAPTER 6: RESULTS

### 6.1. Introduction

Results from this study are divided into four sections:

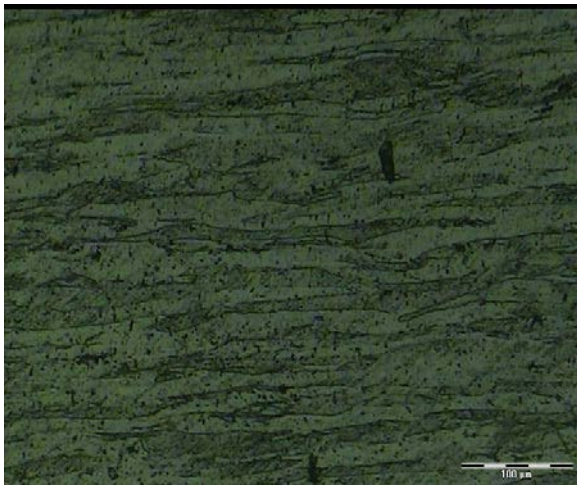
- The first section deals with the effect of cold rolling and annealing process on microstructural and texture evolution in AISI 441 ferritic stainless steel;
- The second section deals with the effect of cold rolling and annealing process on formability of AISI 441 ferritic stainless steel;
- The third section deals with the effect of (Nb+Ti) content on microstructural and texture evolution of AISI 441 ferritic stainless steels
- The fourth section deals with the effect of (Nb+Ti) content on ridging resistance of AISI 441 ferritic stainless steels

### 6.2. Effect of cold reduction and annealing process on microstructural and texture evolution of AISI 441 steel

In order to understand the effect of cold rolling and annealing process on microstructural and texture evolution in AISI 441 ferritic stainless steel, microstructural analyses and bulk texture analysis were carried out. These analyses involve using optical and scanning electron microscopy (SEM) for microstructural analysis and XRD texture measurement for texture analysis. The analyses were carried out on both steels in as-received and laboratory processed conditions. In both cases, they were in cold worked and annealed conditions.

#### 6.2.1. Microstructural analysis of as-received steels

Figure 6-1 shows the optical micrographs for cold rolled steels after 62%, 78% and 82% cold reduction. After cold rolling, the microstructure composed of elongated ribbon like grains with a large number of interior shear deformation. As may be seen from Figure 6-1 below, the grains are deformed along the rolling direction and the spacing between deformations bands tend to decrease with an increase in strain.



(a)



(b)



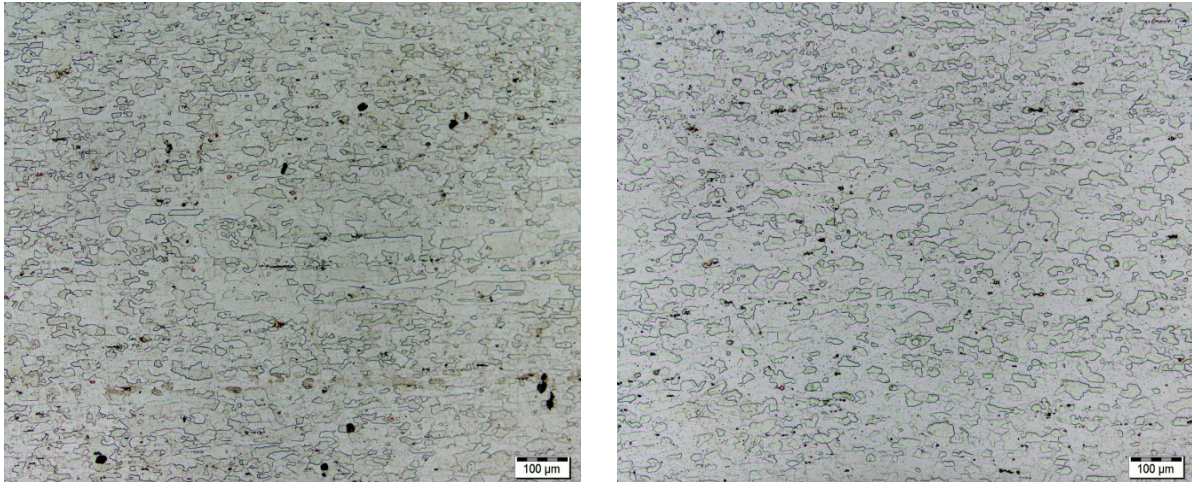
(c)

Figure 6-1: Effect of cold working on the microstructure of AISI 441 ferritic stainless steels. a) 62% cold worked b) 78% cold worked c) 82% cold worked

All three cold rolled materials show similar wavy slip lines and some of these are strongly etched while others are lightly etched. It was reported by Jun-ichi et al [78] that this behaviour depends on their location on the microstructure. As may be seen from Figure 6-1, by increasing the amount of deformation, the deformation bands become narrower. Increasing the amount of cold reduction increases the non-uniform deformation regions (such as shear bands indicated by arrows) which act as nucleation sites for the {111} texture [45, 69].

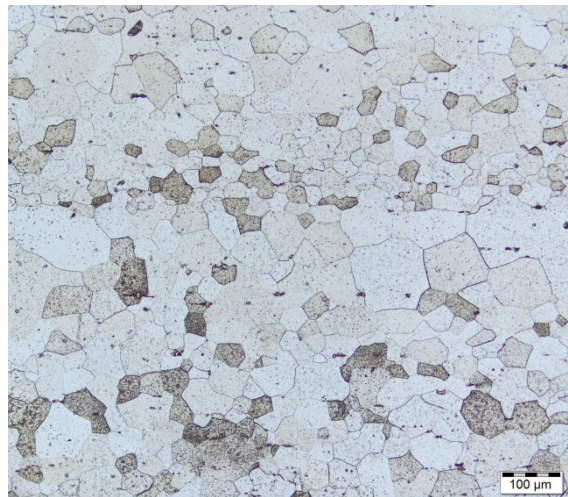


Figure 6-2 to 6-5 below show the effect of annealing temperature on the grain structure evolution of the 78% and 82% cold rolled materials. As may be seen in Figure 6-2 and 6-4, the steel which was given a deformation of 78% and 82% underwent recrystallisation at 900 and 950°C and complete recrystallisation and little grain growth at 1025°C.



(a)

(b)



(c)

Figure 6-2: Optical micrograph of the 78% cold rolled specimen after annealing for 300s at (a) 900°C, (b) 950°C and (c) 1025°C cold rolled steel by water quenching

However the extent of recrystallisation is not clear from the optical microscope because visualisation of etched specimens using light microscope provides contrast that originates from localised attack by the etchant. Grain boundary are the reactive sites relative to subgrain boundaries. Therefore SEM-EBSD was undertaken to distinguish between sub-grain boundaries (recovery) and high angle grain boundary as indicated in Figure 6-3 and Figure 6-5.

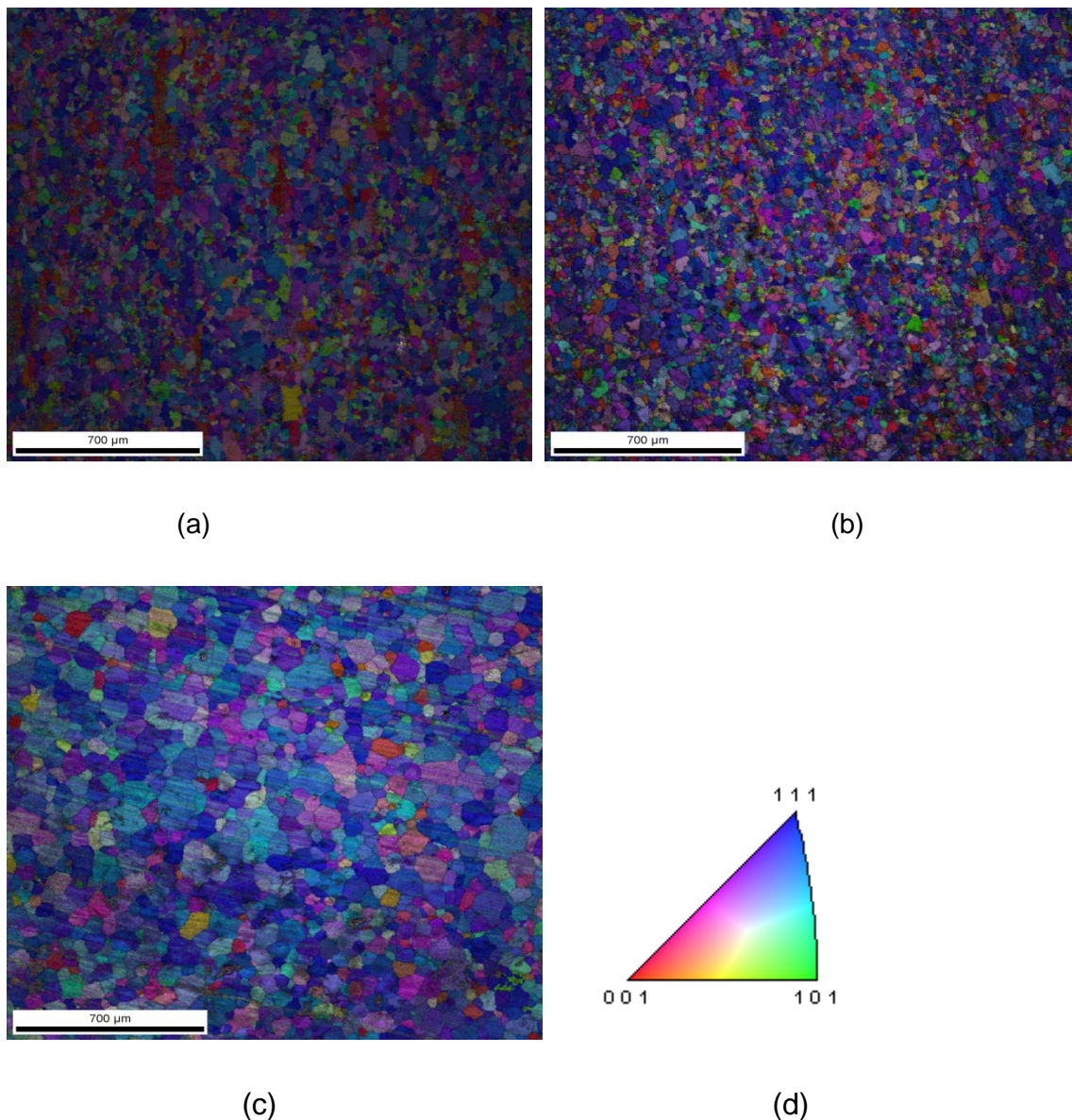
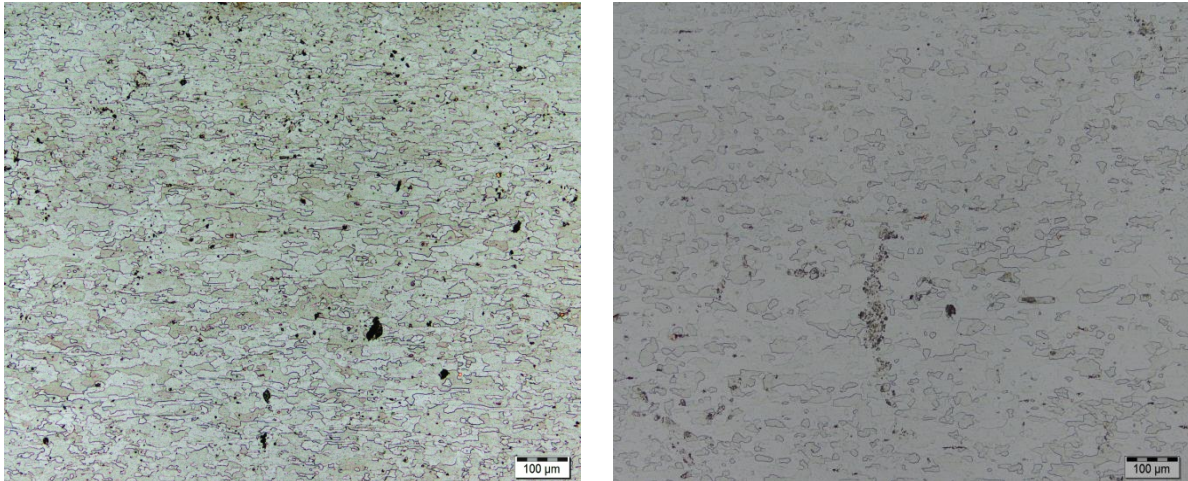


Figure 6-3: Image quality maps of the 78% cold rolled annealed for 300s at (a) 900°C, (b) 950°C and (c) 1025°C cold rolled steel (d) inverse pole figure

Image quality maps indicated in Figure 6-3 and Figure 6-5 clearly shows that recrystallisation took place due to presence of equiaxed grains at 900 and 950°C. In

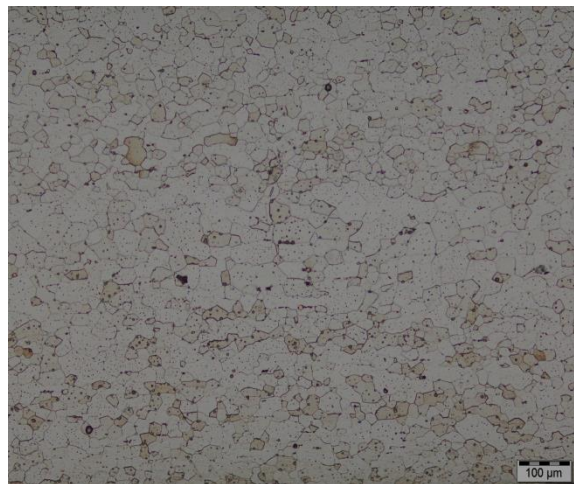


addition there is a change in texture from cold rolled condition with reduction in cube and  $\alpha$ -fibre components or intensities. This is an indication that recrystallisation process has taken place at these annealing temperatures of 900 and 950°C.



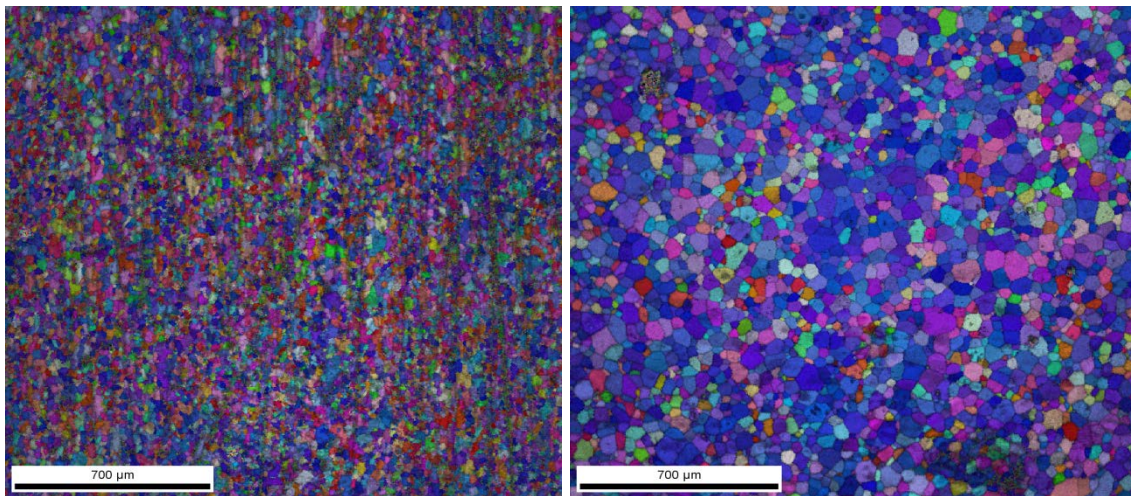
(a)

(b)



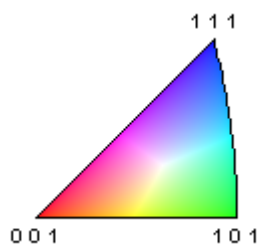
(c)

Figure 6-4: Optical micrograph of the 82% cold rolled specimen after annealing for 300s at (a) 900°C, (b) 950°C and (c) 1025°C cold rolled steel by water quenching



(a)

(b)



(c)

Figure 6-5: Image quality maps of the 82% cold rolled steel annealed for 300s at (a) 900°C, (b) 1025°C cold rolled steel and (c) inverse pole figure

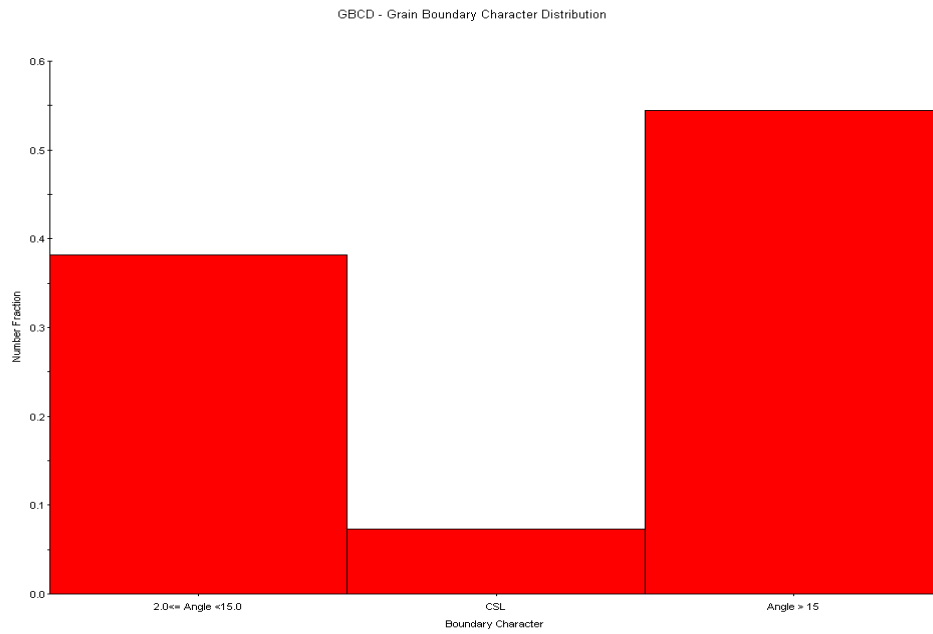
Furthermore, to prove that indeed recrystallisation had taken place at 900 and 950°C, grain boundary character distribution (GBCD) was plotted. The GBCD plots for the steel sheets subjected to 78% cold reduction and annealed at different temperatures are shown in Figure 6-6a-c. There is an increase in the fraction high-angle grain boundaries (HAGB) as the temperature increases from 900 to 1025°C. As may be seen from Figure 6-6a to c recrystallisation had taken place at 900 and 950°C.

The grain boundary character distribution (GBCD) plots for the steel sheets subjected to 82% cold reduction and annealed at different temperatures are shown in Figure 6-7a-c. There is a small decrease in the fraction low-angle boundaries

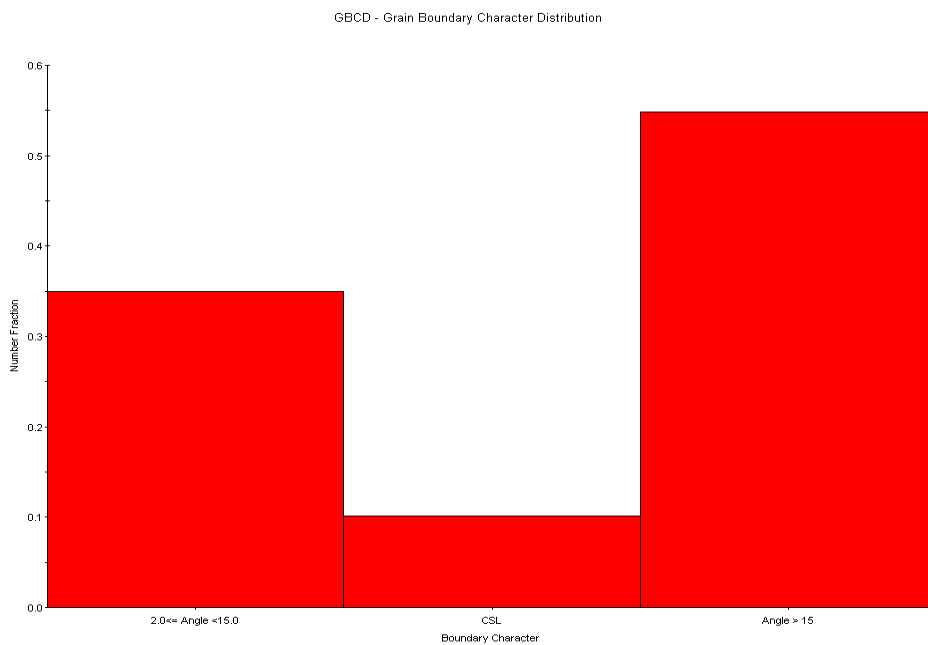




(LAGB) and small increase in the coincident site lattice (CSL) and high-angle grain boundaries (HAGB) as the temperature increases from 900 to 1025°C.



a



b



GBCD - Grain Boundary Character Distribution

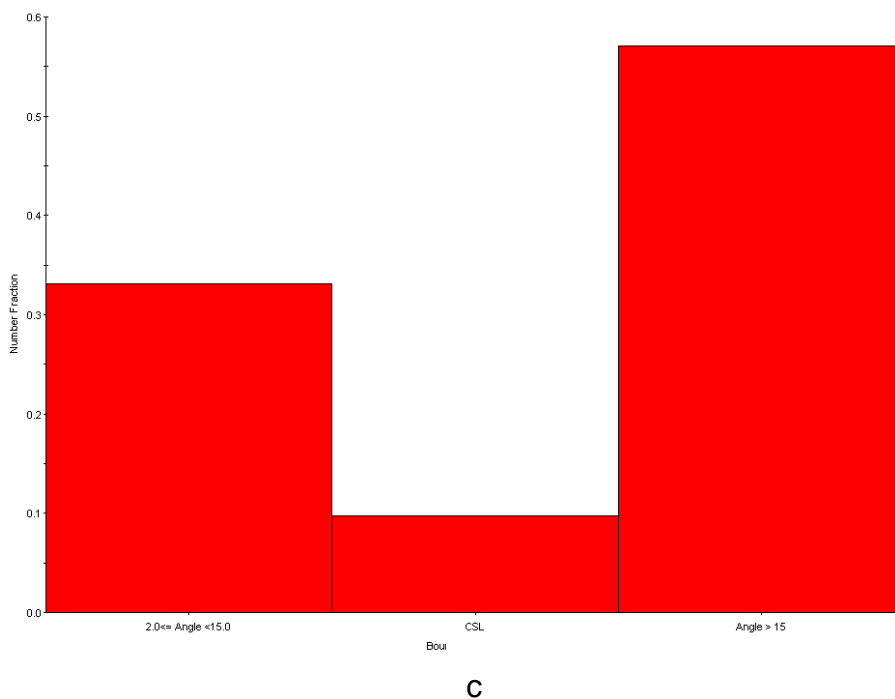
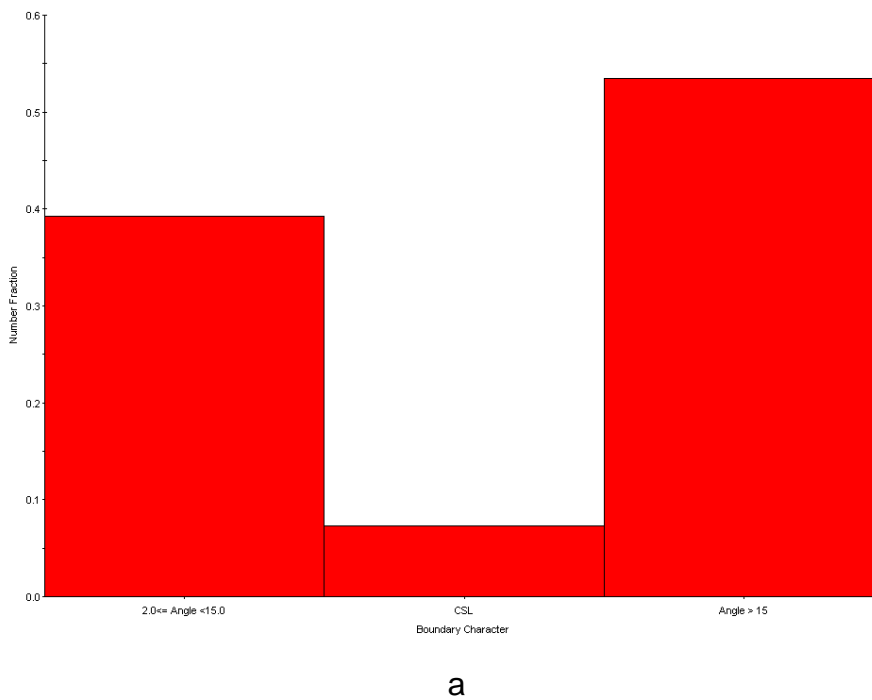


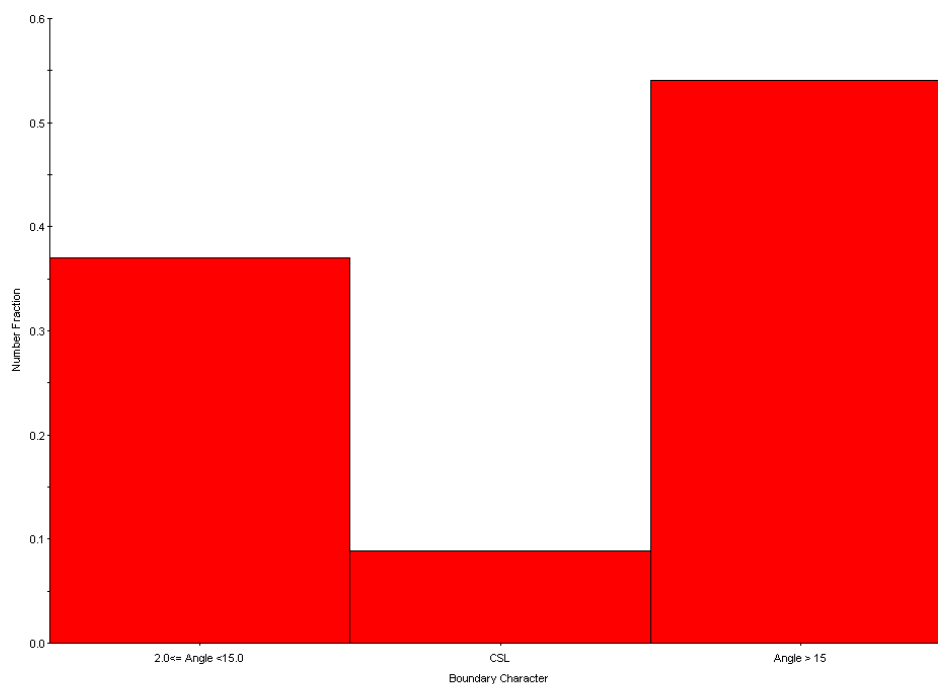
Figure 6-6: Grain boundary character distribution plots of 78% cold rolled steel and annealed at (a) 900°C, (b) 950°C and (c) 1025°C cold rolled steel

GBCD - Grain Boundary Character Distribution





GBCD - Grain Boundary Character Distribution

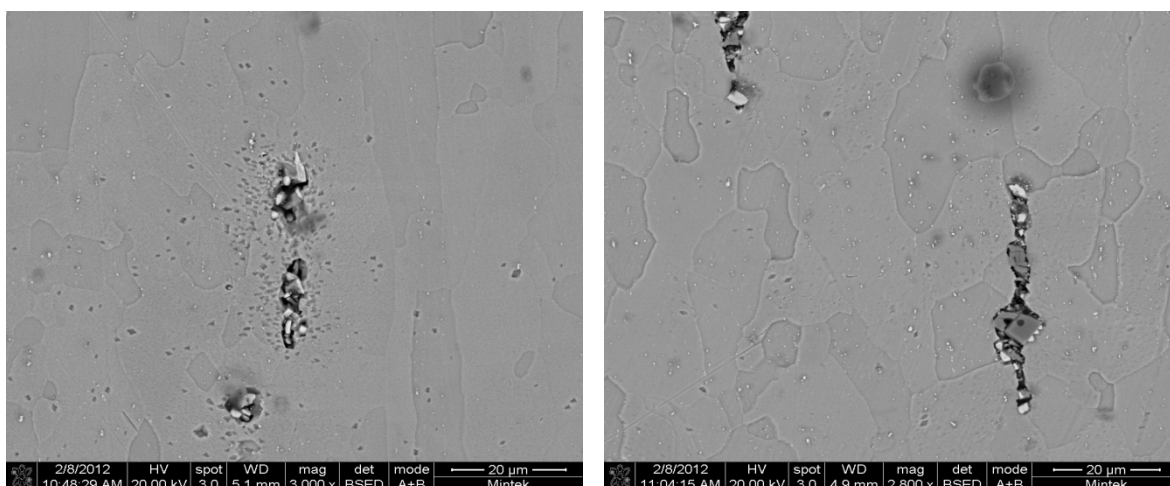


b

Figure 6-7: Grain boundary character distribution plots of 82% cold rolled steel and annealed at (a) 900°C, (b) 1025°C cold rolled steel

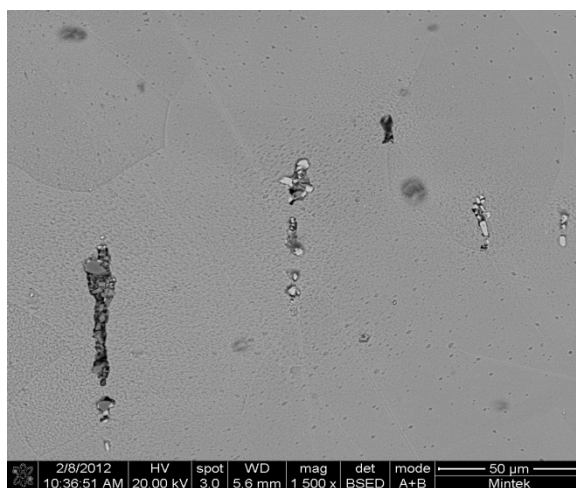
By analysing the GBCD results shown in Figure 6-6 and Figure 6-7, the results shows that increase in annealing temperature increases fraction of HAGB. The higher HAGB fraction indicates that recrystallised grains have formed. It has been reported in literature that the accumulation of dislocations [79, 80] and formation of new grains during recrystallisation [81, 82] are responsible for the increase in HAGB. For the same annealing temperature of 1025°C, 82% cold rolled specimen shows higher CSL fraction compared to 78% cold rolled specimen. This is attributed to the refinement of the structure due to severe deformation [83].

The SEM micrographs of the 78% cold rolled and annealed at three different temperatures are given in Figure 6-8 below. The SEM micrograph shows particles appearing at the grain boundary which had coalesced to form stringers (i.e. as rolled defects). The stringers were elongated and fractured along the grain boundaries in the rolling direction.



(a)

(b)



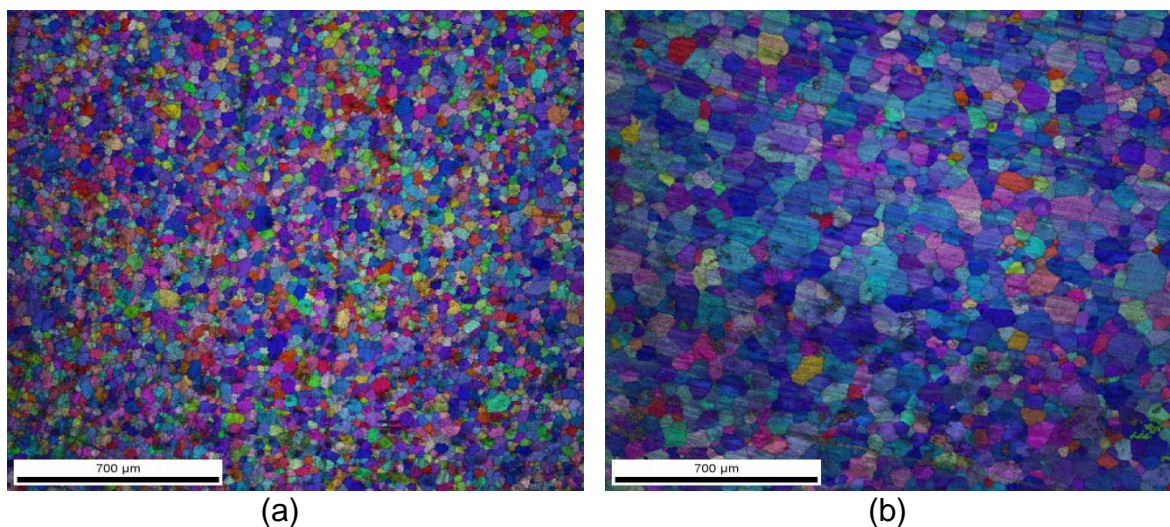
(c)

Figure 6-8: SEM micrographs after 78% cold rolling and annealing at a) 900°C, b) 950°C and c) 1025°C for 300s

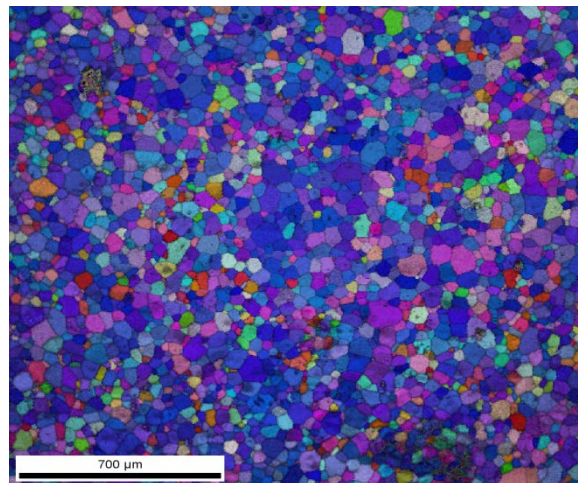
These stringers arise when particles that exist in a microstructure consequently influence grain boundary migration and hence observed to accumulate at the grain boundaries. These grain boundary defects have a negative effect on toughness and formability of this material. It is also noteworthy to see from Figure 6-8 a) and c) that the volume fraction of precipitates seems to decrease as the annealing temperature increases. With annealing above 1025°C, there is a complete dissolution of carbides and microstructure is fully recrystallised. According to SEM-EDX analysis, the whitish phase of the precipitate was found to be niobium carbide (NbC) and

greyish titanium carbonitrides (Ti(C,N) see Figure 6-13. It is the titanium carbonitrides that have a negative influence on formability and toughness of these steels. These forms first during cooling from the melt at the grain boundary and act as nucleation site for NbC. The NbC particles also precipitate within the matrix and, therefore, increase the recrystallisation temperature of these steels as they pin the grain boundaries [84].

It has been reported by Abreu et al [15] that EBSD can be regarded as a reference method for measuring grain size as is not only enabling each grain to be examined but enables this to be accomplished according to misorientation between the two grains. It is for this reason that EBSD was used to analyse grain size variation. Figure 6-9 compares the grain sizes for the steels cold rolled 62%, 78% and 82% respectively and annealed at 1025°C for 180 sec. The 62% cold worked steel was industrially produced. The measured average grain sizes for the steels cold rolled 62%, 78% and 82% were  $30\pm 3\mu\text{m}$ ,  $52\pm 4\mu\text{m}$  and  $41\pm 4\mu\text{m}$  respectively. Contrary to expectation, the steel that was given the least cold reduction of 62% industrially resulted in the finest grain size. This suggests that the industrial cold reduction was somewhat not comparable to that of the laboratory. However, comparison of the two steels which were cold rolled using the lab mill show that increasing the cold reduction from 78 to 82% led to further refinement of the grains due to higher driving force for SRX.







(c)

Figure 6-9: Micrographs for steels cold rolled and all annealed at 1025°C for 180s: (a) 62% industrially produced (b) 78% cold rolled in the lab and (c) 82% cold rolled in the lab

### 6.2.2. Identification of carbides

The yellowish rectangular blocks which are seen in Figure 6-10 below were identified using SEM-EDX as titanium carbonitrides as indicated in Figure 6-11. It has been indicated in literature by Gordon and van Bennekom that the colour of precipitate changes with the ratio between nitrogen and carbon (N/C) in the steel whereby the yellowish/orange colour indicates that the Ti(C,N) contains 10 at.% TiC as was the case with the particles observed in this work, see Figure 6-10 [36].



Figure 6-10: Optical micrograph of as-received hot band after etching with H<sub>2</sub>O, HCl and HNO<sub>3</sub> for 60 seconds

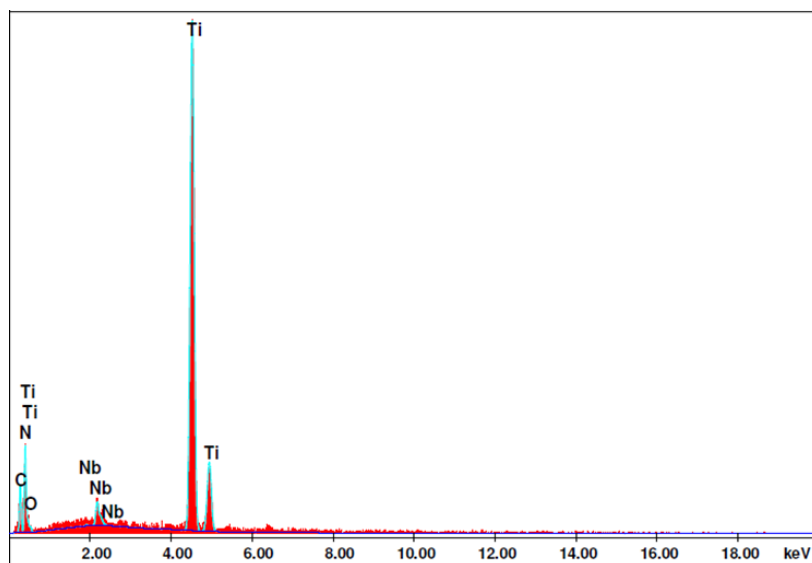


Figure 6-11: SEM-EDS spectra of the yellow particle observed in Figure 6-8

As these ferritic stainless steels are stabilised with Ti and Nb, various kinds of precipitates such as TiC, TiN, Fe<sub>2</sub>Nb and Nb(C,N) are expected to form during different thermomechanical processing [85]. Ti is a highly reactive element which forms TiN precipitates in the presence of N and forms TiC in the presence of C. As Nb is strong carbide former and has higher affinity for carbon than Ti, NbC will form preferentially to TiC. The SEM-EDX results from Figure 6-13 confirm the ThermoCalc® predictions (see Figure 6-12) found by Sello and Stumpf on similar AISI 441 ferritic stainless steel, in that both nitrides and carbides form as (Ti,Nb)(C,N) precipitates with the Ti(C,N) nucleating first and then the Nb(C,N) nucleating on its surface. Figure 6-13 shows the scanning electron micrograph with Energy Dispersive X-Ray Analysis (EDX) analysis of a precipitate formed during annealing of as-received cold rolled specimen. Only large particles could only be analysed using SEM-EDX techniques. As may be seen from Figure 6-13 below, the Nb(C,N) precipitated heterogeneously on the rectangular TiN. This is due to the fact that Ti(C,N) has a lower solubility in ferrite than Nb(C,N) and will therefore form first during cooling from the melt [63]. Nb(C,N) forms at lower temperatures through heterogeneous nucleation on the ledges of existing TiN particle to minimise



activation energy for nucleation. This steel is interstitial-free when annealed at 1025°C as most of the carbon and nitrogen is tied by Ti and Nb.

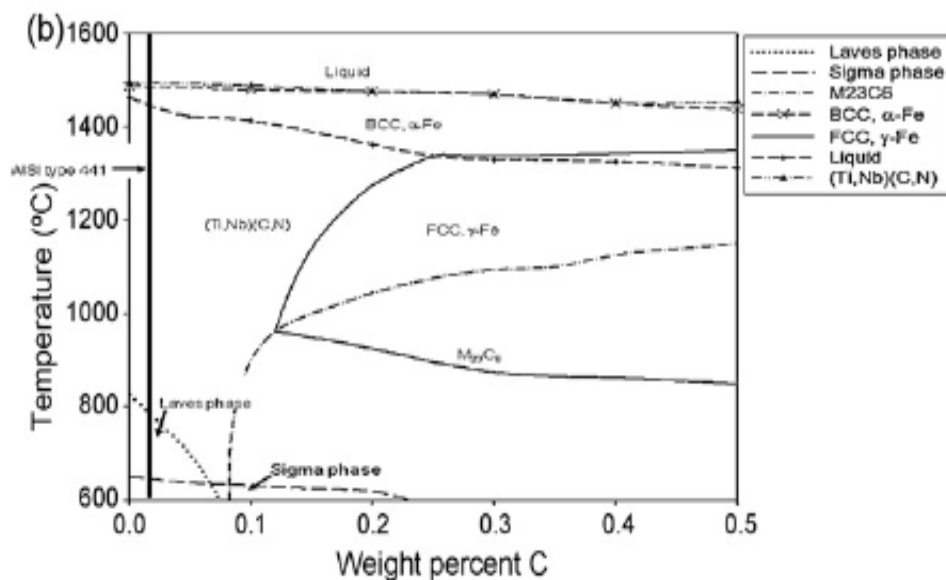


Figure 6-12: The isopleth diagram at 17.9%Cr showing the stable equilibrium phases in type 441 stainless steel with a constant amount of alloying elements and 0–0.5 wt.% of carbon [86].



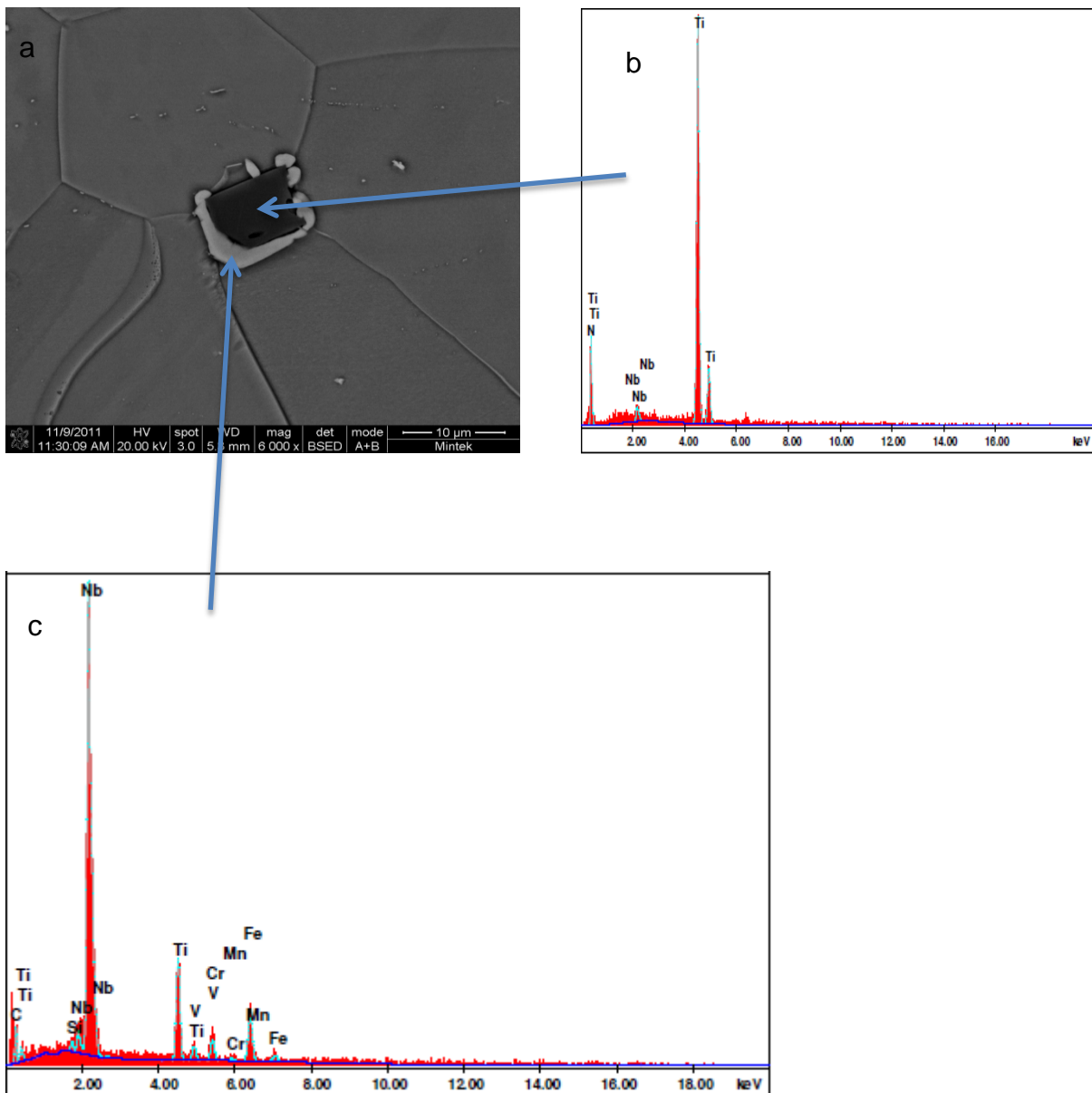


Figure 6-13: a) Scanning electron micrographs of the as-received cold rolled and annealed steel showing precipitation at grain boundaries and inside the matrix, b) and c) are the SEM-EDS spectra of the observed particles.

### 6.2.3. Effect of thermomechanical processing on evolution of texture

#### 6.2.3.1. Cold rolling texture

Figure 6-14 shows the Bunge ODFs section at  $\phi_2 = 45^\circ$  for steels that received the 62%, 78% and 82% cold reduction respectively.

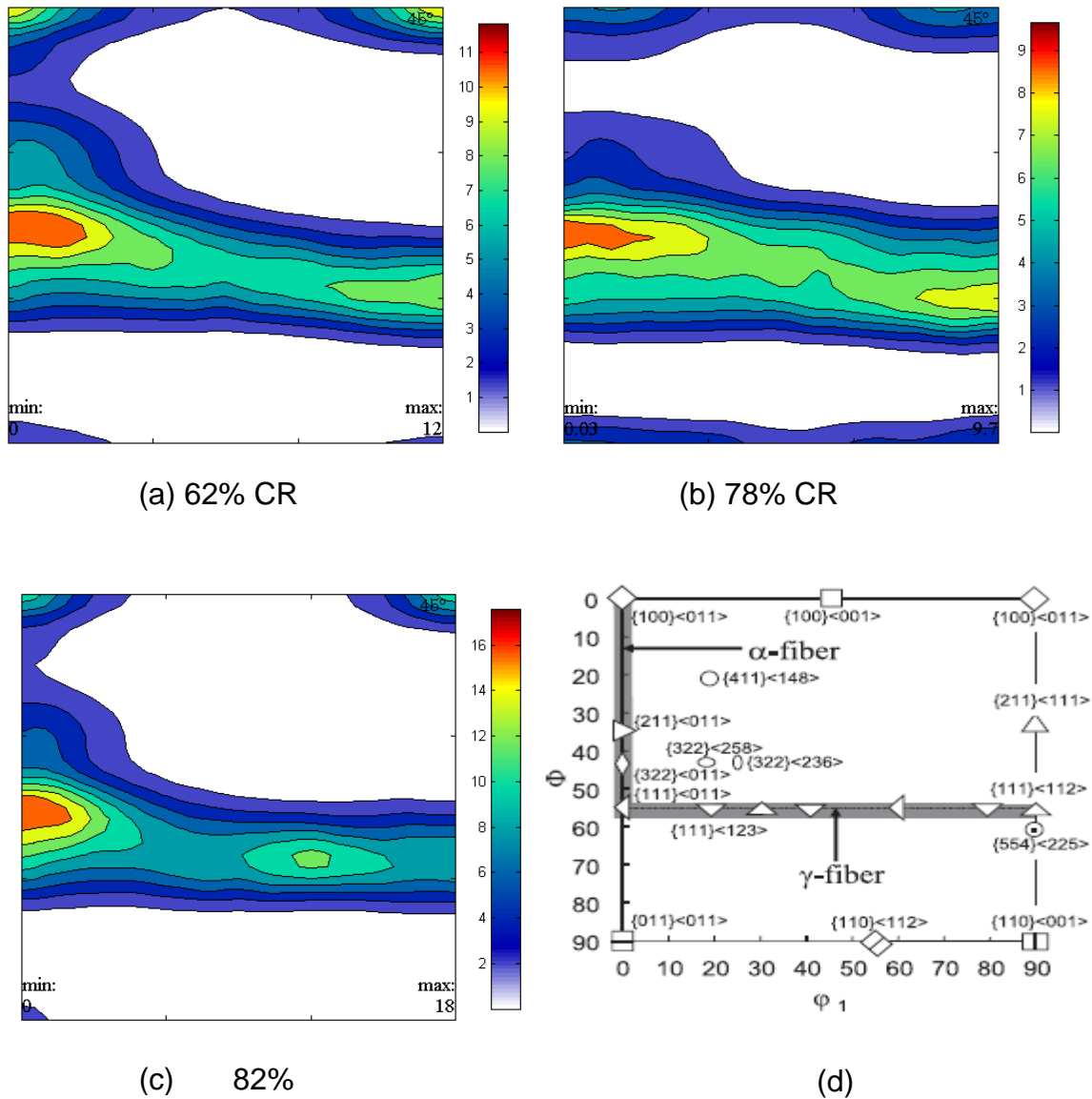


Figure 6-14: XRD Bunge ODFs  $\phi_2 = 45^\circ$  section for steels cold rolled a) 62% as-received, b) and c) cold rolled in the lab for 78% and 82% respectively, and d)  $\phi_2 = 45^\circ$  section showing the position of the main orientations in BCC steels along the RD, ND and TD directions [78].

The texture of cold rolled steels are characterised by both strong  $\alpha$ -fiber, namely  $\{112\}\langle 110 \rangle$ ,  $\{111\}\langle 110 \rangle$ ,  $\{001\}\langle 110 \rangle$  and moderate  $\gamma$ -fibre orientation which

includes  $\{111\}\langle 112\rangle$ . This agrees fully with the previous observation that the  $\{111\}\langle 110\rangle$  and  $\{112\}\langle 110\rangle$  texture become strong when amount of cold reduction is greater than 70% [87, 88]. Khatirkar et al [89] observed that a strong  $\gamma$ -fibre will be developed in the cold rolled state if the initial orientation is  $\{111\}\langle 112\rangle$  and if two  $\{111\}\langle 112\rangle$  type of grains are neighbours, their grain boundary region will rotate towards the common stable end rotation. As may be seen from the ODFs in Figure 6-14 above, it is evident that that the rotation path B was followed during the cold working process. It is also evident that an increase in deformation led to an increase in the intensity of the rolling texture. The intensity of  $\{223\}\langle 110\rangle$  increased from 12 in 62% cold rolled specimen to 18 in 82% cold rolled specimen. This is in agreement with the observations made by Ray et al [68] where they found that the rolling texture is solely dependent on amount of cold reduction not composition as latter have effect of recrystallisation texture. Furthermore, Ushioda et al [90] found that cold rolling textures are neither influenced by the carbon content nor the state of dispersion in low carbon steels.

The amount of stored energy during cold working increases with an increase in the amount of deformation. However grains of different orientation will have different amount of stored energy i.e. grain having  $\{100\}$  orientation have different amount of energy compared to  $\{111\}$ . The amount of stored energy due to deformation increases in the sequence  $\{100\} < \{112\} < \{111\}$  and the highest values were found in the  $\{011\}$  oriented grains [71]. This stored energy is the driving force for recrystallisation on annealing.

However it was stated in literature that increasing the amount of cold reduction above 80% to about 95% leads to progressively increase in the  $\{100\}\langle 011\rangle$  texture [91]. This may explain the reason why there was a decrease in  $R_m$ -value after 82% cold reduction (to be discussed latter).  $\{100\} \langle 011\rangle$  fibre has a negative influence on the formability of materials as it results in low  $R_m$ -values.

#### **6.2.3.2. Annealing texture**

As may be seen from Figure 6-15 below, the texture of as-received annealed steel is characterised by strong  $\{111\}\langle 110\rangle$ ,  $\{554\}\langle 225\rangle$  and weak  $\{111\}\langle 112\rangle$ . It is

important to note that a weak Cube-on-face texture still prevails even after annealing at 1025°C. This is undesirable as Cube-on-face texture is known to exhibit a negative influence on the formability and ridging of ferritic stainless steels.

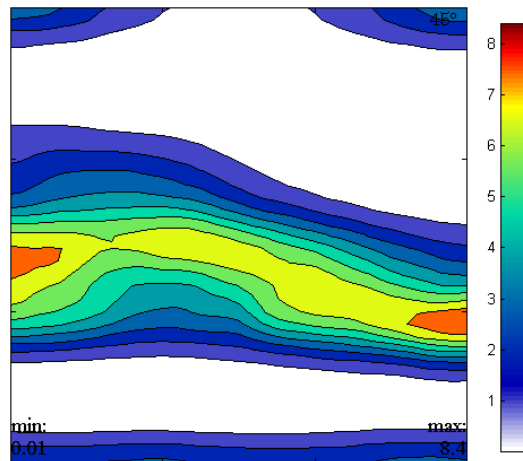


Figure 6-15: Bunge ODF  $\phi_2 = 45$  section showing the presence of relatively strong  $\gamma$ - and weak  $\alpha$ -fibres of the as-received cold rolled and annealed steel B.

#### 6.2.3.2.1. Texture evolution in 78% cold worked and annealed at different temperature

As may be seen from Figure 6-16 below, steels which were cold rolled at 78% and annealed at 900°C and 950°C are characterised by both  $\alpha$ -fibre and  $\gamma$ -fibre orientations with the maxima at  $\{554\}\langle 225 \rangle$ ,  $\{111\}\langle 110 \rangle$  and  $\{111\}\langle 112 \rangle$ . However there was a significant changes in texture after annealing at 900 and 950°C, indicating that recrystallisation has taken place. These two annealing temperatures of 900 and 950°C clearly show that at lower annealing temperatures the annealing texture (the  $\gamma$ -fiber component) is not fully developed. Shin et al [60] indicated that the presence of  $\{334\}\langle 483 \rangle$  and  $\{111\}\langle 112 \rangle$  component proves that recrystallisation has just started to take place i.e. the presence of the  $\{111\}\langle 112 \rangle$  orientation at annealing. The  $\alpha$ -fibre and homogeneous  $\gamma$ -fibre texture formation are evident characteristic of recrystallisation [92]. As may be seen from Figure 6-16 above, when the annealing temperature was increased to 1025°C, the  $\gamma$ -fibre transformation was somewhat retarded and instead  $\gamma$ -fibre shifted to  $\{334\}\langle 483 \rangle$  and  $\{554\}\langle 225 \rangle$ . The  $\{334\}\langle 483 \rangle$  is a texture which is shifted from  $\{111\}\langle 112 \rangle$  by about 8° [63]. Both  $\{554\}\langle 225 \rangle$  and  $\{334\}\langle 483 \rangle$  are recrystallisation texture and are related to the  $\alpha$ -

fibre  $\{112\}\langle 110\rangle$  by a  $26^\circ\langle 110\rangle$  which is close to a  $27^\circ\langle 110\rangle$  relationship having high mobility in bcc grain boundaries [8].

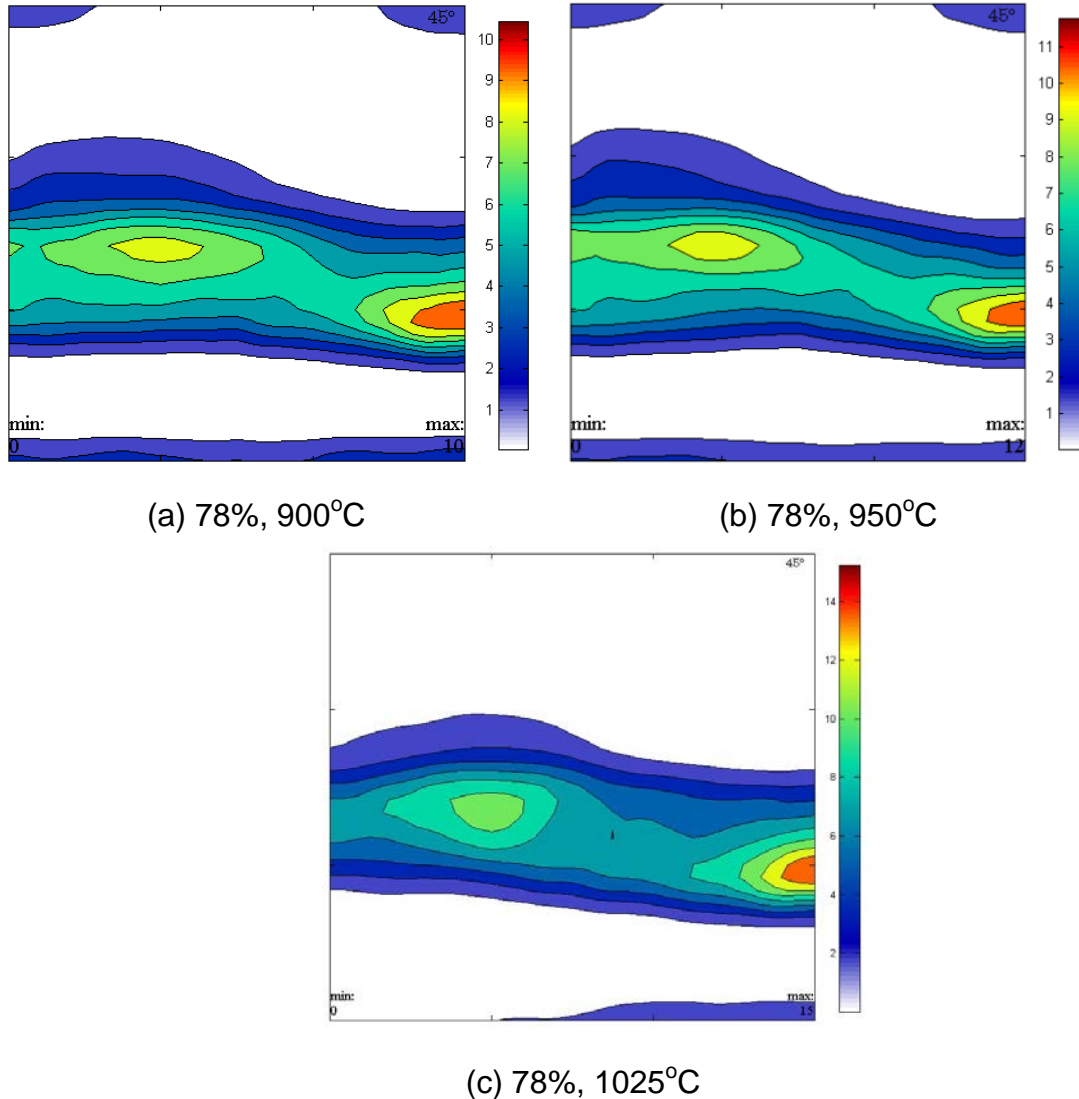


Figure 6-16: Bunge ODF  $\phi_2 = 45$  section for steels cold rolled 78% and annealed at 900, 950 and 1025°C for 300s.

No cube-on-face or rotated cube texture was observed at the higher annealing temperature of 1025°C i.e. the  $\{001\}\langle 110\rangle$  component eventually transformed into shifted  $\gamma$ -fibre orientation after recrystallisation which is in agreement with earlier work [93, 94]. However the transformation rate from  $\{001\}\langle 110\rangle$  to  $\{111\}\langle 112\rangle$  is too slow because the former has low stored energy. This can either be removed by

increasing the annealing temperature or holding time and hence after increasing to 1025°C from 900°C, no cube-on-face texture was found.

### 6.2.3.2.2. Texture evolution in 82% Cold worked and annealed at different temperature

The evolution of texture in the 82% cold rolled steels as indicated in Figure 6-17 is similar to the 78% ones after annealing at 900 and 950°C i.e. strong shifted  $\{111\}\langle 110\rangle$  texture and moderate  $\{111\}\langle 112\rangle$ . However after annealing at 1025°C, no cube-on-face texture component of the  $\{100\}$  plane is observed.

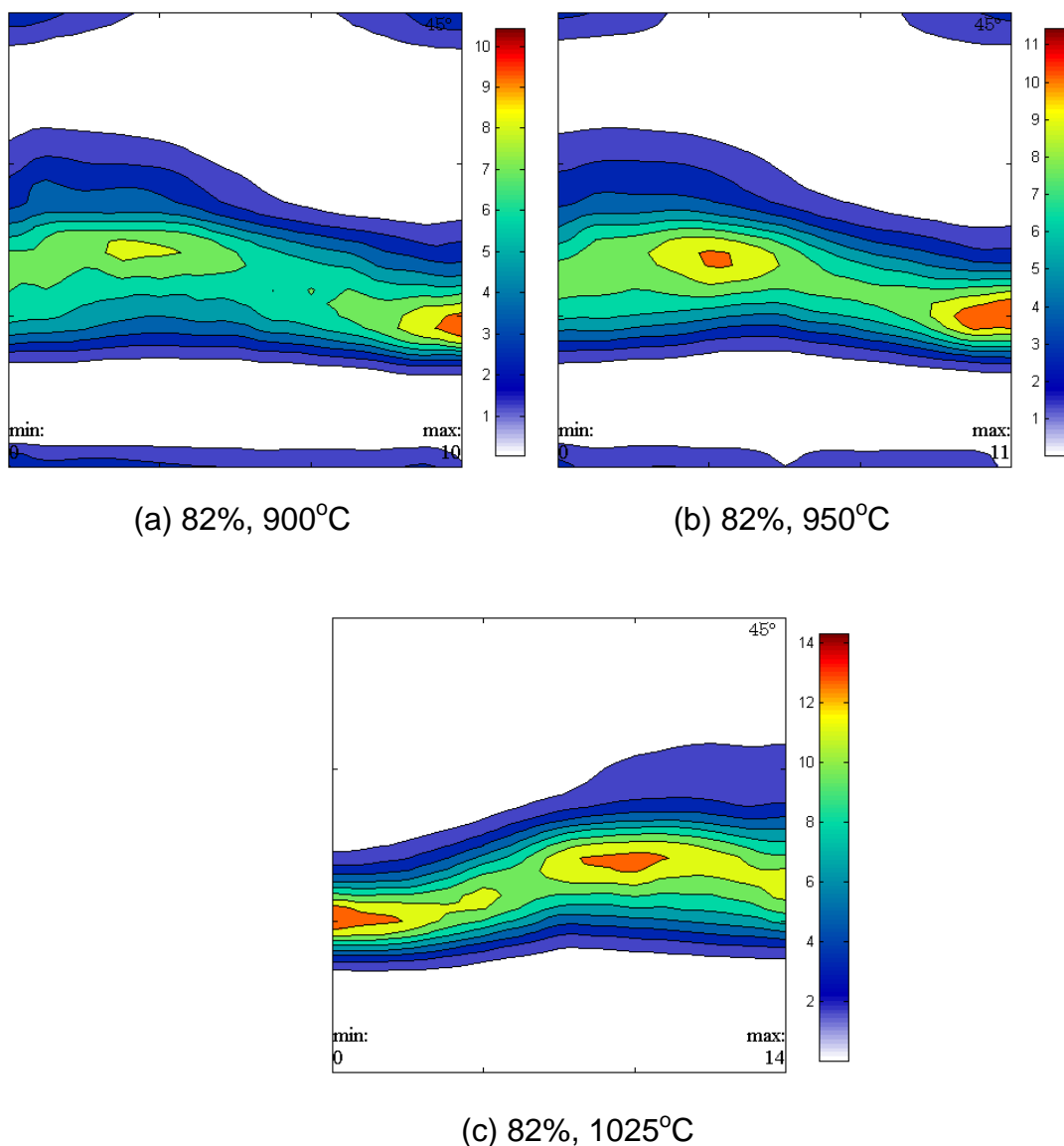


Figure 6-17: Bunge ODF  $\phi_2 = 45$  section for steels cold rolled 82% and annealed at 900, 950 and 1025°C for 300s

### 6.2.3.2.3. Formation of shifted $\gamma$ -fibre

The selective growth mechanism may have played an important role in the formation of these two annealing texture i.e.  $\{334\}\langle 483\rangle$  and  $\{554\}\langle 225\rangle$  in both steels which were cold rolled 78 and 82%. It has been proposed by Raabe and Lucke that the retarding force of fine particles are responsible for a strong growth selection during recrystallisation which leads to the growth of  $\{334\}\langle 483\rangle$  nuclei into the  $\{112\}\langle 110\rangle$  deformation matrix [95-97]. This lead to the strong formation of  $\gamma$ -fibre recrystallisation texture with a strong shifts towards  $\{334\}\langle 483\rangle$  in ferritic stainless steels.

### 6.2.4. Annealing parameter

The relationship between the texture parameter  $\log_{10}\left(\frac{I_{(111)}}{I_{(100)}}\right)$  and annealing temperature T is shown in Figure 6-18 below. This clearly indicates that increasing the annealing temperature increases the  $\{111\}$  texture, hence, the higher  $R_m$ -values as will be seen in section 6.3. Equation 6-1 was developed from the results obtained with the correlation coefficient of  $R^2 = 1$ .

$$\log_{10}\left(\frac{I_{(111)}}{I_{(100)}}\right) = 0.086T_{anneal} - 73.38 \dots\dots\dots 6-1$$

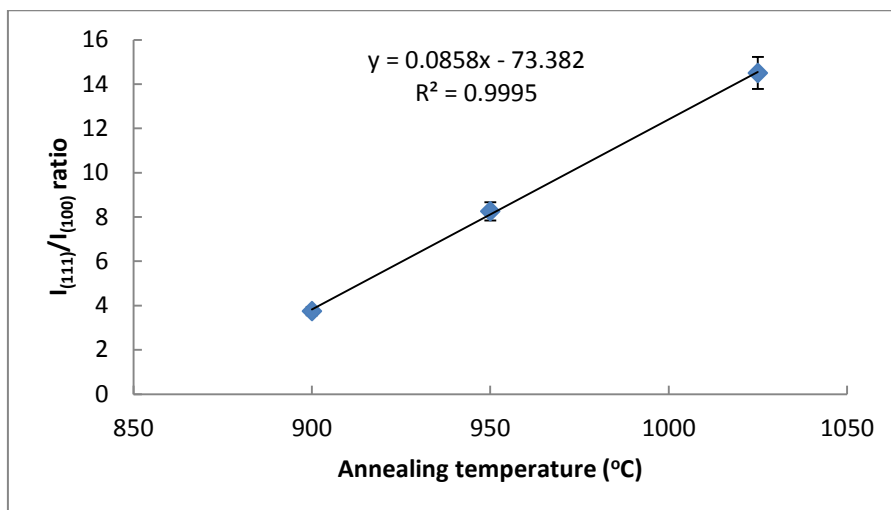


Figure 6-18: Effect of annealing temperature on the texture parameter of AISI 441 ferritic stainless steel after 78 and 82% cold reduction.

### 6.3. Effect of thermomechanical processing on formability

In order to assess the effect of amount of cold reduction and annealing temperature on formability of AISI 441 ferritic stainless steel sheets, the R-value of the cold rolled and annealed sheets were analysed. Calculated  $R_m$  and  $\Delta R$  values for three different temperatures are shown in Table 6-1. To optimise the deep drawability as defined by Lankford parameter, the  $R_m$ -value should be maximised and the  $\Delta R$ -value should be minimised i.e. as close to zero as possible.

Table 6-1: Effect of thermomechanical processing on formability as measured by the  $R_m$ -value and  $\Delta R$

Annealing T	900°C		950°C		1025°C	
	$R_m$	$\Delta R$	$R_m$	$\Delta R$	$R_m$	$\Delta R$
<b>62% CW</b>	-	-	-	-	1.4	0.4
<b>78% CW</b>	1.2	0.2	1.5	0.6	2.0	0.6
<b>82% CW</b>	-	-	1.3	0.5	1.7	0.5

The steels which were cold rolled 78 and 82% respectively and annealed at 1025°C, exhibited the highest  $R_m$ -value although their  $\Delta R$  is higher than expected with values far removed from zero. It is evident that the high  $R_m$ -values are associated with the strong  $\gamma$ -fibre  $\{111\}$ //ND as the 78% and 82% cold rolled steels annealed at 1025°C show higher intensity of  $\{111\}$  orientations parallel to the normal direction compared to the 62% CW steel annealed at the same temperature, see Figure 6-19 below. This observation is in agreement with Pickering and Lewis [16] that high  $\{111\}$  orientations are associated with high amounts of deformation in excess of 75%.



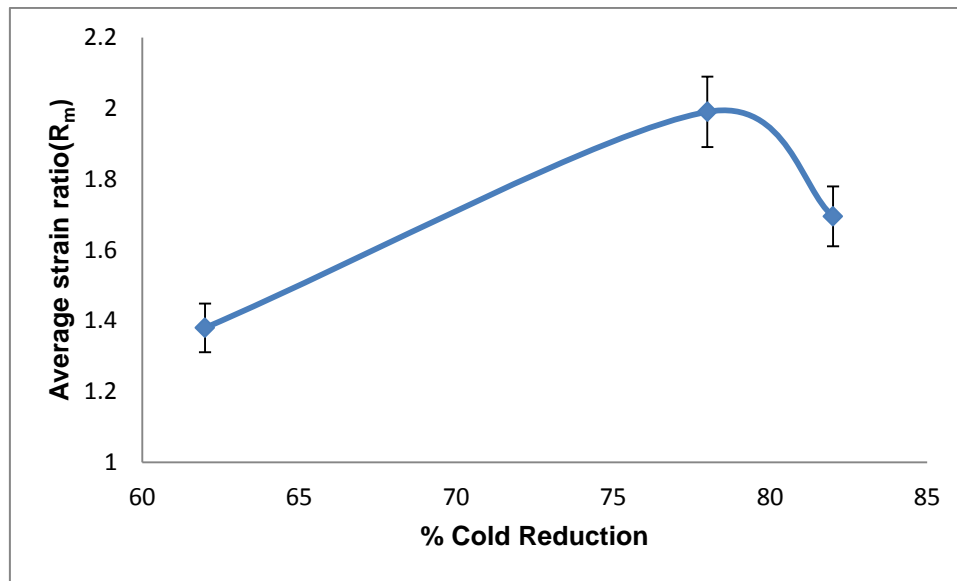


Figure 6-19: Effect of percentage cold reduction on average strain ratio ( $R_m$ -value) for steels annealed at 1025°C for 300s.

Increasing the amount of cold reduction increases the non-uniform deformation regions which act as nucleation sites for {111} texture [69]. At 1025°C, 78% cold rolled steels shows higher  $R_m$ -value compared to 82% cold rolled steels. This may be explained by difference in grain size as will be discussed in chapter 6.

The 62% industrially cold rolled steels which were annealed at 1025°C exhibits the Cube texture which has a negative influence on formability, hence, the lower  $R_m$ -value of 1.4. The intensity of {554}<225> is lower for 62% cold rolled steel compared to 78 and 82% cold rolled steels after annealing. As may be seen from Table 6-1 above, no results were obtained from the steels which were given a cold reduction of 82% and annealed at 900°C as they fracture before a tensile strain of 10% and, therefore, comparable results could not be obtained.

### 6.3.1. Formability parameter

The relationship between the  $R_m$  value and the texture parameter  $\log_{10}(I_{(111)}/I_{(100)})$  is shown in Figure 6-20. Figure 6-20 clearly indicated that the development of high  $R_m$  value is favoured by increasing the intensity of the {111} recrystallisation texture relative to the {100}.

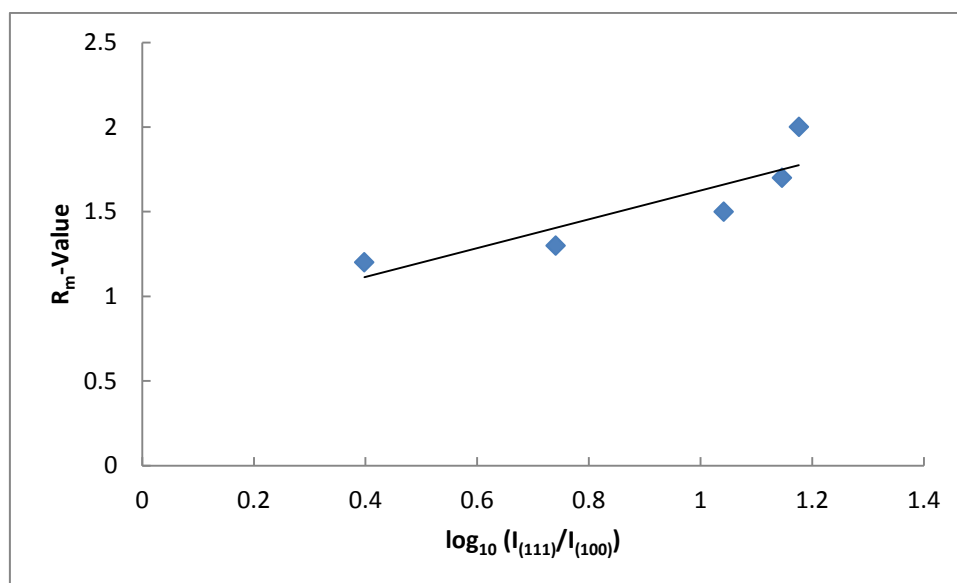


Figure 6-20: Relationship between  $R_m$ -value and the texture parameter  $\log_{10} \left( \frac{I_{(111)}}{I_{(100)}} \right)$  of AISI 441 ferritic stainless steel after being annealed at 900, 950 and 1025°C for 300s

This indicates that for improved formability or deep drawability characteristics, {111} texture orientation must be optimised. The fitted linear equation is given by equation 6-2 below with the correlation coefficient of  $R^2 = 0.8$ .

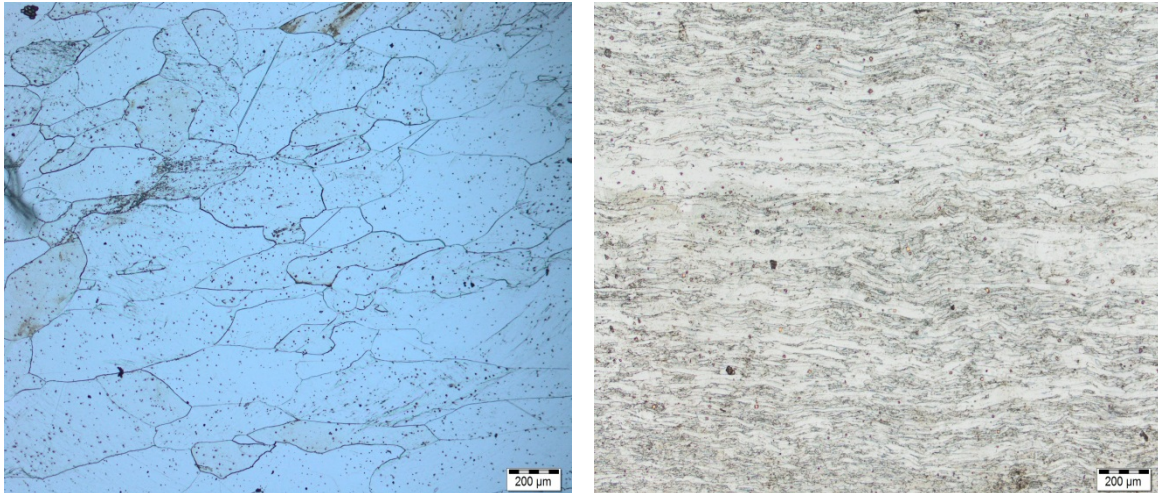
$$R_m = 0.77 + 0.85 \log_{10} \frac{I_{(111)}}{I_{(100)}} \dots\dots\dots 6-2$$

#### 6.4. Effect of (Nb+Ti) content Ratio on microstructural evolution, mechanical properties and texture evolution in AISI 441 ferritic stainless steel

##### 6.4.1. Effect of (Nb+Ti) content on microstructural evolution of the hot band

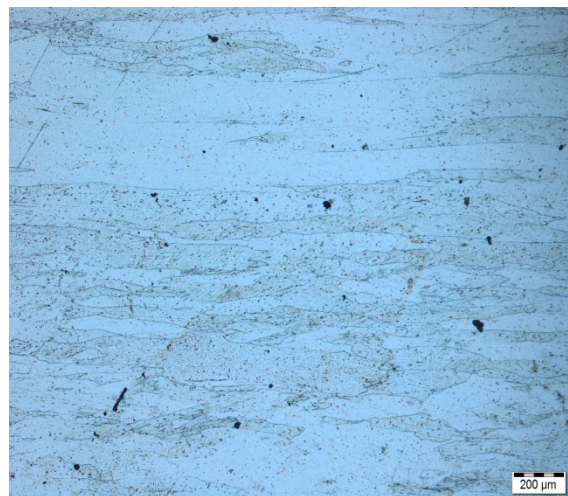
The microstructures of the as-received hot band sheets are shown in Figure 6-21 below. Steel A, which has small amounts of (Nb+Ti) content, exhibits larger deformation bands oriented along the rolling direction compared to steel B and C. It can also be observed that steel A has some equiaxed grains and this suggest that some dynamic recovery took place during hot rolling whereas steels B and C show pan-caked grain structure which indicates that recrystallisation had not taken place during and after hot rolling. The grains are highly elongated in the rolling direction and the width of the deformation bands decrease with an increase in the (Nb+Ti)

content. This is not surprising as Nb is known to increase the recrystallisation temperature and retard recrystallisation [98].



(a)

(b)



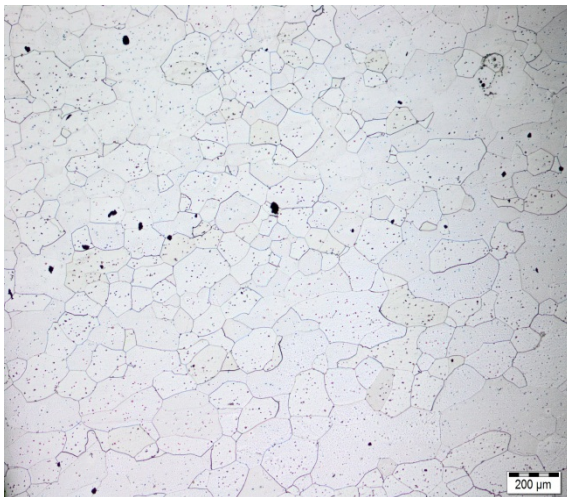
(c)

Figure 6-21: Effect of (Nb+Ti) content on the hot band microstructure of AISI 441 ferritic stainless steels: (a) steel A with 0.26Nb+0.2%Ti (b) steel B with 0.44Nb and 0.15Ti (c) steel C with 0.7%Nb and 0.32% Ti.

#### 6.4.2. Effect of (Nb+Ti) content on microstructural evolution of the annealed hot band

Ferritic stainless steels are difficult to recrystallise during hot rolling because they easily undergo dynamic recovery, therefore, they have to be annealed to remove the

elongated, banded microstructure. After annealing the hot band specimen, the grain sizes for steels A, B and C were found to be  $94\pm 8\mu\text{m}$ ,  $46\pm 6\mu\text{m}$  and  $93\pm 10\mu\text{m}$ . As the (Nb+Ti) content increases, there is a slow rate of dynamic recovery and the driving force consumed by the latter is minimised. Therefore more deformation energy is preserved for static recrystallisation. Therefore higher driving force for recrystallisation results in finer microstructure as (Nb+Ti) content increases. Large grain size in steel C after annealing is surprising because the steels with higher (Nb+Ti) content are expected to possess finer grain size than the steels with low (Nb+Ti) content. However in this work it would appear the decrease in grain size with additions of (Nb+Ti) content goes through a minimum before it starts increasing again and this should be a suggest for further investigation.

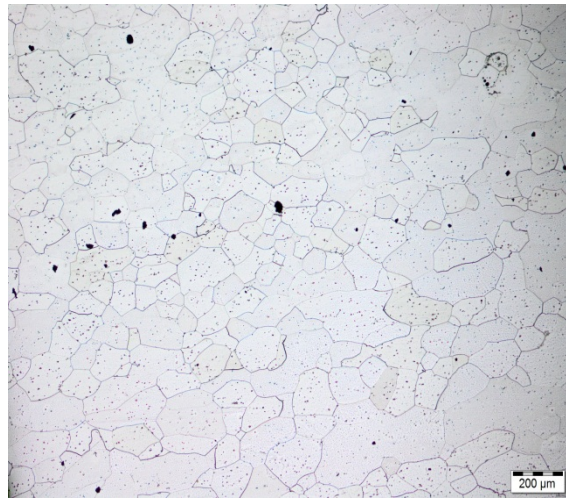


(a)



(b)





(c)

Figure 6-22: Effect of (Nb+Ti) content on the hot band microstructure of AISI 441 ferritic stainless steels after annealing at 1025°C for 300s: (a) steel A with 0.26Nb+0.2%Ti (b) steel B with 0.44Nb and 0.15Ti (c) steel C with 0.7%Nb and 0.32% Ti.

#### 6.4.3. Effect of (Nb+Ti) content on the microstructural evolution after 62% cold working

Figure 6-23 shows the microstructures of the three steels A, B and C after 62% cold. As may be seen, the microstructure is composed of elongated ribbon like grains with a large number of interior shear deformations. Deformation results in the elongation of original grains along the rolling direction axis. The formation of a number of strain induced grain boundaries appears as deformation microband. The sub- and grain boundaries tend to arrange themselves more parallel to the rolling direction with increasing strain and the spacing between them tend to decrease with an increase in (Nb+Ti) content. This might be due to the differences in the initial microstructures where steel C with the highest (Nb+Ti) content was not fully recrystallised, see Figure 6-23 above. All three cold rolled materials show similar wavy fields and some of the wavy fields are strongly etched and some are lightly etched.

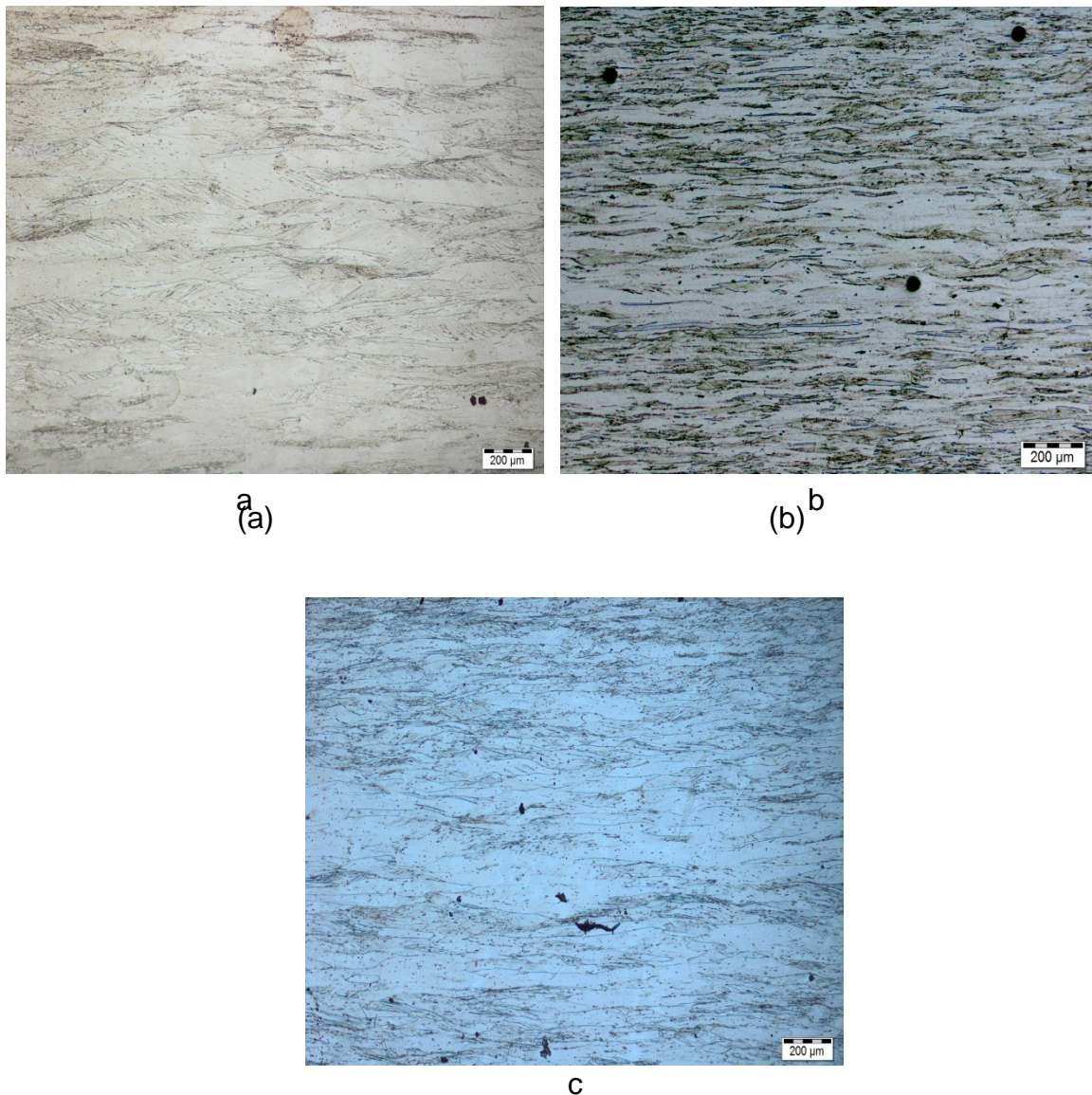


Figure 6-23: Effect of (Nb+Ti) on the microstructure of 62% cold worked AISI 441 ferritic stainless steels. (a) Steel A with 0.26Nb+0.2%Ti (b) steel B with 0.44Nb and 0.15Ti (c) steel C with 0.7%Nb and 0.32% Ti.

#### 6.4.4. Effect of (Nb+Ti) content on the microstructural evolution after 62% cold working and annealing

Figure 6-24 shows the optical microstructures of the three steels namely A, B and C after 62% cold working and annealing at 1025°C for 600s. The grain sizes of steels A, B and C were found to be  $87\pm 13\mu\text{m}$ ,  $100\pm 6\mu\text{m}$  and  $34\pm 2\mu\text{m}$  respectively. This was unexpected as an increase in (Nb+Ti) content is known to pin grain boundary as a results finer microstructure was expected in steel B compared to steel A. However, by looking at the standard deviation, it can be said that grain size in steel A and steel



B does not differ significantly. As mentioned earlier, steel B was industrially cold worked and, therefore, there is a possibility that the deformation (driving force for recrystallisation) could be higher than 62%. Increasing the (Nb+Ti) content to 1.02% in steel C, as expected, led to a decrease in grain size as a result of grain pinning by Nb(C,N) [84].

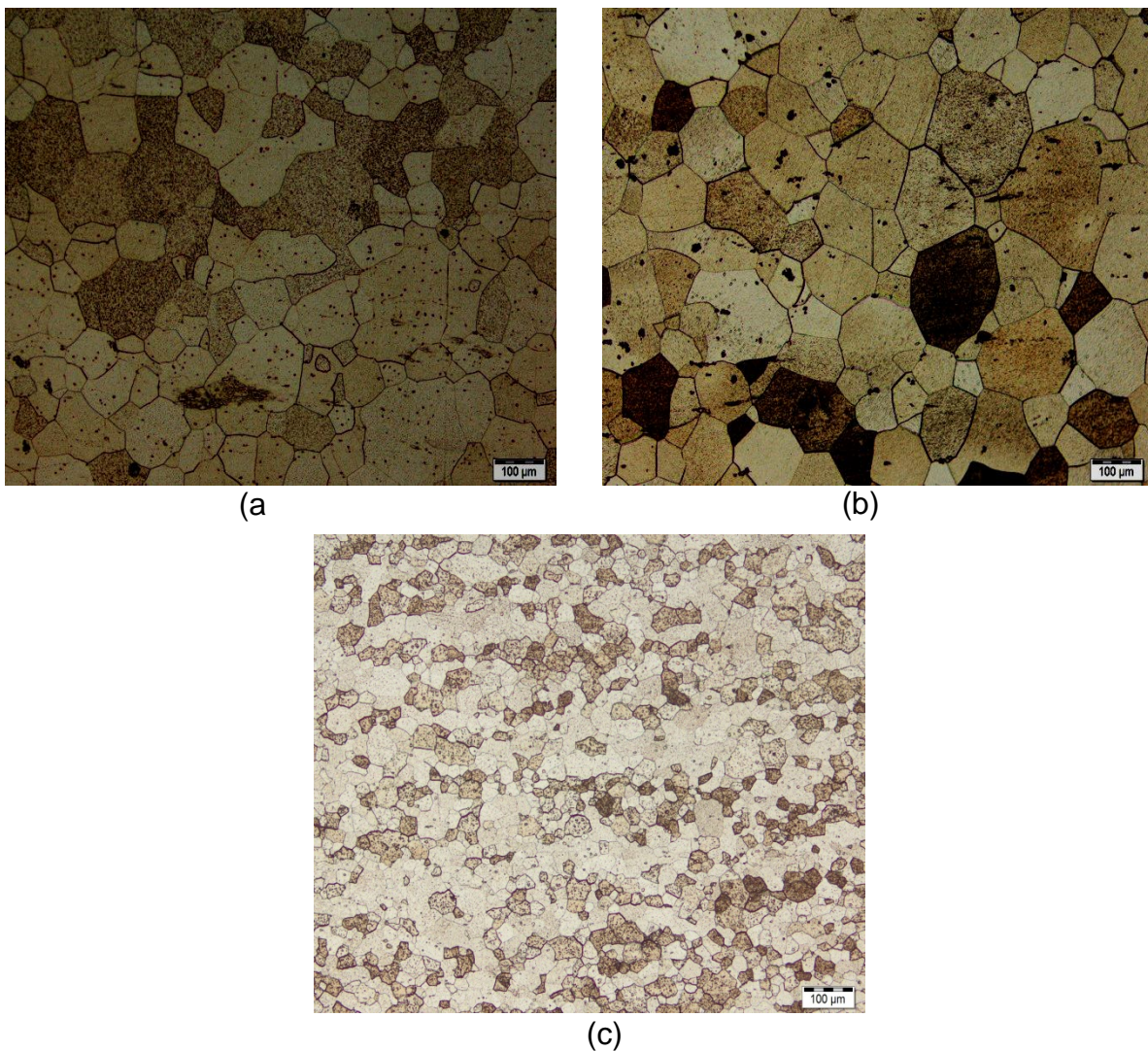


Figure 6-24 : Effect of (Nb +Ti) content on the Microstructure of 62% cold worked and annealed at 1025°C for 300s. (a) Steel A with 0.26Nb+0.2%Ti (b) steel B with 0.44Nb and 0.15Ti (c) steel C with 0.7%Nb and 0.32%Ti

### 6.4.5. Effect of (Nb+Ti) content on recrystallisation kinetics

Hardness measurements were taken to track the recovery and recrystallisation after annealing at 1025°C for different times. As may be seen in Figure 6-25 below, the hardness dropped significantly after 60s. In all three steels, the decrease in hardness after between 60s and 90s is attributed to the recrystallisation during the annealing process. However in steels B and C, the recrystallisation process is “sluggish”. In steel A, the hardness values level off at about  $H_V(300) = 130$  after 60s while steels B and C they level off at  $H_V(300) = 145$  and 153 after 90 and 150s respectively. This indicates that recrystallisation completed after 60s for steel A, 90s for steel B and 150s for steel C. An increase in (Nb+Ti) content leads to an increased recrystallisation temperature or delayed recrystallisation. As may also be seen in Figure 6-25, steels B and C exhibit higher hardness in the fully annealed condition and this may be attributed to the precipitation and solid solution hardening caused by Nb and Ti additions.

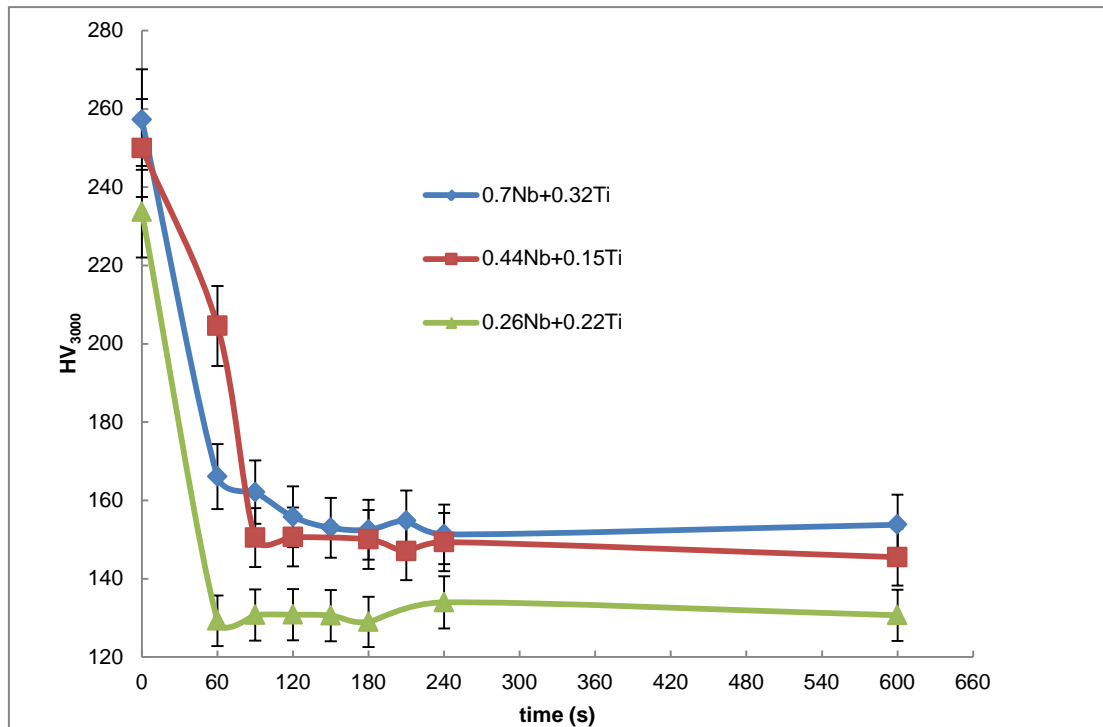


Figure 6-25: Effect of (Nb+Ti) content on the recrystallisation kinetics of AISI 441 ferritic stainless steel after annealing at 1025°C for different times.



#### 6.4.6. Effect of (Nb+Ti) content on mechanical properties of ferritic stainless steel after annealing at 1025°C for 180 minutes.

Table 6-2 shows the effect of Nb+Ti content on the mechanical properties of AISI 441 ferritic stainless steel. It was found that an increase in (Nb+Ti) content led to an increase in both the yield and ultimate tensile strength of the steel as shown by steels A and B. However, further increase in (Nb+Ti) content to 1.06 slightly increased both yield and tensile strength.

Table 6-2: Effect of (Nb+Ti) content on mechanical properties of ferritic stainless steel after annealing at 1025°C.

	Steel A (0.22Nb+0.2Ti)	Steel B (0.44Nb+0.15Ti)	Steel C (0.7Nb+0.36Ti)
Ultimate tensile strength (MPa)	353.6±2.0	444±4.0	447.75±8.0
0.2% offset yield strength (MPa)	216.6±13.6	289.8±3.0	292.9±3.3

However, after increasing (Nb+Ti) content to 1.06, there was a decrease in yield strength and UTS. This may be due to the fact that maximum solubility of Nb in ferritic stainless steel was reached and excess Nb started to have negative influence on mechanical properties. Fujita et al [9] found that the proof strength of the ferritic stainless steels annealed at 1000°C increases with increasing the Nb content up to 0.8%. However when increasing annealing temperature to 1250°C, it was found that the proof strength increases linearly with the increase in Nb content. High proof strength can be obtained when the (C+N) content is less than 0.02% and when annealing temperatures are high. The increase in strength after annealing is mainly due to solid solution strengthening caused by Nb.

#### 6.4.7. Effect of (Nb+Ti) content on texture evolution

##### 6.4.7.1. Effect of (Nb+Ti) content on hot band texture

Figure 6-26 shows the effect of chemical composition on the hot band texture. As may be seen from Figure 6-26, steels A and B exhibited strong  $\alpha$ -fibre and weak  $\gamma$ -fibre and steel C exhibited strong  $\gamma$ -fibre and weak  $\alpha$ -fibre after hot rolling. The  $\gamma$ -fibre in steel C had a higher intensity and distributed more uniform than that in the steel A and B. In steel A, the maximum intensity was found at  $\{223\}\langle 100\rangle$  with some weak  $\{001\}\langle 110\rangle$  while in steel B, the maximum texture intensity was found to be  $\{001\}\langle 110\rangle$ , a typical orientation caused by plain strain deformation [45]. The maximum intensity was found to be  $\{111\}\langle 110\rangle$  in steel C. It has been reported that  $\{001\}\langle 110\rangle$  and  $\{112\}\langle 110\rangle$  oriented crystals have a low recrystallisation rate [99]. However these textures can be weakened by very low deformation temperature which will result in larger accumulated stored energy and a low dynamic recovery rate. This is favourable for the texture rotation from  $\{001\}\langle 110\rangle$  toward relatively stable  $\alpha$ -fibre and  $\gamma$ -fibre [94]. This will reduce the intensity of deleterious  $\{001\}\langle 110\rangle$ . However increasing the (Nb+Ti) content to 1.06, texture was characterised by only  $\gamma$ -fibre with no texture component in (100) plane. The maximum intensity was found at  $\{112\}\langle 110\rangle$ .

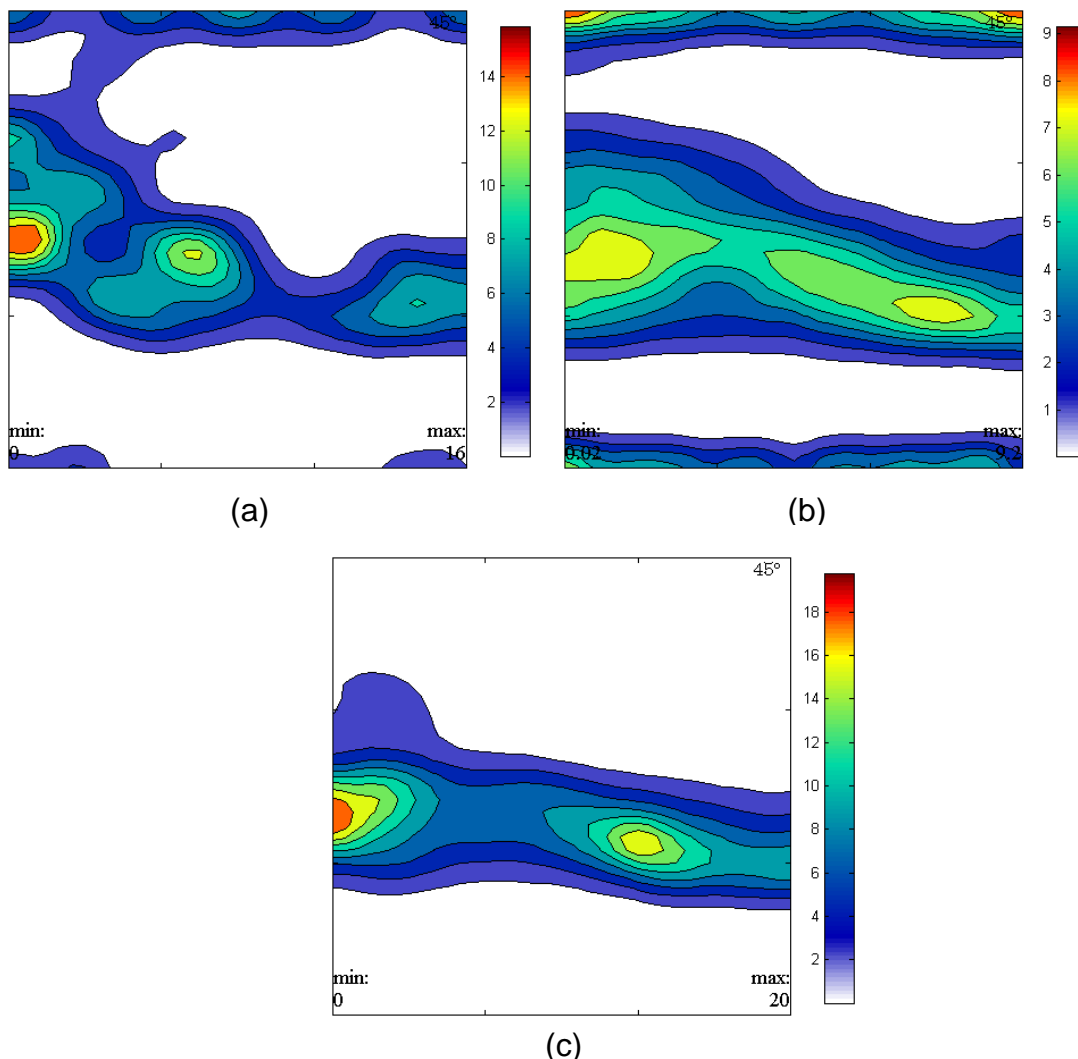


Figure 6-26: Effect of (Nb+Ti) on the Texture Evolution of Hot Band (a) steel A with 0.26Nb+0.2%Ti (b) steel B with 0.44Nb and 0.15Ti and (c) steel C with 0.7%Nb and 0.32% Ti.

#### 6.4.7.2. Effect of (Nb+Ti) content on annealed hot band texture

Figure 6-27 shows the  $\phi_2 = 45^\circ$  sections of the ODFs measured in the centre of the annealed hot band sheets. Texture of steel B after annealing is characterised by both  $\gamma$ -fibre and  $\alpha$ -fibre with  $\{110\}\langle 100 \rangle$  orientation having highest intensity. Comparing Figure 6-27b with Figure 6-27a, it can be seen that annealing the hot band intensified both the  $\gamma$ -fibre and  $\alpha$ -fibre. In other words, annealing of the medium to high (Nb+Ti) content hot band intensified the  $\{110\}\langle 100 \rangle$  orientation which has negative effect on the drawability and ridging resistance of the steel. This is more prominent in steel C whereby the  $\alpha$ -fibre (rotated cube) is introduced after annealing the hot band, see Figures 6-27c and 6-27b.

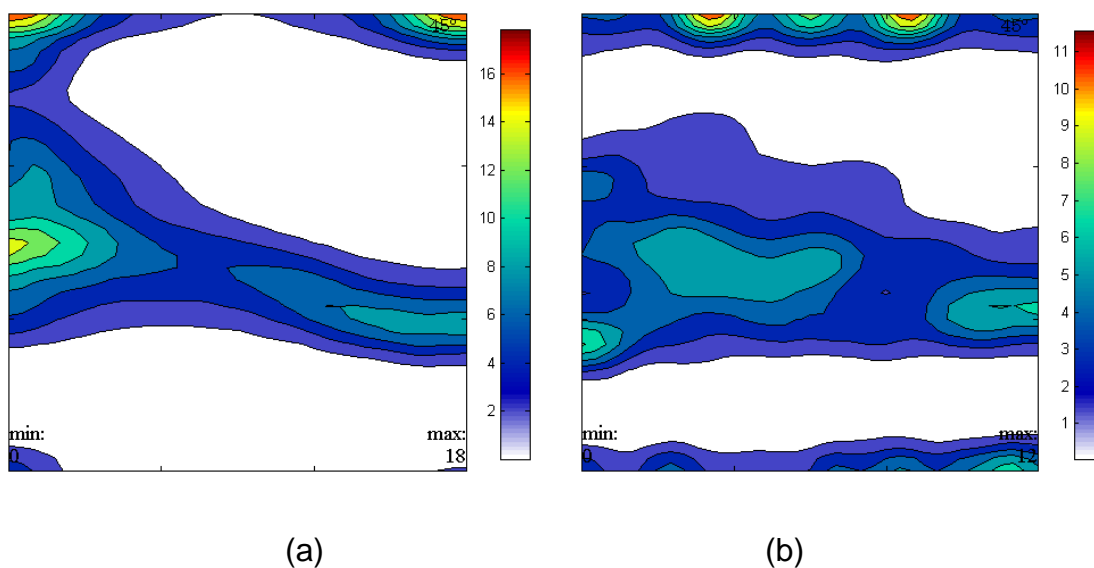


Figure 6-27: Effect of (Nb+Ti) on the texture evolution of hot band after annealing at 1025°C for 300s. (a) 0.44Nb and 0.15Ti (b) 0.7%Nb and 0.32% Ti.

### 6.4.7.3. Effect of (Nb+Ti) content on cold worked steels

Sections of the ODF for the steels A, B and C after given 62% cold reductions are given in Figures 6-28 to 6-30 below respectively. As may be seen in all steels there is both  $\alpha$ - and  $\gamma$ -fibre. However, the  $\gamma$ -fibre is stronger in Steels B and C with higher (Nb+Ti) content than steel A.

As may be seen from Figure 6-29 below, the texture of steel A is characterised by strong  $\alpha$ -fibre i.e.  $\{112\}\langle 110\rangle$  and strong  $\gamma$ -fibre i.e.  $\{554\}\langle 225\rangle$  i.e. the texture in Steel A is characterised by both RD// $\langle 110\rangle$  and ND// $\langle 111\rangle$  with the maximum peaks at  $\{112\}\langle 110\rangle$ . A similar pattern is also observed in Steel B. This is typical texture of deformation texture in BCC steels [15]. However, steel C with the highest (Nb+Ti) content is characterised by strong  $\gamma$ -fibre i.e.  $\{554\}\langle 225\rangle$  and strong  $\alpha$ -fibre i.e.  $\{100\}\langle 110\rangle$ , and shifted  $\{112\}\langle 110\rangle$ . By analysing Figure 6-28 to Figure 6-30, it can be seen that increasing the amount of (Nb+Ti) content lead to increased  $\{100\}\langle 110\rangle$  orientation i.e. intensity  $f(g)$  of  $\{100\}\langle 110\rangle$  increased from 4 in steel A to 11 in steel C.

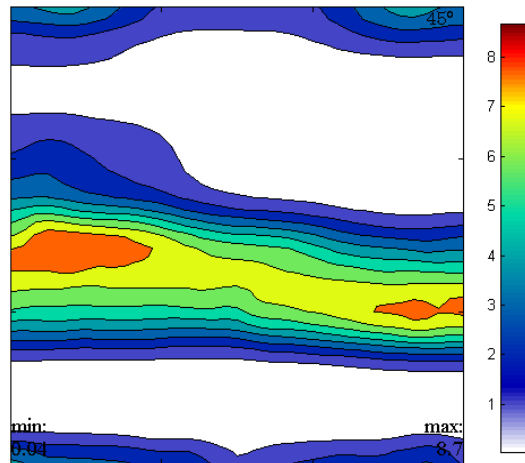


Figure 6-28: the  $\varphi_2 = 45^\circ$  sections of the ODFs measured in the centre of the steel A with 0.26Nb+0.2Ti 62% cold worked sheets.

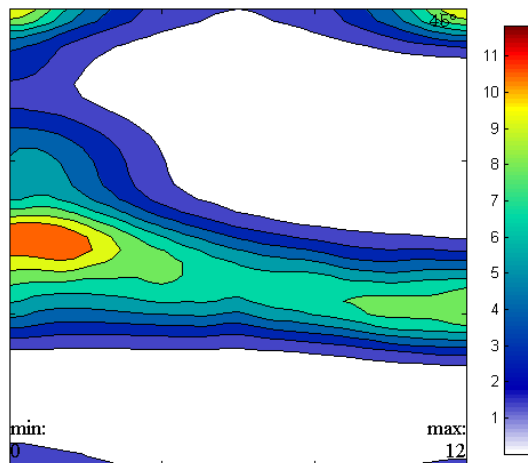


Figure 6-29: the  $\varphi_2 = 45^\circ$  sections of the ODFs measured in the centre of the 0.44Nb+0.15Ti 62% cold worked sheets.

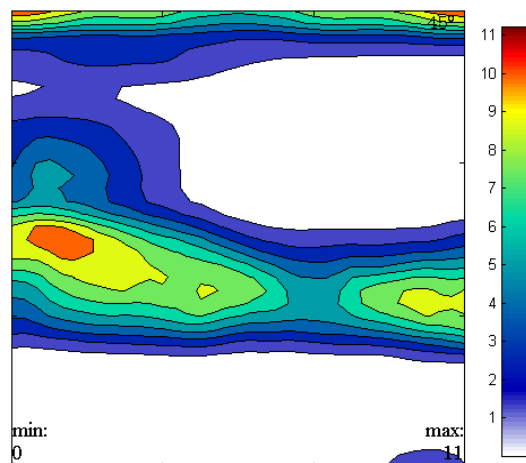


Figure 6-30: the  $\varphi_2 = 45^\circ$  sections of the ODFs measured in the centre of the 0.7Nb+0.32Ti 62% cold worked sheets.

#### 6.4.7.4. Effect of (Nb+Ti) content on cold worked and annealed steels

Figures 6-31 below shows sections of the ODFs for steels A, B and C after 62% cold reduction and annealing at 1025°C for 300s. Subsequent annealing treatment after cold working induces recrystallisation texture which is dependent on the nucleation sites for recrystallised grain. As may be seen, steel A is characterised by  $\{100\}\langle 100\rangle$ ,  $\{111\}\langle 110\rangle$  and  $\{554\}\langle 225\rangle$ . The texture of steel B is characterised by strong  $\{111\}\langle 110\rangle$ ,  $\{554\}\langle 225\rangle$  and weak  $\{111\}\langle 112\rangle$  while that of steel C is characterised by weak cube texture and strong  $\gamma$ -fibre, namely  $\{554\}\langle 225\rangle$  and  $\{111\}\langle 110\rangle$ . However the intensity of the three steels is almost the same and this was not expected as Nb and Ti are known to increase intensity of  $\gamma$ -fibre. Inagaki et al [93] observed that the addition of Ti and Nb enhances the formation of the  $\gamma$ -fibre (more precisely,  $\{554\}\langle 225\rangle$  recrystallisation texture. This is partly due to the effect of Ti and Nb on the rolling texture i.e. the rotation of  $\{554\}\langle 225\rangle$  to  $\{111\}\langle 225\rangle$  during cold rolling is suppressed by Ti and Nb addition and this leads to the grains with  $\{554\}\langle 225\rangle$  being strongly strained. Therefore strong  $\{554\}\langle 225\rangle$  recrystallisation texture originate from severely deformed  $\{554\}\langle 225\rangle$  grains. By analysing all three texture results collectively, it can be seen that increasing the (Nb+Ti) content does not seem to have an effect on the overall texture intensity. However, increasing (Nb+Ti) content lead to an enhanced  $\gamma$ -fibre. This requires further micro-texture investigation using SEM-EBSD.

It has been shown in literature that a combination of high  $r$ -valued  $\{111\}$  and low  $r$ -valued  $\{100\}$  orientation in the recrystallisation texture of final products lead to ridging [62, 63].

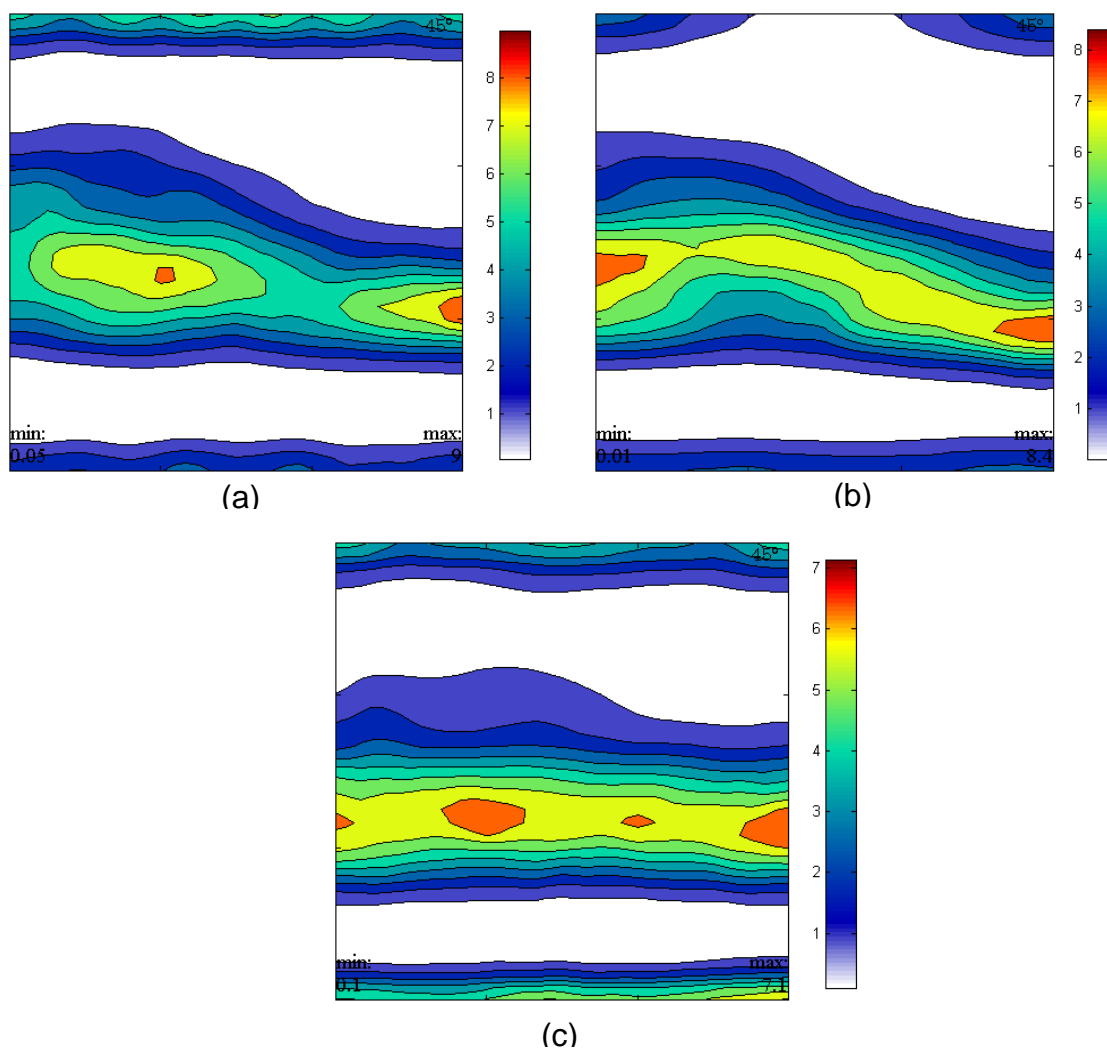


Figure 6-31: Effect of ( Nb +Ti) content on the cold worked after annealing at 1025 for 300s annealed of AISI 441 ferritic stainless steels. (a) Steel A with 0.26Nb+0.2%Ti (b) steel B with 0.44Nb and 0.15Ti (c) steel C with 0.7%Nb and 0.32% Ti.

### 6.5. Effect of (Nb+Ti) content on ridging resistance

Surface ridging behaviour was investigated on the three steel steels A, B and C in the cold rolled and annealed condition. Figure 6-32 shows the roughness profiles along the transverse direction of the strips after subjecting them to the tensile strain of 0.1. As may be seen, steel A shows less resistance against surface ridging with the average roughness  $R_a$  of  $1.5\mu\text{m}$  followed by steel B with average roughness  $R_a$



of  $1.1\mu\text{m}$ . Steel C shows highest resistance to ridging with the average roughness  $R_a$  of  $0.64\mu\text{m}$ . It is evident that increasing the (Nb+Ti) content increases the ridging resistance as measured by the ridging height (or depth of the troughs) as shown in Figure 6-33. This is because by increasing the amount of (Nb+Ti) content, the number of nucleation sites for  $\{111\}$  texture increases and, consequently, the  $\{100\}$  texture decreases.

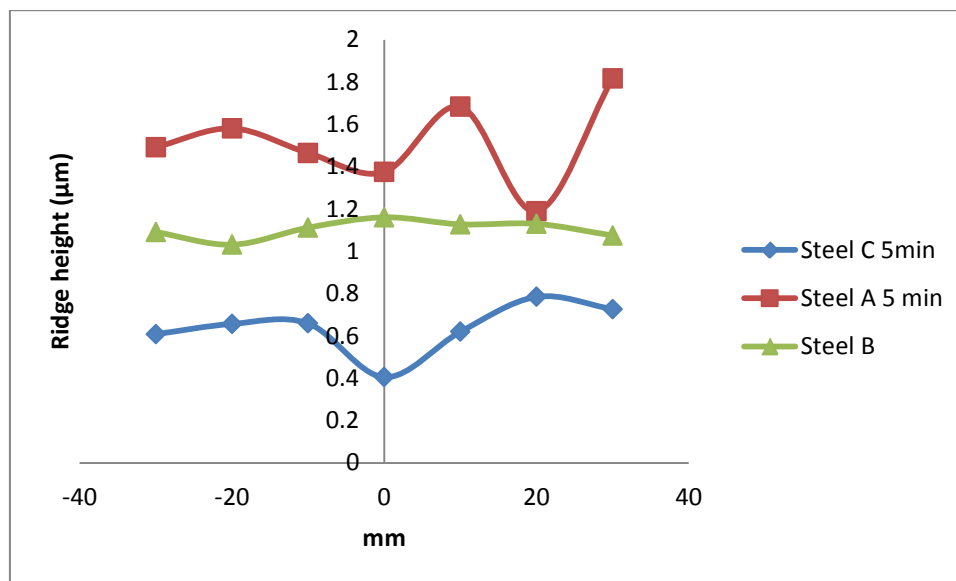


Figure 6-32: Effect of (Nb+Ti) content on ridging resistance of AISI 441 ferritic stainless steel after annealing at  $1025^\circ\text{C}$  for 300s.

It has been reported in literature that the main cause for ridging phenomenon in the Fe-17% Cr alloy is the  $\alpha$ -fibre in the centre layer of the hot rolled sheets which is inherited and stabilised by cold rolling [100, 101]. This is because the mechanism for ridging was found to be that of differential yielding under tension, which is brought by a variation in stored energy associated with different texture components in the sub-grains and grains i.e.  $\{100\}$  versus  $\{111\}$  texture components [10].

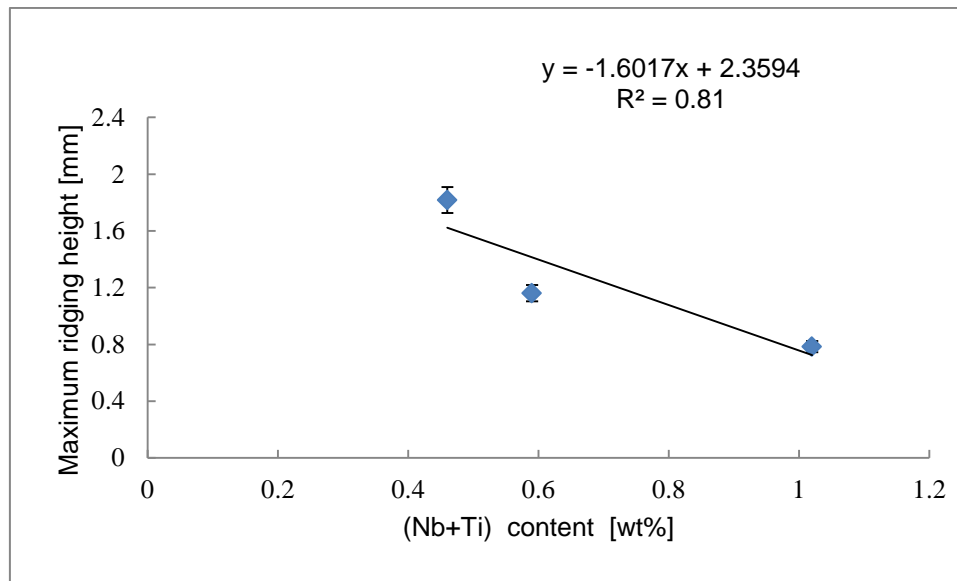


Figure 6-33: Effect of (Nb+Ti) content on the ridging resistance of AISI 441 ferritic stainless steel.

It was assumed in this context that the clustered lateral distribution of certain texture components such as the  $\alpha$ -fibre component  $\{001\}\langle 110\rangle$ ,  $\{112\}\langle 110\rangle$  and  $\{111\}\langle 110\rangle$  in case of ferritic steels can lead to unfavourable topological arrangement of the out of plane shears which is referred to as ridging. It has been found in literature that ridging phenomenon can be eliminated by reduction of these components and their topological clustering in the hot band texture, a change of the deformations mode or the randomisation of the texture by phase transformation [102-104].



## 7. CHAPTER 7: DISCUSSION

### 7.1. Introduction

The discussion of the results given in chapter 6 is divided into four parts:

- The first part which comprises section 7.2 deals with the effect of cold rolling and annealing process on microstructural and texture evolution in AISI 441 ferritic stainless steel;
- The second part which consists of section 7.3 presents the effect of cold rolling and annealing process on formability of AISI 441 ferritic stainless steel;
- The third section which consists of section 7.4 presents with the effect of (Nb+Ti) content on microstructural and texture evolution of AISI 441 ferritic stainless steels
- Lastly, section 7.5 deals with the effect of (Nb+Ti) content on ridging resistance of AISI 441 ferritic stainless steels

### 7.2. Effect of cold rolling and annealing process on microstructural and texture evolution in AISI 441 ferritic stainless steel

Hutchinson reported that during cold rolling, the texture of ferrite becomes progressive stronger and sharper with increasing deformation [71, 105]. It was further stated that the most important aim of sheet producers is to develop as strongly as possible the texture components in which  $\{111\}$  planes are parallel to the sheets i.e.  $\gamma$ -fibre. The cold rolled texture shows a strong RD// $\langle 110 \rangle$  fibre texture with a  $\{001\}\langle 110 \rangle$  having maximum intensity and ND// $\langle 111 \rangle$  fibre with a  $\{111\}\langle 110 \rangle$  having maximum intensity. During cold rolling, the grains with unstable orientations in the hot band rotate toward a more stable orientation. Inagaki [106] reported paths for crystal orientation as follows:

$$(A) \{100\}\langle 100 \rangle \rightarrow \{001\}\langle 110 \rangle \rightarrow \{112\}\langle 110 \rangle \rightarrow \{223\}\langle 110 \rangle$$

$$(B) \{110\}\langle 001 \rangle \rightarrow \{554\}\langle 225 \rangle \rightarrow \{111\}\langle 112 \rangle \rightarrow \{111\}\langle 110 \rangle \rightarrow \{223\}\langle 110 \rangle$$

From the above paths, it can be seen that path A goes through the  $\alpha$ -fibre orientation while path (B) goes through the  $\gamma$ -fibre orientation.

In Figure 6-18, the texture parameter  $\log_{10} \left( \frac{I_{\{111\}}}{I_{\{100\}}} \right)$  is plotted against the annealing temperature for 78 and 82% cold rolled materials respectively. In this study, the maximum orientation density of  $\phi = 55 \pm 10^\circ$  in the  $\varphi_2 = 45^\circ$  section of the ODF was taken as a representative of the  $\{111\}$  intensity [78]. From Figure 6-18, it can be seen that texture parameter increases with increase in annealing temperature. Annealing at 900 and 950°C, showed the presence of moderate  $\gamma$ -fibre texture with a maximum intensity  $f(g)$  of 10 and 11 respectively. Increasing the annealing temperature to 1025°C led to a very strong shifted  $\gamma$ -fibre namely  $\{554\}\langle 225 \rangle$  with  $f(g)$  of 18 and  $\{334\}\langle 483 \rangle$  with  $f(g)$  of 11.5 in 78% cold rolled steels as shown in Figure 6-16C. 82% cold rolled steels as shown in Figure 6-14C was characterised by strong  $\alpha$ -fibre  $\{111\}\langle 110 \rangle$  with intensity  $f(g)$  of 13 and the shifted  $\{111\}\langle 110 \rangle$  with intensity of 13. The cold rolled  $\alpha$ -fibre was completely disappeared after annealing at 1025°C as shown in Figure 6-17(a) to (c). Both the intensity of Cube-on-face and Goss textures were reduced after annealing at both 900 and 950°C and completely disappeared at 1025°C in both 78 and 82% cold reduction.

The intensity of  $\alpha$ -fibre decreased prominently after recrystallisation annealing at 1025°C. It has been reported in literature that intensity of  $\alpha$ -fibre completely disappear only during the late stages of recrystallisation when the volume of the recrystallised grains reaches 100% as shown in Figure 7-1below [107, 108]. This decrease in  $\alpha$ -fibre was associated with increase in intensity of the  $\{111\}\langle 112 \rangle$  or  $\{554\}\langle 225 \rangle$  component in the recrystallisation texture. This indicates that the  $\{111\}\langle 112 \rangle$  orientation grows more quickly into the remaining  $\alpha$ -fibre of the deformed matrix than the  $\{111\}\langle 110 \rangle$  [109]. It was further reported that this orientation change, which occurs during the final stages of recrystallisation, is unlikely to be controlled by nucleation mechanism because all the high stored energy sites of the deformed substructure have already being consumed by nucleation at earlier stages.

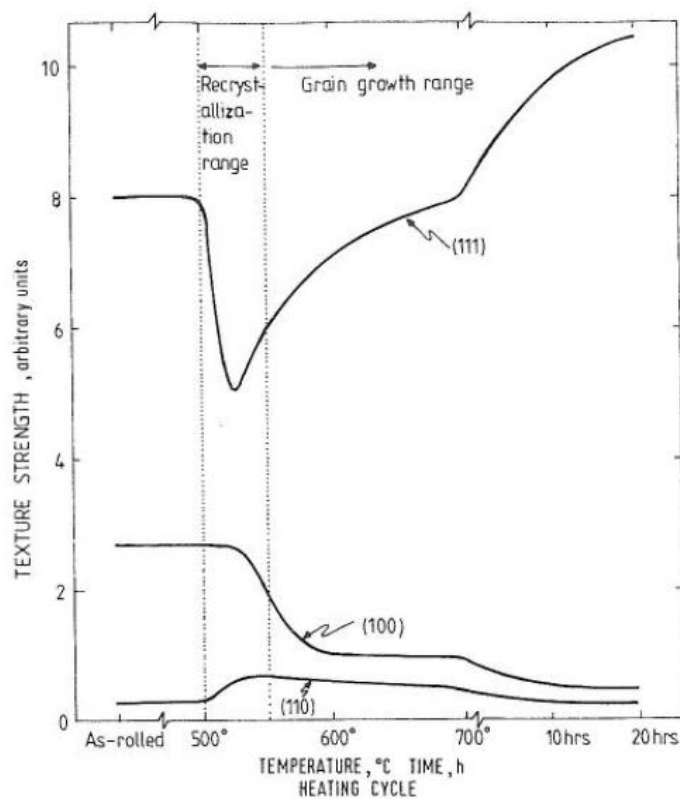


Figure 7-1: Effect of annealing time and temperature on texture variation of some important texture components in low carbon steel [107].

The reason for this was explained in terms of energy requirement. More energy is required to form  $\{111\}$  nucleation sites because the stored energy of a particular texture increases from  $\{100\} \langle 100 \rangle$  to  $\{111\} \langle uvw \rangle$  [71].

### 7.3. Effect of cold rolling and annealing process on formability of AISI 441 ferritic stainless steel

The relationship between the  $R_m$ -value and the amount of cold reduction is shown in Figure 6-19 in Chapter 6. Figure 6-19 clearly indicates that increasing the amount of cold reduction leads to increased  $R_m$ -value after annealing. It has been found in literature that the total amount of cold reduction is an important variable which controls the texture and formability of annealed sheets [35]. Final texture is weakly developed after small amount of cold reduction and the final texture normally contains  $\{110\} \langle 100 \rangle$ , the Goss component in addition to a  $\{111\}$  orientation [71]. The optimum cold reduction which corresponds to a maximum  $R_m$ -value was found

to be 78%. However the  $R_m$ -value was lowered significantly after 78% cold reduction, see Figure 6-14. This is in agreement with the results shown in the graph shown in Figure 4-22(a). Hutchinson [71, 105] reported that decreases in  $R_m$ -value after higher amount of cold reduction was accompanied by near  $\{100\}$  component, such as  $\{411\}\langle 148 \rangle$  and  $\{411\}\langle 011 \rangle$ . In this study, the materials annealed at 1025°C after 82% cold reduction showed no  $\{100\}$  texture components. However, the decline in  $R_m$ -value beyond 78% cold reduction can be attributed to the decrease in grain size after annealing i.e. the 82% cold rolled and annealed steel has finer grains, see Figure 6-5. Literature shows that increasing the grain size leads to increased  $I_{(111)}/I_{(100)}$  ratio and hence high  $R_m$ -value [42]. However, there must be the compromise between high  $R_m$ -value and mechanical properties of the steel.

It has been found in previous investigations [13, 14, 16] that the formability of ferritic stainless steel can be improved by increasing the average plastic strain ratio ( $R_m$ -value). This was found to be closely related to  $\{111\}$  recrystallisation texture. In Figure 6-20, the  $R_m$ -value is plotted against the logarithm of the texture parameter

$\log_{10} \left( \frac{I_{(111)}}{I_{(100)}} \right)$ . As may be seen from Figure 6-20, the  $R_m$ -value increases linearly with

an increase in  $\{111\}$  orientation. This is in agreement with previous observation that

increasing the  $\log_{10} \left( \frac{I_{(111)}}{I_{(100)}} \right)$  ratio leads to increased  $R_m$ -value [14, 42]. This is not

surprising because according to the calculated results using the relaxed constraints method of plasticity, Ray et al [43, 110] found that  $\{111\}$  orientation has a high  $R_m$ -value and smaller planar anisotropy compared to  $\{100\}$  orientation. Therefore, to achieve higher drawability, it is desirable to have higher proportion of grains orientated with their  $\{111\}$  planes parallel to the sheet planes i.e. materials possessing a strong  $\{111\}$  orientation and little  $\{100\}$  orientation. The equation from the regression analysis of the plot of the  $R_m$ -value versus the logarithm of the texture

parameter,  $\log_{10} \left( \frac{I_{(111)}}{I_{(100)}} \right)$  in Figure 6-20 as determined by XRD technique was found

to be:

$$R_m = 0.77 + 0.85 \log_{10} \frac{I_{(111)}}{I_{(100)}} \dots\dots\dots 7-2$$

Where  $R_m$  is the plastic anisotropy,  $I_{(111)}$  is the intensity of {111} orientation and  $I_{(100)}$  is the intensity of {100} orientation. Lewis and Pickering [16] studied the development of recrystallisation texture in ferritic stainless steels and their relationship on formability was found to be:

$$R_m = 0.77 + 0.36 \log_{10} \frac{I_{(111)}}{I_{(100)}} \dots\dots\dots 7-3$$

As may be seen from equations 7-2 and 7-3, the result from this study predicts slightly higher  $R_m$ -values. This could be due to a number of reasons arising from the different technique used, number of test (which were limited in this work) and chemical compositions of the steels. However, by and large, the results are comparable.

The planar anisotropy,  $\Delta R$ -values, of the 78% and 82% cold worked and annealed at 1025°C is higher than 62% cold worked. This is because texture in these materials is characterised mainly by shifted {111} orientation. i.e. {554}<225> and {334}<483>. Du Wei et al [63] said that shifted {111} orientation often lead to the increase in planar anisotropy. It was further observed that this shifted texture components results from the Zener drag and selective growth which gives rise to higher  $\Delta R$ -value.

#### **7.4. Effect of (Nb+Ti) content on microstructural and texture evolution of AISI 441 ferritic stainless steels**

##### **7.4.1. Effect of (Nb+Ti) content on the hot band and annealed hot band texture**

The evolution of the cold rolling texture is dependent on the hot rolling, hot band annealing and cold rolling processes [111]. 17% Cr ferritic stainless steels undergo rapid recovery before recrystallisation and there is no phase transformation during hot rolling due to their high Cr content and low carbon content [112]. In steel A, the maximum intensity was found at {223}<100> with some weak {001}<110> while in steel B, the maximum texture intensity was found to be {001}<110>, a typical orientation caused by plain strain deformation [45]. This strong {001}<110>



component in the hot band is generally inherited from  $\{001\}\langle uvw \rangle$  orientation from the as-cast material in ferritic stainless steels [14, 112, 113]. This is not surprising because the ferritic stainless steels are hard to recrystallise during hot rolling because of the fast dynamic recovery and the recrystallisation rate of the grain with  $\{hkl\}\langle 110 \rangle$  orientation is extremely low due to their low stored energy [112]. Therefore, this restricts texture randomisation through dynamic recrystallisation. Figure 6-26 shows the texture of the hot band materials. It can be seen that increasing the amount of (Nb+Ti) content lead to increased  $\gamma$ -fibre. This is not surprising because Nb and Ti tend to promote the formation of  $\gamma$ -fibre [106].

Figure 6-27 shows the texture of the hot rolled sheet after annealing at 1025°C for 5 minutes. The centre layer of steel B a consists of the  $\{hkl\}\langle 110 \rangle$  texture with a maximum  $f_{(g)}\max = 16$  at  $\{100\}\langle 110 \rangle$ , see Figure 6-27(a). This have has a negative effect on the formability and ridging resistance of ferritic stainless steels. The main aim of annealing hot band materials is to reduce the intensity of  $\{100\}\langle 110 \rangle$  orientation. However after annealing, the opposite of the expected results occurred. This may partially be due to either that the annealing temperature was too low or the time was short for full recrystallisation to take place. Therefore, full recrystallisation of the hot band can be achieved by annealing at higher temperature than 1025°C or longer annealing time at 1025°C. However the annealing temperature must be carefully chosen as this will have an effect on the annealed hot band grain size knowing that. The hot band grain sizes have effect of the final recrystallisation, with smaller grain size favouring nucleation of  $\gamma$ -fibre after recrystallisation [68, 120].

The same applies to steel C after similar annealing heat treatment, see Figure 6-27(b). As may be seen from Figure 6-26(c), steel C hot band initially consisted of entirely  $\gamma$ - fibre was only weakened by annealing heat treatment. This leads to an interesting debate as to whether the material should be annealed or cold worked without prior annealing treatment and could be a subject for further investigation.

#### **7.4.2. Effect of (Nb+Ti) content on the cold rolled texture**

Figure 6-28 to Figure 6-30 shows effect of (Nb+Ti) content on the cold worked texture of ferritic stainless steel. The texture of all three cold worked steels is characterised by  $RD//\langle 110 \rangle$  ( $\alpha$ -fibre) and  $ND//\langle 111 \rangle$  ( $\gamma$ -fibre). It can be seen from

Figure 6-28 to Figure 6-30 that increasing the (Nb+Ti) content lead to increased  $\{100\}\langle 110\rangle$  intensity. Otherwise the overall characteristic of the texture in steel A to C remains the same. This is not surprising because deformation texture depend solely on the amount of deformation applied to the steel [71].

#### 7.4.3. Effect of (Nb+Ti) content on the recrystallisation texture

Figure 6-31 shows the effect of (Nb+Ti) content on the recrystallisation texture of AISI 441 ferritic stainless steel. The texture of all three steels i.e. steel A, B and C is approximated by  $RD//\langle 110\rangle$  and  $ND//\langle 111\rangle$ . From Figure 6-31, it can be seen that increasing the (Nb+Ti) content enhanced the formation of  $ND//\langle 111\rangle$  i.e.  $\gamma$ -fibre, notably the  $\{111\}\langle 112\rangle$ ,  $\{554\}\langle 225\rangle$  and  $\{111\}\langle 110\rangle$ . The formation of  $\{554\}\langle 225\rangle$  texture component in these steels is due to the (Nb,Ti)(C,N). This is in agreement with the Sawatani et al [114] that the favourable fine Ti(C,N) precipitate suppresses recrystallisation of  $\{110\}\langle 001\rangle$  during annealing heat treatment and high intense  $\{554\}\langle 225\rangle$  i.e. shifted  $\{111\}\langle 112\rangle$  recrystallisation texture is preferentially formed. It has been indicated in literature that addition of Nb and Ti to ferritic stainless steel forms carbonitrides precipitate and this precipitates have been found to have significant effects on final recrystallisation texture [115]. These carbonitrides supply more sites for nucleation. Liu and Yang on their study found that addition Nb and Ti increases the equiaxed grain ratio, the microstructure refinement and enhance  $\gamma$ -fibre in the recrystallisation texture [116, 117].

The formation of the  $\gamma$ -fibre can also be explained in terms of the particle stimulated nucleation. Particle stimulated nucleation (PSN) by undissolved (Nb,Ti)(C,N) produces highly favourable  $\{111\}\langle 112\rangle$  texture. Areas surrounding large (Nb,Ti)(C,N) satisfies energy requirement for nucleation of  $\{111\}\langle uvw\rangle$  due to strain energy induced in the surrounding matrix [16, 107]. More energy is required to form  $\{111\}$  nucleation sites. The reason for this being that the stored energy of a particular texture increases from  $\{100\}\langle 011\rangle$  through  $\{110\}\langle 011\rangle$  to  $\{111\}\langle uvw\rangle$ . The  $\{111\}\langle uvw\rangle$  texture has the greatest misorientation and thus for nucleation sites of the  $\{111\}\langle uvw\rangle$  texture to form, large misorientation energy must be present at the nucleation site [18,87]. It was further observed that the energy requirement is

satisfied in the region surrounding the Nb or Ti precipitates due to inhomogeneous deformation.

However these precipitates must form inside the matrix because of their negative effect on  $\gamma$ -fibre enhancement when they precipitate on grain boundaries. In a study on the recrystallisation behaviour of Ti stabilised ferritic stainless steel sheet, Sinclair et al [118, 119] found that the precipitation of fine Ti(C,N) on grain boundaries retard the grain boundary motion restricting the growth of  $\gamma$ -fibre recrystallisation texture weakening it.

### **7.5. Effect of (Nb+Ti) content on ridging resistance of AISI 441 ferritic stainless steels**

Effect of (Nb+Ti) content on the ridging severity is indicated in Figure 6-32. As may be seen, an increase in (Nb+Ti) content leads to an increases ridging resistance. It has been found in literature that addition of Nb and Ti promotes the development of {111} type texture and reduces {100} type texture [85] . Figure 6-33 shows the maximum ridging height as a function of (Nb+Ti) content and it is evident from this figure that an increase in (Nb+Ti) content results in an increase in ridging resistance.

Applying the three ridging models in section 4.6, it can be concluded that by minimising cube on face texture {100} orientation and maximising the {111} texture, the ridging phenomenon problem can be minimised if not eradicated completely. As mentioned earlier, increasing the (Nb+Ti) content increases the amount of {111} texture component at the expense of {100} texture and that leads to improved ridging resistance as observed in Figures 6-27 and 6-28 above.

## 8. CHAPTER 8: CONCLUSIONS

The primary objective of this study was to enhance the understanding of the effects of thermomechanical processing and chemical composition on the texture evolution of AISI 441 ferritic stainless steel and relate that to its ridging severity and formability. The following conclusions can be made from this study:

1. Optimising the amount of cold reduction and annealing temperature are crucial to ensure that desirable  $\gamma$ -fibre is obtained and  $\alpha$ -fibre is minimised. The steel that received 78% cold reduction and annealed at 1025°C exhibited the highest intensity of shifted  $\gamma$ -fibre notably  $\{554\}\langle 225 \rangle$  and  $\{334\}\langle 483 \rangle$ . This is favourable for deep drawing.
2. The 78% and 82% cold rolled steels after being annealed at 1025°C, showed no texture component in the (100) plane, therefore it is concluded that this steels will experience minimal ridging compared to 62% cold rolled steels annealed at 1025°C.
3. Increasing the (Nb+Ti) content did not have effect on the overall texture intensity. However, increasing (Nb+Ti) content enhanced the formation of  $\gamma$ -fibre and reduced  $\alpha$ -fibre and this resulted in improved ridging resistance i.e. the steel with the highest (Nb+Ti) content experienced the least ridging.

## 9. CHAPTER 9: RECOMMENDATION

Annealing the hot band samples lead to weakening of  $\gamma$ -fibre and favouring the formation of  $\alpha$ -fibre, it is therefore, recommended that effect of the annealing process on texture evolution of the hot band be investigated. It is also recommended that the effect of composition on the recrystallisation kinetics be investigated.



## 10. REFERENCES

1. Charles et al. *The Ferritic Stainless Steel Family: The appropriate Answer to Nickel Volatility*. [cited 2011 03 March ]; Available from: <http://arcelormittal.com/stainlesseurope/sites/default/files/fckfiles/uploadfile/Documentation/Technic>.
2. Venter, I. *Catalytic Converter Industry and DTI at Incentive Impasse*. 2010 [cited 2012 10 May ]; Available from: <http://www.engineeringnews.co.za/article/catalytic-converter-industry-and-dti-at-incentives-impasse-2010-08-05>.
3. [cited 2012 10 May ]; Available from: [http://www.sassda.co.za/sectors/tubes\\_pipes.htm](http://www.sassda.co.za/sectors/tubes_pipes.htm).
4. Venter, I. *MIDP Uncertainty Blamed for 6.2% Fall in SA Catalytic Converter Exports*. 2008; Available from: <http://www.engineeringnews.co.za/article/midp-uncertainty-blamed-for-62-fall-in-sa-catalyticconverter-exports-2008-05-02>.
5. Fujita et al. *Changes of microstructures and High Temperature Properties during High Temperature Service of Niobium Added Ferritic Stainless Steels*. *Materials Science and Engineering A*, 2003. Vol. 351: pp. 272-281.
6. Sato, E. and Tanoue, T. *Present and Future Trends of Materials for Automotive Exhaust Systems*, in *Nippon Steel Technical Report No.641995*. p. 13-17.
7. Atsushi et al. *Ferritic Stainless Steel for Automotive Exhaust Systems-High Heat Resistant Ferritic Stainless Steel with High Formability for Automotive Exhaust Manifolds: "JFE-MH1"*. JFE Technical Report No.4, 2004: pp. 61-66.
8. Hiramatsu, S. *The Stainless*, 1994. Vol. 38: pp. 10.
9. Fujita et al. *Scripta Materialia*, 1996. Vol. 35: No.6, pp. 705-710.
10. Sheppard, T. and Richards, P. *Materials Science and Technology*, 1986. Vol. 2: pp. 693-699.
11. Chao, H. *Metallurgical Transactions*, 1973. Vol. 4: pp. 1183-1186.
12. Takechi, et al. *Trans. JIM*, 1967. Vol. 8: pp. 233-239.
13. Muller et al, *Journal of the South African Institute of Mining and Metallurgy*, 1990. Vol: 90, No.1, p. 17-26.
14. Huh, M.-Y. and Engler, O. *Materials Science and Engineering A*, 2001. Vol. 308: pp. 74-87.
15. de Abreu et al. *Materials Characterization*, 2006. Vol. 57: pp. 342-347.
16. Lewis, D.B and Pickering, F.B. *Metals Technology*, 1983. Vol. 10: pp. 264-273.
17. Davison, R.M. *Metallurgical Transactions*, 1974. Vol. 5: pp. 2287-2294.
18. Kiaei et al. *Journal de Physique IV, Colloque C3, Supplement au Journal de Physique III*, 1995. Vol. 5: pp. C3-67-C3-75.





19. Lula, R.A. *Stainless steel*. Revised Edition, 1986: American Society for Metals, Metals Park, Ohio.
20. Simmons, J.W. *Materials Science and Engineering A*, 1996. Vol. 207: pp. 159-169.
21. Stumpf, W.E. *Chapter 4: Precipitation of Intermetallic Compounds in Higher Alloyed Steels, NFM 700 Course Notes, University of Pretoria*. 2009.
22. Sourmail, T. *Materials Science and Technology*, 2001. Vol.17: No.1, pp.-14.
23. Llewellyn, D.T. *Steels: Metallurgy and Applications*: 1994: Butterworth-Heinemann Ltd, pp. 14-22.
24. Sedriks, A.J. *Corrosion of Stainless Steels*. 2nd Edition,1996: Wiley-Interscience Publication.
25. *Columbus Stainless Technical Data Sheets*. [cited 2011 01 February]; Available from: [www.columbusstainless.co.za](http://www.columbusstainless.co.za).
26. van Zwieten, A.C.T.M. and Bulloch, J.H. *International Journal of Pressure Vessels and Piping*, 1993. Vol. 56: pp. 1-31.
27. Yamagishia, et al. *Procedia Engineering*, 2010. Vol. 2: pp. 275-281.
28. Zucatoa et al. *Materials Research*, 2002. Vol. 5: No.3, pp. 385-389.
29. Coreno-Alonso et al. *Materials Chemistry and Physics*, , 2004. Vol. 84: pp. 20-28.
30. Leslie, W.C. *The Physical Metallurgy of Steels*. Materials Science and Engineering Series1981, London: Hemisphere Publishing Corporation.
31. Inoue, Y. and Kikuchi, H. *Present and Future Trends of Stainless Steels for Automotive Exhaust System*. Nippon Steel Technical Report No.88, 2003: pp. 62-68.
32. Amuda, M.O.H. and Mridha, S. *International Journal of Corrosion*, 2011. 2011.
33. Grubb, J.F. *Stabilization of High Chromium Ferritic Stainless Steels*. in *Proceedings of International Conference on Stainless Steels*. 1991. Chiba: ISIJ.
34. *European Standard Ref. No EN 10088-2:2005*, June 2005, European Committee for Standardisation: Brussels.
35. Lewis, D.B. and Pickering, F.B. *Development of Recrystallisation Textures in Ferritic Stainless Steels and their Relationship to Formability*, in "*Advances in the Physical Metallurgy and Applications of Steels*" *Proc. Int. Conf. Metals Soc*1982, The Metals Society, London: University of Liverpool, .
36. Gordon, W. and van Bennekom, A. *Materials Science and Technology*, 1996. Vol. 12: pp. 126-131.
37. Yan et al. *Materials Characterization*, 2009. Vol. 60: pp. 65-68.
38. Shua et al. *Journal of Materials Processing Technology*, 2012. Vol. 212: pp. 59-65.



39. Barrett, C. and Massalski, T.B. *Structure of Metals*. International Series on Materials Science and Technology. Vol. 3rd revised Edition. 1980: Pergamon Press Inc.
40. Suwas, S. and Gurao, N.P. *Journal of Indian Institute of Science*, 2008. Vol. 88: No.2, pp. 151-176.
41. Stumpf, W.E. *Chapter 6: The Hot and Cold Rolling of Metals: NMM 320 Course Notes: University of Pretoria*. 2007.
42. Hatherley, M. and Hutchinson, W.B. *An Introduction to Textures In Metals*. The Institution of Metallurgist, 1979. Monograph No.5: pp. 1-74.
43. Ray, et al. *ISIJ International*, 1994. Vol. 34: No.12, pp. 927-942.
44. Bunge, H.J. *Texture Analysis in Materials Science: Mathematical Methods* 1982: Butterworths & Co.
45. Zhang et al. *Journal of Materials Processing Technology*, 2011. Vol. 211: pp. 1051-1059.
46. Raabe, D. and Lucke, K. *Materials Science and Technology*, 1993. Vol. 9: pp. 302-311.
47. Engler, O. and Randle, V. *Introduction to Texture Analysis: Macrotecture, Microtexture and Orientation Mapping*. 2nd Edition ed2010: CRC Press.
48. Xie, C.L. and Nakamachi, E. *Materials Science and Engineering A*, 2003. Vol. 340: pp. 130-138.
49. Roe, Ryong-Joon. *Journal of Applied Physics*, 1965. Vol. 36: No.6, p. 2024-2031.
50. Verlinden et al. *Thermomechanical Processing of Metallic Materials*. Pergamon Materials Series, ed. R.W. Cahn, 2007. Chapter 8.
51. Wenk, H-R. and van Houtte, P. *Texture and Anisotropy*. Reports on Progress in Physics, 2004. Vol. 67: pp. 1367-1428.
52. Stumpf, W.E. *Chapter 5: Static and Dynamic Recrystallisation , NFM 700 Course notes. University of Pretoria*. 2009.
53. Leslie, W. *Trans AIME*, 1961. Vol. 221: pp. 752.
54. Hosford, W. *Trans AIME*, 1964. Vol. 230: pp. 12.
55. George E. Dieter, *Mechanical Metallurgy*. Metallurgy and Metallurgical Engineering, 1961, USA: McGraw-Hill
56. Hu, H. *Texture*, 1974. Vol. 1: pp. 233-258.
57. Honeycombe, R.W.K., *The Plastic Deformation of Metals* 1968: Edward Arnold Ltd.
58. Doherty, R.D. *Scripta Metallurgica*, 1985. Vol. 19: pp. 927.
59. Hölscher, M. and Staubwasser, L. in *Proc Int Conf "Processes and Materials Innovation in Stainless Steel Products"*, 1993: Florence, Italy.
60. Shin et al. *Acta Materialia*, 2003. Vol. 51: pp. 4693-4706.



61. Brochu et al. . ISIJ International, 1997. Vol. 37, No.9: pp. 872-877.
62. Suzuki et al. Transactions ISIJ, 1983. Vol. 23: pp. 731-737.
63. du Wei et al. Journal of Iron and Steel Research, International, 2010. Vol. 17: No.6, pp. 47-52.
64. Wu et al. Materials Science and Engineering A, 2006. Vol. 423: pp. 300-305.
65. Chao, H. Trans ASM, 1967. Vol. 60: pp. 37.
66. Takechi et al. Trans. Japan Institute of Metal, 1967. Vol. 8: pp. 223.
67. Wright, R.N. Metallurgical Transactions, 1972. Vol. 3: pp. 83-91.
68. Ray, R.K. and Jonas, J.J. International Materials Reviews, 1990. Vol. 35, No.1: pp. 1-36.
69. Yazawa et al. ISIJ International, 2003. Vol. 43: No.10, pp. 1647-1651.
70. HU, H. and Goodman, S.R. Metallurgical Transactions, 1970. Vol. 1: pp. 3057-3060.
71. Hutchinson, W.B. International Metals Reviews, 1984. Vol. 29: No.1, pp. 25-41.
72. Fukuda, M., Journal of Iron and Steel Institute, Japan, 1967. Vol. 53: pp. 559-561.
73. Takahashi, M. and Okamoto, A. Transactions of Iron and Steel Institute, Japan, 1979. Vol. 19: pp. 391-400.
74. Wallen, B. and Olssen, J. *Handbook of Stainless Steels*, D. Peckner and I.M. Bernstein, Editors. 1977, McGraw-Hill: New York. pp. 16-77.
75. Field, D.P., Ultramicroscopy, 1997. Vol. 1-9: pp. 67.
76. Humphreys, F.J., Scripta Materialia, 2004. Vol. 51: pp. 771.
77. Beddoes, J. and Bibby, M.J. in *Principles of metal manufacturing processes* 1999, Arnold: London. pp. 142-161.
78. Hamada et al. ISIJ International, 2011. Vol. 51: No.10, pp. 1740-1748.
79. Hughes, D.A. and Hansen, N., Scripta Metallurgica and materilia, 1995. Vol. 33: No.2, pp. 315.
80. Hughes, D.A. and Hansen, N., Acta Materialia, 1997. Vol. 45: No.9, pp. 3871.
81. Humphrey et al., Philosophical Transactions of the Royal Society, 1999. B57: pp. 1663.
82. Humphreys, F.J. and M. Hatherly, *Recrystallisation and Related Annealing Phenomena* 1995, Oxford: Pergamon Press.
83. Watanabe, T., Scripta Metallurgica, 1992. Vol. 27: pp. 1497.
84. Fu-ren et al. Journal of Iron and Steel Research, International, 2012. Vol. 19: No.11 pp. 52-56.
85. Yan et al. Materials Characterisation, 2008 Vol. 59: pp. 1741-1746.



86. Sello, M.P. and Stumpf, W.E. *Materials Science and Engineering A*, 2010. Vol. 527: pp. 5194-5202.
87. Park et al. *Acta Materialia*, 1998. Vol. 46:No.10, pp.3371-3379.
88. Samajdar et al. *Acta Materialia*, 1998. Vol. 46, No.8,pp.2751-2763.
89. Khatirkar et al. *Trans IIM*, 2010. Vol. 63: No.1, p. pp.55-62.
90. Ushioda et al. *Materials Science and Technology*, 1986. Vol. 2: pp. 807-815.
91. Humane et al. *Trans IIM*, 2010. Vol. 63: No.6, pp.867-880.
92. He et al. *Materials Science and Technology*, 2005. Vol. 21: No.12, pp. 1436-1439.
93. Uematsu, Y. and Yamazaki, Y. *Tetsu-to-Hangane*, 1992. Vol. 78: pp. 632.
94. Park et al. *ISIJ International*, 2002. Vol. 42: pp. 100.
95. D.Raabe and Lucke, K. *Scripta Metallurgica*, 1992. Vol. 27: pp. 1533.
96. Raabe et al. *Steel Research*, 1993. Vol. 64: pp. 359.
97. D.Raabe and K. Lucke, *Scripta Metallurgica and materialia*, 1992. Vol. 26: pp. 29.
98. du Wei et al. *Journal of Iron and Steel Research, International*, 2010. Vol. 17: No.7: pp. 58-62.
99. Tsuji et al. *ISIJ International*, 1993. Vol. 33: No.7, pp. 783-792.
100. Engler et al. *Tome, Metallurgical and Materials Transactions A*, 2005. Vol. 36: pp. 3127-3139.
101. Knutsen, R.D. and Wittridge, N.J. *Materials Science and Technology*, 2002. Vol.18: pp. 1279-1285.
102. Wittridge, N.J. and Knutsen, R.D. *Materials Science and Engineering A*, 1999. Vol. 269: pp. 2005.
103. Knutsen, R.D. and Wittridge, N.J. in *Processing of International Conference Minerals and Materials*. 1996, SAIMM: Somerset West, South Africa. pp. 632-640.
104. Wittridge, N.J. and Knutsen, R.D. *Materials Characterisation*, 1996. Vol. 31.
105. Hutchinson, W.B. *Metal Science*, 1974. Vol. 8: pp.185-196.
106. Inagaki, H. *ISIJ International*, 1994. Vol. 34: pp. 313.
107. Haessner, F. *Recrystallisation of Metallic Materials*. 2nd Edition ed1978, Germany: Dr. Reiderer Verlag.
108. R.Saha and Ray, R.K. *Journal of Material Science*, 2008. Vol. 43: pp. 207-211.
109. Kestens, L. and Jonas, J.J. *Metals and Materials*, 1999. Vol. 5: No. 5, pp. 419-427.
110. Ray et al. *ISIJ International*, 1992. Vol. 32: No.2: pp. 203-212.

111. Gao et al. Journal of Materials Science, 2012. DOI 10.1007/s10853-012-7027-5.
112. Liu et al. ISIJ International, 2009. Vol. 49: pp. 890.
113. Miyamoto et al. ISIJ International, 2010. Vol. 50: pp. 1653.
114. Sawatani et al. Tetsu-to-Hangane, 1977. Vol.63(No.5): pp.843-854.
115. Du et al. Journal of Iron and Steel Research International, 2010. Vol.17: pp. 159.
116. Liu, Y.D. and Yang Y. Applied Mechanics and Materials, 2011. Vols. 55-57: pp.1926-1931.
117. Liu, Y.D. and Yang Y. Advanced Materials Research, 2011. Vols. 181-182: pp.1054-1058.
118. Sinclair et al. Advances of Engineering Materials, 2003. Vol. 5: pp. 570.
119. Sinclair et al. Metallurgical and Materials Transactions A, 2005. Vol. 36: pp. 3205.
120. Ray et al. International Materials Review, 1994. Vol. 39: No.4, pp.129.